学位申請論文

村上哲也

論 文 内 容 の 要 旨

報告番号	甲第　　号	氏名	村上哲也
論文調査担当者	主査　小林晨作 三宅弘三　　玉垣良三		

（論文題目）

Detailed Study of the $^{12}C(^{16}O,\alpha)$ Reaction Mechanism

（$^{12}C(^{16}O,\alpha)$反応機構の詳細研究）

（論文内容の要旨）

$^{12}C+^{12}C$系の高スピン分子的共鳴状態が重クラスターの直接移行反応によって励起出来る可能性が示唆されて以来，これに関係する研究が精力的に行われて来た。入射エネルギー145MeVでの$^{12}C(^{16}O,\alpha)$反応よりのαスペクトルは複合核過程から来ると思われる大きな連続的バックグラウンドの上に，いくつかの顕著な構造を示した。これらの構造の位置が$^{12}C(^{12}C,X)$反応の励起関数に見られる構造のものと相関があること，角分布は，反応機構が^{12}C移行過程であることを示唆する強い前方ピークをもつこと，同じような構造が$^{12}C(^{16}O,\alpha)$反応では見られないこと等，分子的共鳴状態が$^{12}C(^{16}O,\alpha)$反応の終状態として作られている可能性が強いと考えられた。もしそうなら，分子的共鳴状態のうち特定スピンのものを，重イオン核反応の一つの特徴である運動学的整合条件を積極的に利用して，選択的に励起出来，分子的共鳴状態の研究を大いに発展させることが出来よう。そこ

で申請者はこの現象をさらに追求するために，三種類の実験を行った。まず第一に$^{13}C(^{16}O,\alpha,^{12}C)^{13}C$の粒子相関を入射エネルギー145 MeVで測定した。これにより$^{12}C(^{16}O,\alpha)$反応のαスペクトルにみられる構造が分子的共鳴状態であるならば，この構造のかなりの部分が$^{12}C+^{12}C$に分裂していることがわかるはずである。結果は，(1)同時計測α－^{12}Cの持つ断面積が非常に小さいこと，(2)同時計測α粒子のスペクトルには同時計測をしないときに見られたような構造がみられないことを示した。これから得られる結論はシングルαスペクトルに見られた構造は分子的共鳴状態に起因しないか，或いは$^{12}C+^{12}C$に分裂する分岐比が予想されている値に比して著しく小さいということである。しかし収量の少ない粒子相関の実験だけでは，統計的精度をあげて明確な結論を得ることはむつかしいので，入射エネルギーを系統的に変えることによりシングルαスペクトルの構造を調べた。その結果入射粒子のエネルギーをかえるに従って，構造の位置が，終状態の^{24}Mgの励起エネルギーで考えた場合，連続的に動くことがわかった。簡単な運動学的考察から，構造が^{24}Mgの励起状態或いはより特殊的に分子的共鳴状態ではなくむしろ放出粒子^{16}O，および^{16}Oが標的核からαをピック　アップして出来る^{20}Neのα崩壊によって生ずることがわかった。同じような構造が$^{13}C(^{16}O,\alpha)$反応では殆んどみられないという事実と考え合わせて放出粒子^{20}Neの崩壊過程がより大きな役目を果していると推測される。この推論は申請者等の第3の実験，$^{16}O(^{12}C,^{8}Be)^{20}Ne$反応の測定結果と他グループの$^{16}O(^{13}C,^{9}Be)^{20}Ne$反応のデータとを比較することによって支持された。このように3つの実験を行うことによって従来分子的共鳴状態と関係すると思われていたαスペクトルの構造が実は入射粒子が標的核からαをピック・アップしてその後α崩壊する過程に由来することが明らかになった。

「論文」

DETAILED STUDY OF THE $^{12}C(^{16}O,\alpha)$ REACTION MECHANISM

Tetsuya Murakami

This work was carried out at the Cyclotron Institute, Texas A&M University, College Station, Texas and submitted to the Department of Physics, Kyoto University, Japan for partial fulfillment of a doctral degree.

ABSTRACT

A series of experiments concerning the $^{12}C(^{16}O,\alpha)$ reaction was performed to find out an evidence of the existence of the molecular resonances as a final state interaction of the $^{12}C(^{16}O,\alpha)$ reaction. Contrary to our expectation, no evidence was found. The experimental results clearly indicate the importance of the sequential ejectile α-decay processes in the $^{12}C(^{16}O,\alpha)$ reaction. In fact the $^{20}Ne^*$ sequential decay process can explain most of the experimental facts qualitatively, although we cannot neglect the contribution of the $^{16}O^*$ sequential decay process.

TABLE OF CONTENTS

I. INTRODUCTION

A. General Remarks of Heavy-Ion Reactions

The heavy-ion nuclear physics has been one of the most actively studied areas in the nuclear physics in these two decades. This is mainly owing to development of heavy-ion accelerators and particle detecting systems, which lead us to investigate various combinations of projectiles and targets. It is well known, in heavy-ion induced reactions, the wave length of a projectile is much shorter than the typical dimension of system. Therefore an application of semiclassical theory for their motions is allowed. Moreover, heavy-ion can carry quite large angular momentum and energy so that they might make more complicated but exotic states. In fact accumlated data of heavy-ion induced reactions have revealed many characteristic features. Some of them can be summarized as follows:

(i) In relatively light nuclei systems, such as a $^{12}C+^{12}C$ system, so-called nuclear molecular resonances have been found [1]. The widths of them are surprisingly narrower than those of potential shape resonances and wider than those of compound resonances. This fact indicates the existence of intermediate structures in those systems. For example, in the $^{12}C+^{12}C$ system distinct structures have been observed in excitation functions of various exit channels such as elastic, inelastic, fusion, and so on.

(ii) Like light-ion induced reactions, direct reaction processes have been observed in relatively light "heavy-ion" induced reactions such as inelastic and few-nucleon transfer reactions leading to

discrete states [2]. Traditional direct reaction treatments, such as the distorted-wave Born approximation (DWBA) including the finite range and recoil effects, generally work well to explain those phenomena. As expected, it has been proved that such reactions provide uniqe approaches to high-spin cluster states which cannot be populated by light-ion induced reactions.

(iii) It was found that new reaction processes showing large mass, charge, energy, and angular momentum transfers have unexpectedly large cross section, when incident projectile energies are well above Coulomb barriers of systems [3]. Concerning those phenomena, many new terminologies, such as quasi-elastic scattering, deep-inelastic scattering, quasi-fission, pre-compound etc., were developed. To explain them, usually rather macroscopic pictures, like friction model etc. are used.

(iv) Compound nuclear reactions, such as (HI,xnγ) reactions, have opened up new area of high-spin states nuclear physics, because they favorably populate very high-spin residual states [4].

(v) Though not observed yet, many people expect that we can create high density, condensed states of nuclear matter by using heavy projectiles with relativistic energy ~GeV/AMU. Next generation accelerators now under constructions might give us answers.

Recently new methods to investigate the nuclear molecular resonances are proposed mainly by the Texas A&M University group [5]. As mentioned in (ii), direct few-nucleon transfer reactions are promising way to study high-spin cluster states. Therefore, it is natural to extend such an approch to much exotic states like nuclear

molecular resonances. In the next section, we will review such attempts.

B. Review of the $^{12}C(^{16}O,\alpha)$ Reaction

During the past two decades, enormous experimental and theoretical efforts have been devoted to study the $^{12}C+^{12}C$ system, in which the so-called nuclear molecular resonances were found in excitation functions of several reaction channels (see refs. [6] for recent reviews). According to those accumulated data, the resonances with the same J^{π} values are clustered in the several exit channels, such as ^{16}O, ^{8}Be and α channels, and they seem to make gross structures with a unique J^{π} value. The relation between the spin value and the centroid energy of the same spin group was well predicted by the Yale potential, which was determined by fitting the elastic scattering angular distribution. This relation is easily extended to the much higher energy region where Cormier et al. [7] found the presence of strong structures supposed to have spin 14^{+}, 16^{+} and 18^{+}.

Though well-investigated, the $^{12}C+^{12}C$ nuclear molecular states have been still not well-understood especially for its high-spin members. For example, even an existence of the molecular states is uncertain in highly-excited energy region of ^{24}Mg. Recently the gamma/particle decay branching ratios of possible 14^{+} members of the molecular band at $E_x(^{24}Mg)$=39.1, 39.7 MeV has been measured [8,9]. The small observed branching ratios support that these particular resonances have structures as shape resonances rather than as molecular states.

Till quite recently, the $^{12}C+^{12}C$ system has been studied only by taking the excitation function of the $^{12}C(^{12}C,X)$ reaction, but this

procedure is quite tedious to determine the resonance energies and J^{π} values. However, after Lazzarini et al. [10] showed the possibility to make such resonances as final states in a multiparticle transfer reaction using the $^{12}C(^{16}O,\alpha)^{24}Mg$ reaction at ^{16}O incident energies of 62 to 100 MeV, the investigation using multiparticle transfer reaction has attracted much attentions. According to their results, though there is large competition from the compound process, the $^{12}C(^{16}O,\alpha)^{24}Mg$ reaction can selectively populate the states in ^{24}Mg which correlate to those found in $^{12}C(^{12}C,X)$ excitation functions.

Using multiparticle transfer reaction, several resonances can be seen in one energy measurement and measuring the decay yields from the resonances allow us to determine the branching ratio of them. The spins of the final states could be determined by an angular correlation measurement of subsequent particle decay from those states. Moreover, considering that the ground state of ^{16}O has a strong α-$^{12}C(2^+)$ clustering strength, the $^{12}C(^{16}O,\alpha)^{24}Mg$ reaction could also make odd natural parity states which have $^{12}C+^{12}C(2^+)$ configuration.

To populate much higher-spin states in ^{24}Mg nucleus, the $^{12}C(^{16}O,\alpha)$ reaction at an ^{16}O incident energy of 145 MeV was performed by Nagatani et al. [5]. Their results obtained at θ_{lab}=7, 15, and 40° are shown in Fig. I-1. As seen in this figure, a series of broad peaks exists on an underlying continuum background, they are seen more clearly after background subtraction. The energies of these structures seemed to correlate with those of high-spin nuclear molecular states (12^+), (14^+), (16^+) and (18^+) and they were strongly enhanced at forward angles. In contrast, similar structures were not observed in the inclusive α-spectra obtained by bombarding ^{13}C with 145 MeV ^{16}O. Since molecular resonance structures were not observed in $^{12}C+^{13}C$

system, Nagatani et al. suggested that the obtained structures were caused by a direct ^{12}C transfer to the molecular resonances [5].

The high-spin molecular resonances observed in the $^{12}C+^{12}C$ system are reported to have large partial widths for the decay into $^{12}C(g.s.)+^{12}C(g.s.)$ and $^{12}C(g.s.)+^{12}C(2^+)$ channels [7], and so resonant $^{12}C+^{12}C$ final states made by the $^{12}C(^{16}O,\alpha)^{24}Mg^*$ reaction should decay mainly into those channels. Therefore coincidence measurement would reduce the background from other processes and allow the molecular states to be observed more clearly. To find out those processes, Rae et al. carried out coincidence measurements of $^{12}C(^{16}O,\alpha^{12}C)^{12}C$ and $^{13}C(^{16}O,\alpha^{12}C)^{13}C$ reactions at an ^{16}O incident energy of 140 MeV [11]. Those data were taken at 22 angle pairs covering 7.5° to 30° in the laboratory for the ^{12}C particle and -4° to -18° for the α particle, and their result was negative, no evidence for a $^{12}C+^{12}C$ final state interaction was found. Instead of $^{12}C+^{12}C$ final state interaction, $\alpha+^{12}C$ one was clearly observed. Considering this fact, Rae et al. offered the sequential decay process of $^{16}O^*$ as an one possible origin of the structures.

Branford et al. also suggested the same interpretation [12]. They measured the total widths and α decay branching ratios of the peaks in the inclusive α spectrum of $^{12}C(^{16}O,\alpha)^{24}Mg$ reaction with very high resolution in the bombarding energy region of 60 to 100 MeV. It turned out that the observed states in the ^{24}Mg excitation energy E_x=20-30 MeV have narrower total widths (~50 keV) than those of the known ^{24}Mg molecular states. Moreover the decay branching ratios of those states to the ground state of ^{20}Ne were very small. Based on these results, they concluded that at least in Lazzarini's experiment [10], direct excitation of molecular states seems unlikely.

Fig. I-1. α-spectra from the $^{12}C(^{16}O,\alpha)^{24}Mg$ reaction at $E(^{16}O)=145$ MeV. (From ref. [5].)

RELATIVE YIELDS
E_α (MeV)
7°
15°
40°
COUNTS
4000
3000
2000
1000
-4.1
-1.4
0.0
-8.1
-9.5
-13.1
-16.5
-16.8
-20.0
-21.2
-23.8
-20.0
21.2
26
29
27
(10+)
31
35
(12+)
38
42
(14+)
43
48
(16+)
51
56
(18+)
-8.1
-9.5
-13.1
-16.8
-20.0
-21.2
20.0
29
27
(10+)
31
35
(12+)
38
42
(14+)
-13.1
-16.5
-20
-28
-33
-40

On the other hand, Ichimura et al. showed that simple theoretical model based on a direct ^{12}C transfer to the molecular resonances could explain the qualitative feature of the structures [13]. Futhermore, systematic measurements of the ($^{16}O,\alpha$) reaction on ^{14}N, ^{16}O, and ^{20}Ne targets performed by Takahashi et al. (see Fig. I-2) showed that prominent broad peaks were observed in the reactions on the ^{16}O and ^{20}Ne targets, while they were absent on the ^{14}N target [14]. Following this fact, they suggested that it is hardly believed that the sequential α decay process of the $^{16}O^*$ has responsibility to the structures.

Recently, Szanto de Toledo et al. [15] proposed a completely different interpretation for the observation of these structures. They claimed that the structures are an extension of the ^{24}Mg yrast sequence populated by the well understood high-spin selectivity [16] of α-particle evaporation from ^{28}Si compound nucleus. To check their idea, we performed a measurement of the $^{14}N(^{14}N,\alpha)$ reaction at an $E_{lab}(^{14}N)$=111 MeV, which leads to similar compound nucleus ^{28}Si as the $^{12}C(^{16}O,\alpha)$ reaction at an $E_{lab}(^{16}O)$=145 MeV [17]. The resultant α inclusive spectrum did not show any distinct structures which were observed in the $^{12}C(^{16}O,\alpha)$ reaction (see Fig. I-3). In fact, the theoretical analysis by using the Hauser-Feshbach formalism with a normal level density formula shows that α-particles evaporated from ^{28}Si compound nucleus have only smooth spectra and that the observed continuum background might mainly come from compound process. This fact pointed out that the structures could not be coming from the compound process, contrary to the suggestion of Szanto de Toledo et al. [15].

Fig. I-2. Energy spectra of the ($^{16}O,\alpha$) reaction on various targets: each spectrum is identified by target. (From ref. [14].)

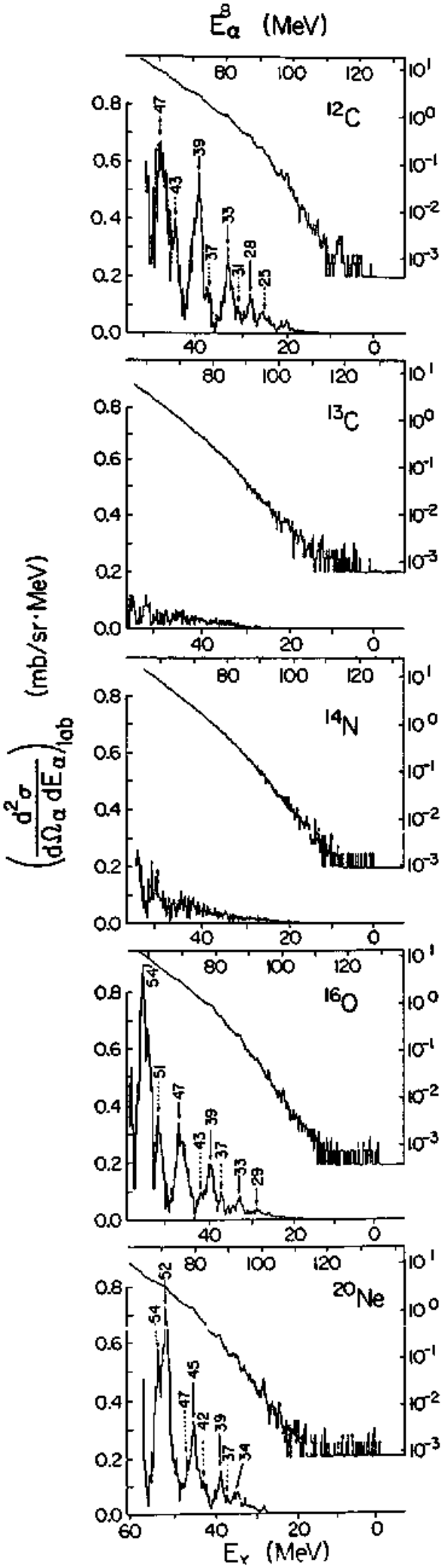
E_α^B (MeV)
^{12}C
^{13}C
^{14}N
^{16}O
^{20}Ne
$\left(\frac{d^2\sigma}{d\Omega_\alpha\, dE_\alpha}\right)_{lab}$ (mb/sr·MeV)
E_γ (MeV)

Fig. I-3. Energy spectra of the $^{12}C(^{16}O,\alpha)$ at 145 MeV and $^{14}N(^{14}N,\alpha)$ at 111 MeV. The raw spectra are displayed in the logarithmic scale, while the background subtracted spectra are shown in the linear scale. The solid lines show the theoretical spectra of the one-step compound evaporations, and the dashed lines show the multi-step results. (From ref. [17].)

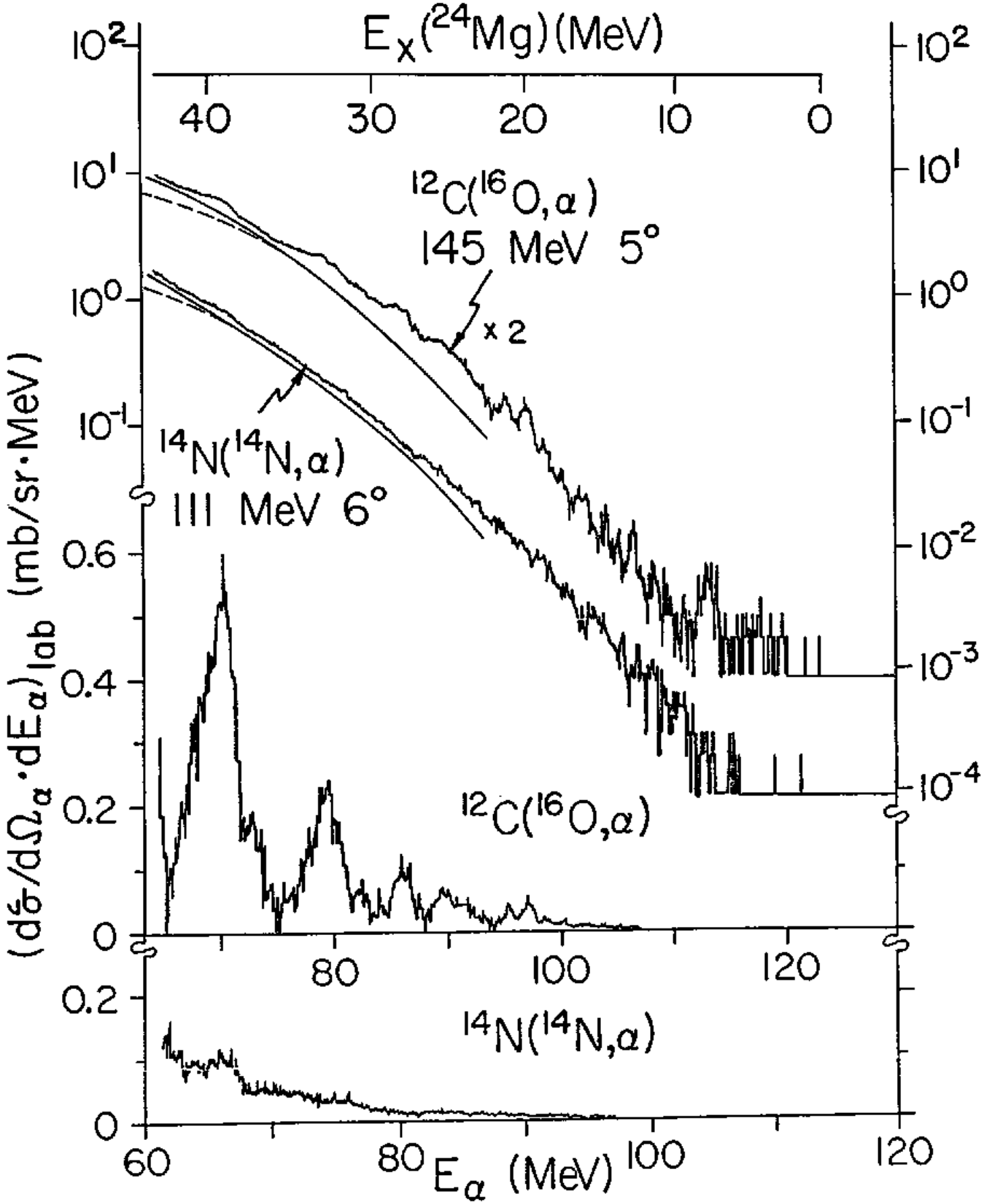
$E_x(^{24}Mg)$(MeV)
40
30
20
10
0
10^2
10^1
10^0
10^{-1}
$^{12}C(^{16}O,\alpha)$
145 MeV 5°
x 2
$^{14}N(^{14}N,\alpha)$
111 MeV 6°
10^{-2}
10^{-3}
10^{-4}
$(d\sigma/d\Omega_\alpha \cdot dE_\alpha)_{lab}$ (mb/sr·MeV)
0.6
0.4
0.2
0
$^{12}C(^{16}O,\alpha)$
80
100
120
0.2
0
$^{14}N(^{14}N,\alpha)$
60
80
E_α (MeV)
100
120

Though already many investigations concerning the $^{12}C(^{16}O,\alpha)$ reaction have been performed as mentioned above, there is still no direct evidence to draw a conclusion whether the $^{12}C(^{16}O,\alpha)$ reaction can populate the molecular resonances or not. To understand the origin of the structures in the single α-spectrum of the $^{12}C(^{16}O,\alpha)$ reaction, we have carried out a series of experiments. For convenience, we will present details about those experiments independently. In chapter II, experimental procedures, results and short discussion about the coincidence measurement of the $^{12}C(^{16}O,\alpha^{12}C)$ reaction are presented. The results of this measurement cast strong doubt about the population of the nuclear molecular states as final states of the $^{12}C(^{16}O,\alpha)$ reaction. Then we describe the incident energy dependence of the $^{12}C(^{16}O,\alpha)$ reaction in chapter III, that shows an importance of the other processes. In chapter IV, details about the $^{16}O(^{12}C,^{8}Be)^{20}Ne$ reaction measurement are presented. The results of this measurement confirm the importance of sequential α-decay process of a $^{20}Ne^{*}$ in the $^{12}C(^{16}O,\alpha)$ reaction. The comprehensive discussion, which makes the relation of three experiments clear, will be described in chapter V. The summary of the present work will be given in chapter VI.

II. COINCIDENCE MEASUREMENT OF THE $^{12}C(^{16}O,\alpha^{12}C)$ REACTION

A. Introductory Remarks

As we already mentioned in the previous chapter, in order to pin down the origin of the structures we have to measure much kinematically complete quantities. If the structures are really coming from the nuclear molecular resonances, large portions of them should decay into $^{12}C(g.s.)+^{12}C(g.s.)$, $^{12}C(g.s.)+^{12}C(2^+)$ and $^{12}C(2^+)+^{12}C(2^+)$ channels, because the high-spin molecular resonances are expected to have large ^{12}C-decay widths [7]. First attempt to measure the ^{12}C-decay of these structures by Rae at el. [11] not necessarily had an ideal setting for this purpose. The reaction processes:

$$
\begin{array}{lll}
^{12}C + {}^{16}O \longrightarrow {}^{24}Mg^* + \alpha & & \\
\qquad\qquad\quad \longrightarrow {}^{12}C(g.s.) + {}^{12}C(g.s.) & & \\
\qquad\qquad\quad \longrightarrow {}^{12}C(g.s.) + {}^{12}C(2^+) & & [I] \\
\qquad\qquad\quad \longrightarrow {}^{12}C(2^+) + {}^{12}C(2^+) , & &
\end{array}
$$

which we want to measure, evidently have competing processes:

$$
\begin{array}{lll}
^{12}C + {}^{16}O \longrightarrow {}^{12}C(g.s.) + {}^{16}O^* & & \\
\qquad\qquad\qquad\quad \longrightarrow {}^{12}C(g.s.) + \alpha & & \\
\qquad\qquad\qquad\quad \longrightarrow {}^{12}C(2^+) + \alpha & & \\
\longrightarrow {}^{12}C(2^+) + {}^{16}O^* & & [II] \\
\qquad\qquad\qquad\quad \longrightarrow {}^{12}C(g.s.) + \alpha & & \\
\qquad\qquad\qquad\quad \longrightarrow {}^{12}C(2^+) + \alpha & &
\end{array}
$$

The processes [I] and [II] have exactly same final states, so there is no way to distinguish them by taking coincidence data at only one angle set. Usually the first reaction steps of processes [II]; i.e. inelastic

scatterings, show quite forward peaked angular distributions. Moreover, their cross sections are likely to become smaller as the excitation energy of the ejectile ^{16}O is getting larger. On the other hand, the decay process of $^{24}Mg^*$ is not supposed to have a very strong angular dependence. These general features imply that if the α and ^{12}C particles are measured at forward angles with a small relative angle separation, the processes [II] are selectively observed as in the case of Rae et al. [11]. On the other hand, if the α and ^{12}C particles are measured at very forward and backward angles, respectively, the contribution of the processes [II] should become smaller, and then we might be able to observe the processes [I] much easily. Therefore we have attempted to carry out α-^{12}C coincidence measurements using one α- and two ^{12}C-counters with such geometries. Though ^{12}C-^{12}C coincidence data at an one angle set does not have a broad range in terms of the excitation energy of a ^{24}Mg, we have also taken ^{12}C-^{12}C coincident events at the same time, because our preliminary experiment showed that the α-^{12}C coincident events have a very small counting rate.

B. Experimental Procedures

The experiment was performed by using a 146.2 MeV $^{16}O^{4+}$ beam extracted from the Texas A&M University 224 cm variable energy cyclotron. After analyzed by a 160° analyzing magnet, the beam was focused on a 475 $\mu g/cm^2$ natural carbon target positioned at a center of the 40 cm-diameter scattering chamber. Since $^{12}C^{3+}$ beam has nearly same rigidity as $^{16}O^{4+}$ one, special care was taken to separate them. The target thickness was measured by an energy loss of an ^{241}Am α source.

The incident energy was estimated to be 145.5 MeV at the center of the target. The size of the beam spot was kept less than 3 mm in height and 2 mm in width to minimize ambiguity of detecting angles. Under this condition, the typical beam intensity was 100 nA (current) on the target.

A schematic view of the detection system used for the experiments is shown in Fig. II-1. Alpha particles were momentum analyzed by the Enge split-pole magnetic spectrometer (we note this LI counter) and then detected by using an 86 cm-long position-sensitive proportional counter backed by a plastic scintillator (see Fig. II-2(a)). A single rectangular slit, which subtended a solid angle of 1.28 msr and an angle of ±1.0°, was used for a collimation of the spectrometer. This slit was also used as a Faraday cup. To reduce effects of secondary-α produced by elastically scattered $^{16}O^{6+}$ particles at the entrance window of the focal plane counter, a thin Kapton foil was inserted between the two dipole magnets as an electron stripper and a thin brass foil was set just in front of the detector as a stopper. (see Fig. II-1) Two silicon surface barrier counter telescopes were used to measure heavy particles. One of them (HI1) consisted of 10.9 μm ΔE, 200 μm E, and 1.5 mm veto counters and the other (HI2) consisted of 16.8 μm ΔE, 200 μm E, and 1.5 mm veto counters. The rectangular defining slits for them provided angular acceptances of ±0.5° for both of them and the solid angles of 1.44 msr and 1.67 msr, respectively. The angular openings of the detection systems and the target thickness were chosen so that the different three-body final states in $^{12}C+^{12}C+\alpha$ outgoing channel, Q=-7.16, -11.60 and -16.04 MeV, could be separated at the angle

Fig. II-1. Experimental configuration for the coincidence measurement.

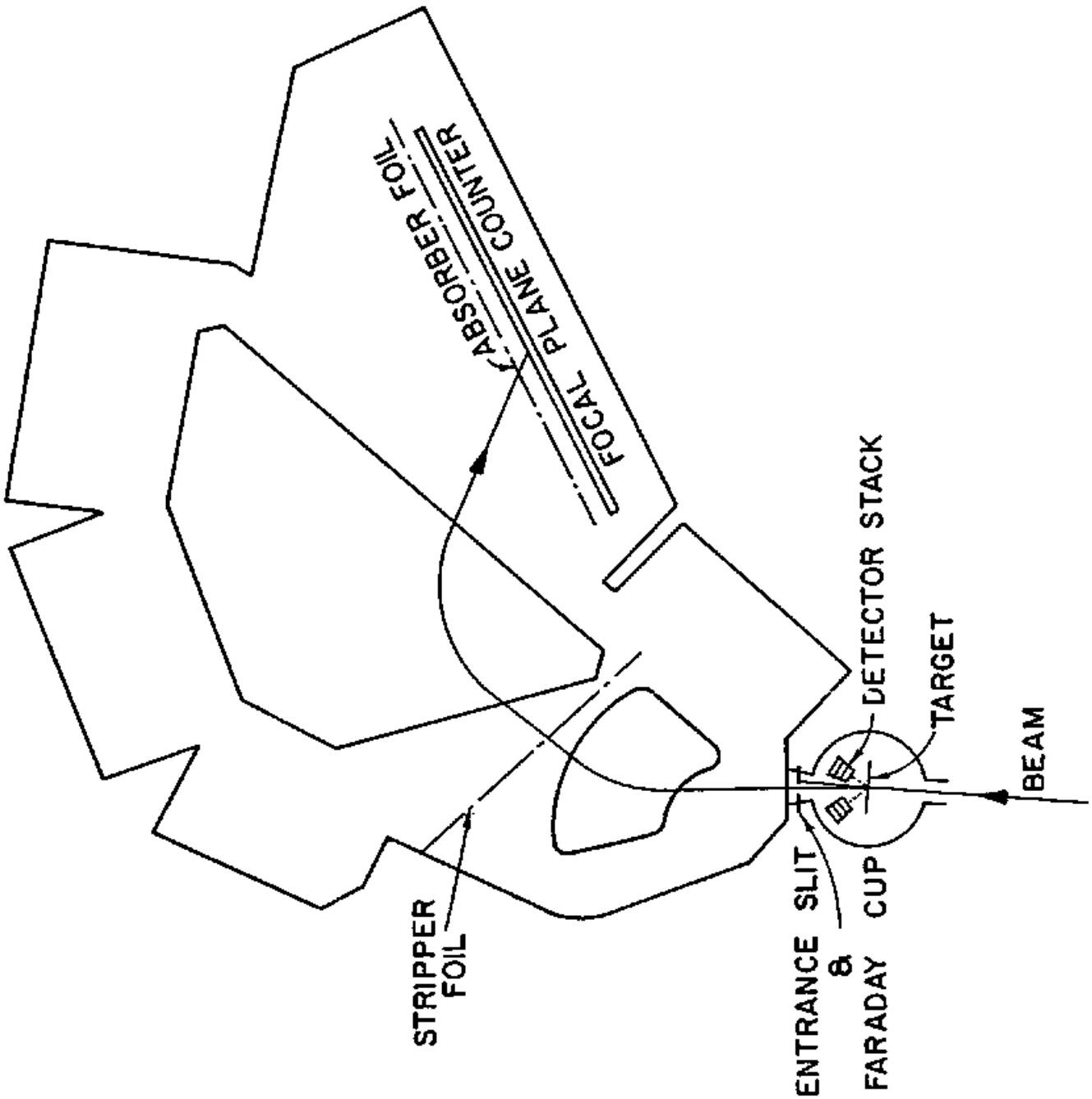
ABSORBER FOIL
FOCAL PLANE COUNTER
DETECTOR STACK
TARGET
BEAM
STRIPPER FOIL
ENTRANCE SLIT & FARADAY CUP

Fig. II-2. Cross sections of the focal-plane counters: (A) for the 86 cm counter and (B) for the 120 cm counter. The bias voltage applied on each electrode is also shown.

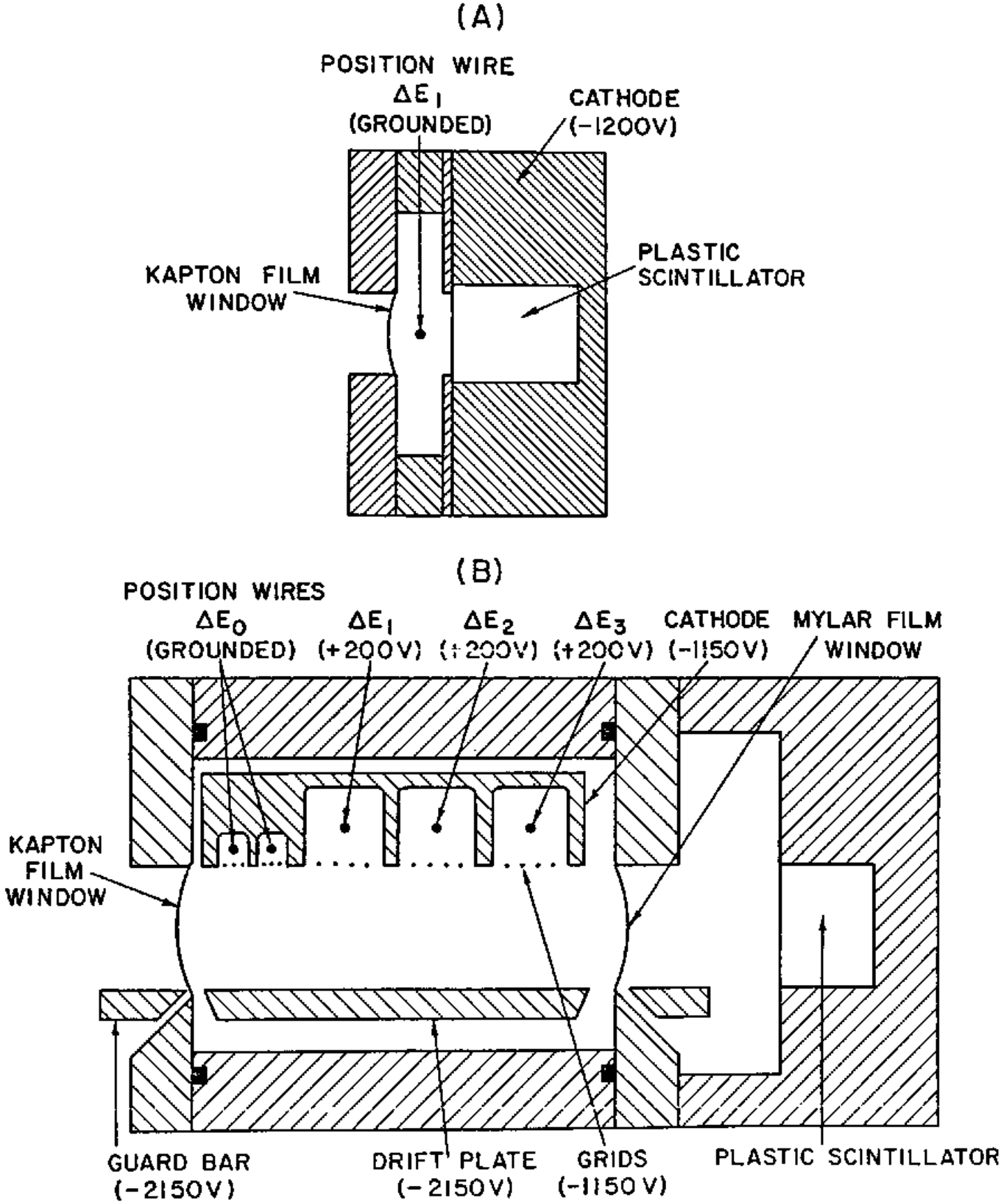
(A)
POSITION WIRE
ΔE1
(GROUNDED)
CATHODE
(-1200V)
KAPTON FILM
WINDOW
PLASTIC
SCINTILLATOR
(B)
POSITION WIRES
ΔE0
(GROUNDED)
ΔE1
(+200V)
ΔE2
(+200V)
ΔE3
(+200V)
CATHODE
(-1150V)
MYLAR FILM
WINDOW
KAPTON
FILM
WINDOW
GUARD BAR
(-2150V)
DRIFT PLATE
(-2150V)
GRIDS
(-1150V)
PLASTIC SCINTILLATOR

where we performed measurements.

Overall energy resolutions of the counter telescopes and the spectrometer were approximatelly 1.2 MeV caused by the large angular opening and the energy loss in the target. Gains of counters were optimized independently and the ratio of them was measured by injecting a same amount of charge into the input stage of the preamplifiers. The energy calibration for the spectrometer was obtained by elastic scatterings of a ^{16}O on a ^{12}C at $\theta_{lab}=4°$ under several magnetic fields and then fitting those data with a quadratic function. For the telescopes, elastic and inelastic scatterings of 109.6 MeV $^{12}C^{3+}$ beam (analogous beam of 146.2 MeV $^{16}O^{4+}$ beam) were used. The total ambiguity of energy calibrations is estimated to be less than ±250 keV.

A block diagram of the electronics used for the measurements is shown in Fig. II-3. The time difference between the scintillator signal and the RF signal of the cyclotron was measured to separate A/z values of particles analyzed by the spectrometer. Here the symbol A and z denote mass and atomic charge of the detected particle respectively. Four different types of coincident events, namely LI-HI1, LI-HI2, HI1-HI2, and LI-HI1-HI2, were obtained from the three detection systems. The event type was distinguished by the bit pattern of DCB (Discriminator Coincidence Buffer unit). For each coincident event, eight parameters, i.e. DCB output, Hρ, Hρ+Lρ, ΔE(HI1), E(HI1), ΔE(HI2), E(HI2), and sum of TAC (Time-to-Amplitude Converter) outputs, were processed by a VAX-11/780 on-line computer and stored on a magnetic tape event by event for the later analysis. Here the Hρ and Lρ denote the two signals from the position counter in the spectrometer. One of

Fig. II-3. Block-diagram of the electronics set up. Abbreviations are as follows:

PA	Preamplifier
SA	Spectroscopic amplifier
TFA	Timing filter amplifier
CFD	Constant fraction discriminator
DCM	DC-mixer
TSCA	Timing single channel analyzer
TAC	Time to amplitude converter
PUI	Pile up inspector
COIN	Universal coincidence
DA	Delay amplifier
GDG	Gate and delay generator
LGS	Linear gate and stretcher
SUM	Summing amplifier
ADC	Analog to digital converter
DCB	Discriminator coincidence buffer

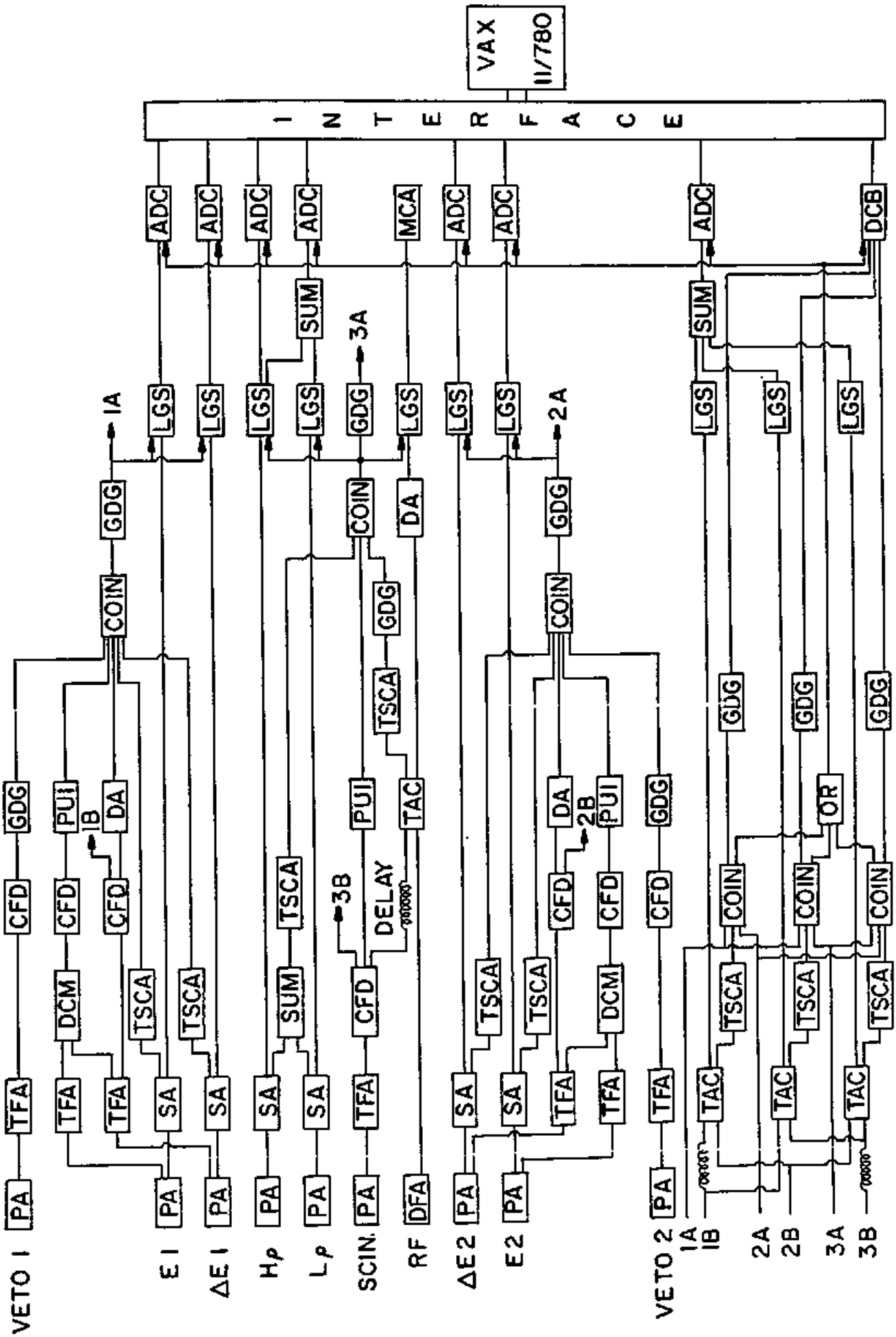
VAX 11/780
INTERFACE
ADC
MCA
DCB
SUM
LGS
GDG
COIN
DA
PUI
DCM
TSCA
TAC
CFD
TFA
SA
PA
DFA
DELAY
OR
1A
1B
2A
2B
3A
3B
VETO 1
E 1
ΔE 1
Hp
Lp
SCIN.
RF
ΔE 2
E 2
VETO 2

them is from the higher momentum side and the other is from the lower momemtum side, respectively.

The measurements were carried out at two angle sets, namely θ_{LI}=4°, θ_{HI1}=39.5° and θ_{HI2}=-34.5°, and θ_{LI}=4°, θ_{HI1}=39.5° and θ_{HI}=-39.0°, where the negative angles specify the opposite side of the beam axis from the spectrometer. These geometries of the measurements were chosen under following considerations. First, the most forward angle for the α detection where we can measure particles without any background problem is θ_{lab}=4° using the spectrometer. Second, the most backward angle for the meaningful ^{12}C detection corresponds to the perpendicular decay of $^{24}Mg^*$ to its recoil direction, because beyond this angle the companion ^{12}C has smaller separation angle from the α-particle than the detected ^{12}C in the center-of-mass system. When α-particles are detected at θ_{lab}=4°, these angles for the 12^+, 14^+ and 16^+ states ($E_x(^{24}Mg)$~33, 39 and 47 MeV) in the laboratory system are θ_{lab}~39.3°(-36.8°), 35.7° (-34.6°) and 42.7°(-38.7°), respectively. The typical coincidence counting rates for LI-HI1, LI-HI2, and HI1-HI2 events are 0.2, 0.1 and 0.3 counts/sec., respectively, while the single counting rates for LI and HI1 are 2K and 200 cps.

C. Experimental Results

The accumulated event-by-event data were sorted by selecting the event type and making particle identifications, for example ΔE versus E two-dimensional plots for the counter telescopes and a $M^2=(H\rho+L\rho)*(H\rho/(H\rho+L\rho)+0.5)^2$ mass square spectrum for the spectrometer with an off-line VAX-11/780 computer system. Large difference of three-body

Q-values between $^{12}C+^{12}C+\alpha$ and other channels gave us unambiguous identification of the reaction channel, though we could not get good isotopic identification from ΔE-E plots because of too thin ΔE detectors. The contribution of chance coincident events were reduced by using information of the TAC output.

As a typical example of two-dimensional spectra, the $E12_C$ versus $E12_C$ scatter plot of 39.5° and -34.5° angle set is shown in Fig. II-4. In this spectrum, kinematic loci associated with $^{12}C+^{12}C+\alpha$ final states with Q-values -7.16, -11.60 and -16.04 MeV are clearly separated in the high energy region of two ^{12}C particles. On the other hand, we could not get a clear separation of them in the low energy region. In the E_α versus $E^{12}C$ spectrum the loci themselves were ambiguous. However, by making an one-dimensional Q-value plot following the relation of the three-body kinematics summarized in Appendix A, we could identify them at least for the α-^{12}C coincidence data. A typical example of the Q-value plots is shown in Fig. II-5. This figure also shows the poor statistics of the data. Even after subtracting chance coincident events by using the TAC information we can see several peaks in the kinematically forbidden region Q>-7.16 MeV. This is due to the poor counting rate of both true and chance coincident events and the bad yield ratio (worse than 1 to 1) between them. It is worth while noting that the Q~-16.04 MeV locus not necessarily corresponds to $^{12}C(2^+)+^{12}C(2^+)+\alpha$ final state, because final states $^{12}C(g.s.)+^{12}C(0^+;7.65\ MeV)+\alpha$ and $^{12}C(g.s.)+^{12}C(3^-;9.64\ MeV)+\alpha$ have similar Q-values and our energy resolution in the Q-value spectrum was not good enough to separate those states. Nevertheless we will refer that as $^{12}C(2^+)+^{12}C(2^+)+\alpha$ for

Fig. II-4. Two-dimensional energy spectrum between ^{12}C-^{12}C coincidence at $\theta^{12}C_1$=39.5° and $\theta^{12}C_2$=-34.5°. Count in each channel is indicated by the density of dots.

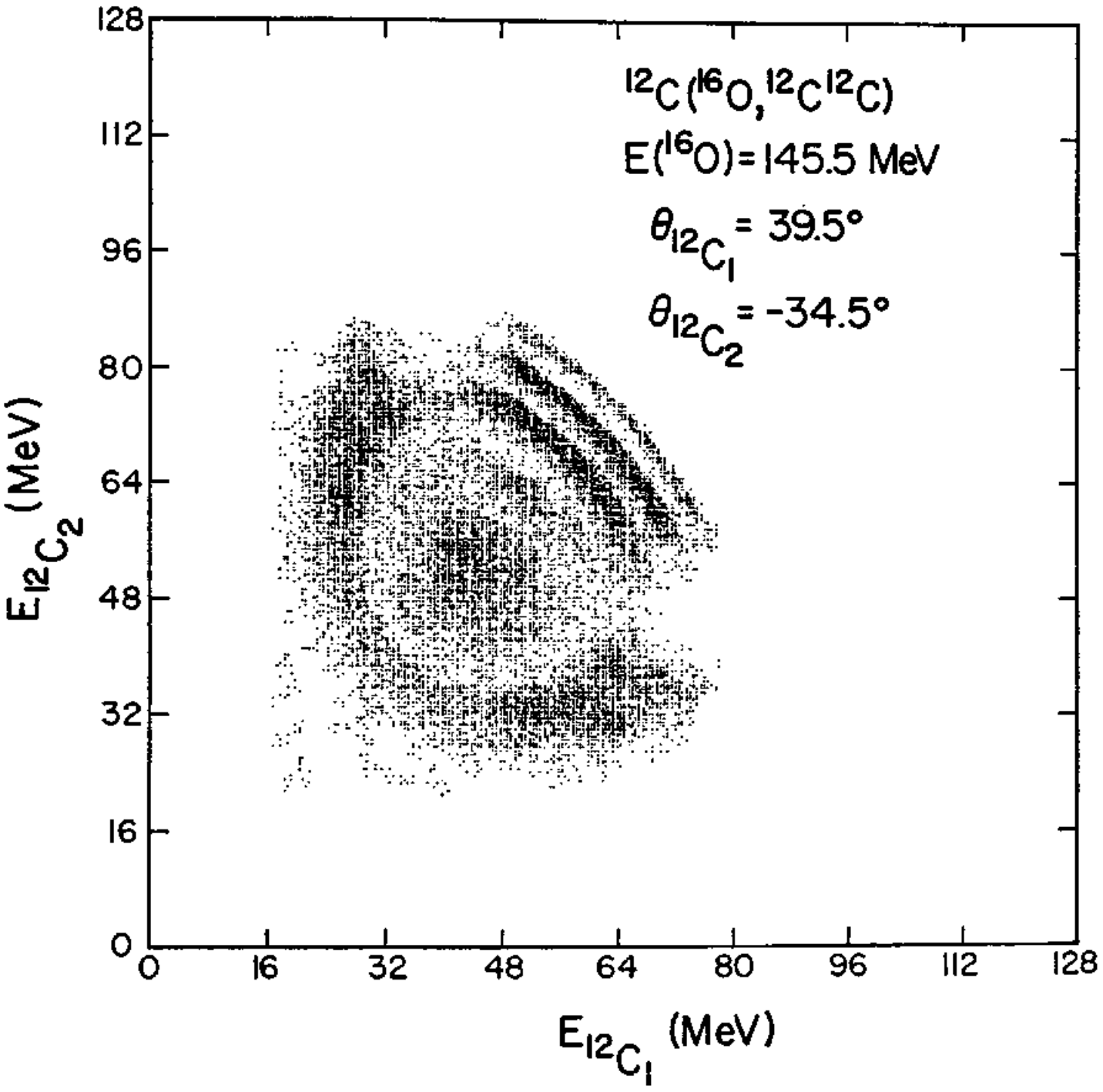
$^{12}C(^{16}O,^{12}C^{12}C)$
$E(^{16}O) = 145.5$ MeV
$\theta_{^{12}C_1} = 39.5°$
$\theta_{^{12}C_2} = -34.5°$
$E_{^{12}C_2}$ (MeV)
$E_{^{12}C_1}$ (MeV)
0
16
32
48
64
80
96
112
128

Fig. II-5. Typical Q-value spectrum made by using the three-body kinematics (see Appendix A). Arrows indicate positions of three different final states, namely the $^{12}C(g.s.)+^{12}C(g.s.)+\alpha$, $^{12}C(g.s.)+^{12}C(2^+)+\alpha$ and $^{12}C(2^+)+^{12}C(2^+)+\alpha$.

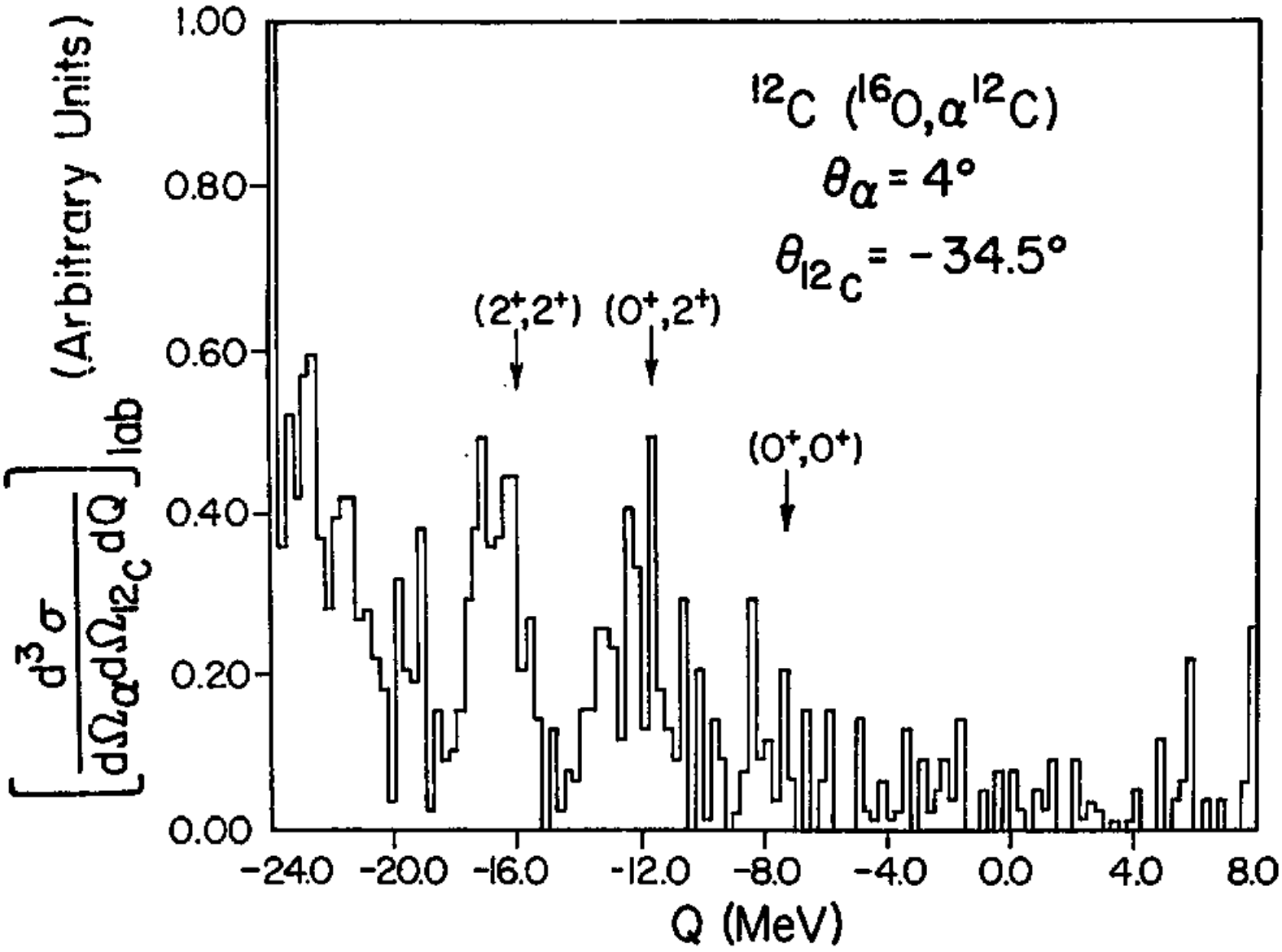
^{12}C (^{16}O,$\alpha^{12}C$)
$\theta_\alpha = 4°$
$\theta_{^{12}C} = -34.5°$
(2+,2+)
(0+,2+)
(0+,0+)
$\left[\frac{d^3\sigma}{d\Omega_\alpha d\Omega_{12_C} dQ}\right]_{lab}$ (Arbitrary Units)
1.00
0.80
0.60
0.40
0.20
0.00
-24.0
-20.0
-16.0
-12.0
-8.0
-4.0
0.0
4.0
8.0
Q (MeV)

brevity. Because we could not separate three different final states in the ^{12}C-^{12}C coincidence data in the low energy region, we will discuss only about the α-^{12}C coincidence data in the following.

Since we are investigating three-body final states, there are in general three possible pairs of two-body residual interactions which should be distinguished. In the present measurements, processes [I] and [II] are expected so that relative kinematic energies of the detected ^{12}C particle and the companion ^{12}C particle, the detected ^{12}C and the α-particle, and the companion ^{12}C and α-particle should be examined. The final results from the α-^{12}C coincidence data sorted according to the Q-value are shown in Figs. II-6~12. Because the α-^{12}C (companion) relative kinematic energy spectra are similar to the α-^{12}C (detected) ones, we do not display them at this time. This resemblance might come from the similar relative angular separations between α and ^{12}C in both cases. To get absolute magnitude of cross sections in the center-of-mass system of the ^{12}C+^{12}C+α three-body system, we used the relations summarized in Appendix A. In the case of relative energy spectra between ^{12}C and ^{12}C, the spectra are compared with a background subtracted single spectrum obtained by the same detection system. For convenience, we renormalize the relative energy spectra between two ^{12}C particles under following assumptions. First, all α-^{12}C coincident events are supposed to be the decay of nuclear molecular states. Second, decay angular distributions of molecular resonances are isotropic. Third, decay branching ratios of them are 0.22, 0.32, and 0.18 for the $^{12}C(g.s.)$+$^{12}C(g.s.)$, $^{12}C(g.s.)$+$^{12}C(2^+)$ and $^{12}C(2^+)$+$^{12}C(2^+)$ channels, respectively. These values have been adopted for the

Figs. II-6-8. Triple differential cross sections for the $^{12}C+^{12}C+\alpha$ channels in the $^{16}O^*$-recoil-center-of-mass system as a function of a relative energy between α and detected ^{12}C. Figures 6, 7 and 8 correspond to g.s.-g.s., g.s.-2^+ and 2^+-2^+ channels, respectively. Typical statistical errors are shown by error-bars.

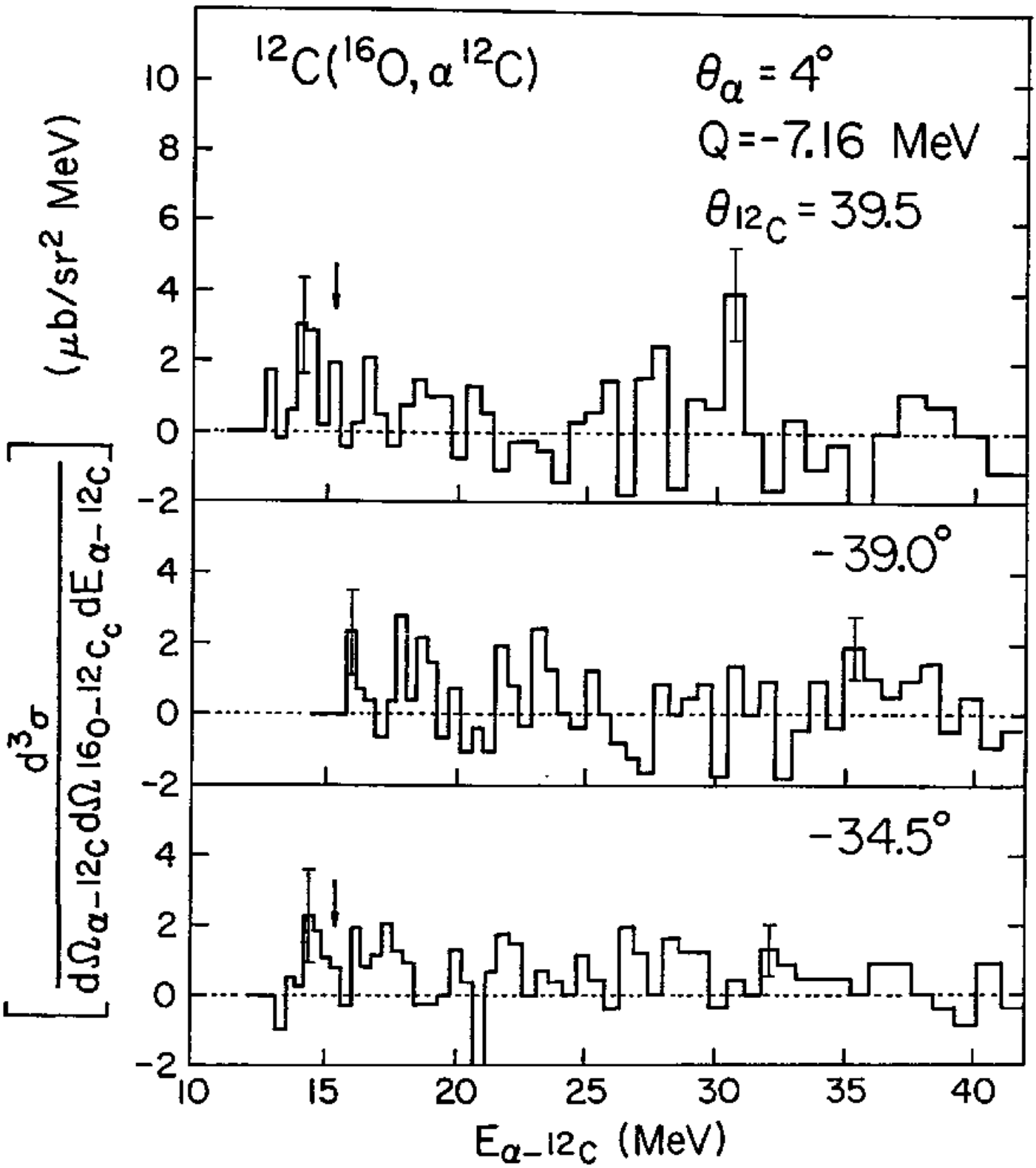
$^{12}C(^{16}O, \alpha\,^{12}C)$
$\theta_\alpha = 4°$
Q=-7.16 MeV
$\theta_{12C} = 39.5$
-39.0°
-34.5°
$\frac{d^3\sigma}{d\Omega_{\alpha-12C}\, d\Omega_{16O-12C}\, dE_{\alpha-12C}}$ (μb/sr^2 MeV)
$E_{\alpha-12C}$ (MeV)

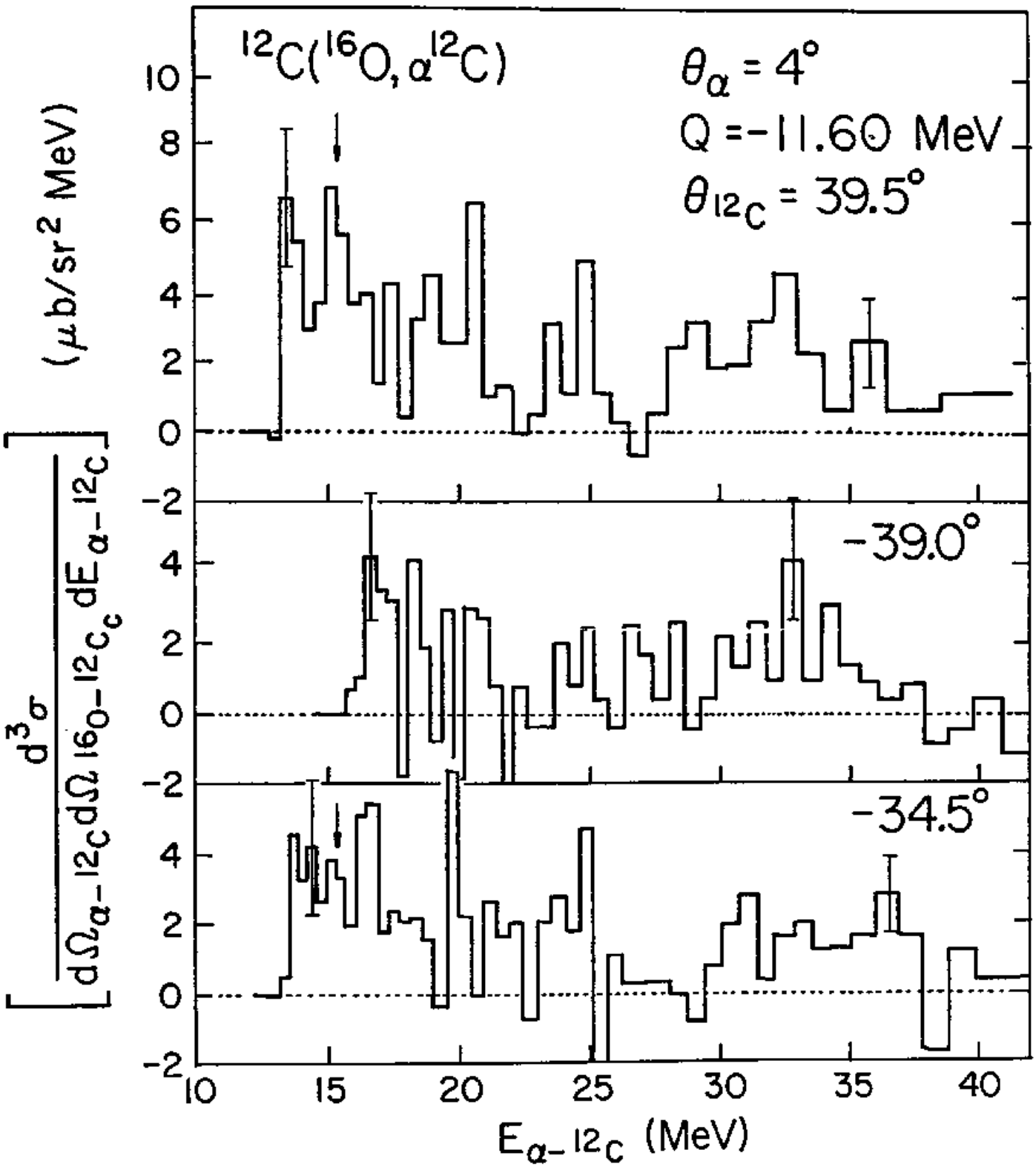
$^{12}C(^{16}O, \alpha^{12}C)$
$\theta_\alpha = 4°$
Q = -11.60 MeV
$\theta_{^{12}C} = 39.5°$
-39.0°
-34.5°
$\frac{d^3\sigma}{d\Omega_{\alpha-^{12}C} d\Omega_{^{16}O-^{12}C_c} dE_{\alpha-^{12}C}}$ (μb/sr^2 MeV)
$E_{\alpha-^{12}C}$ (MeV)

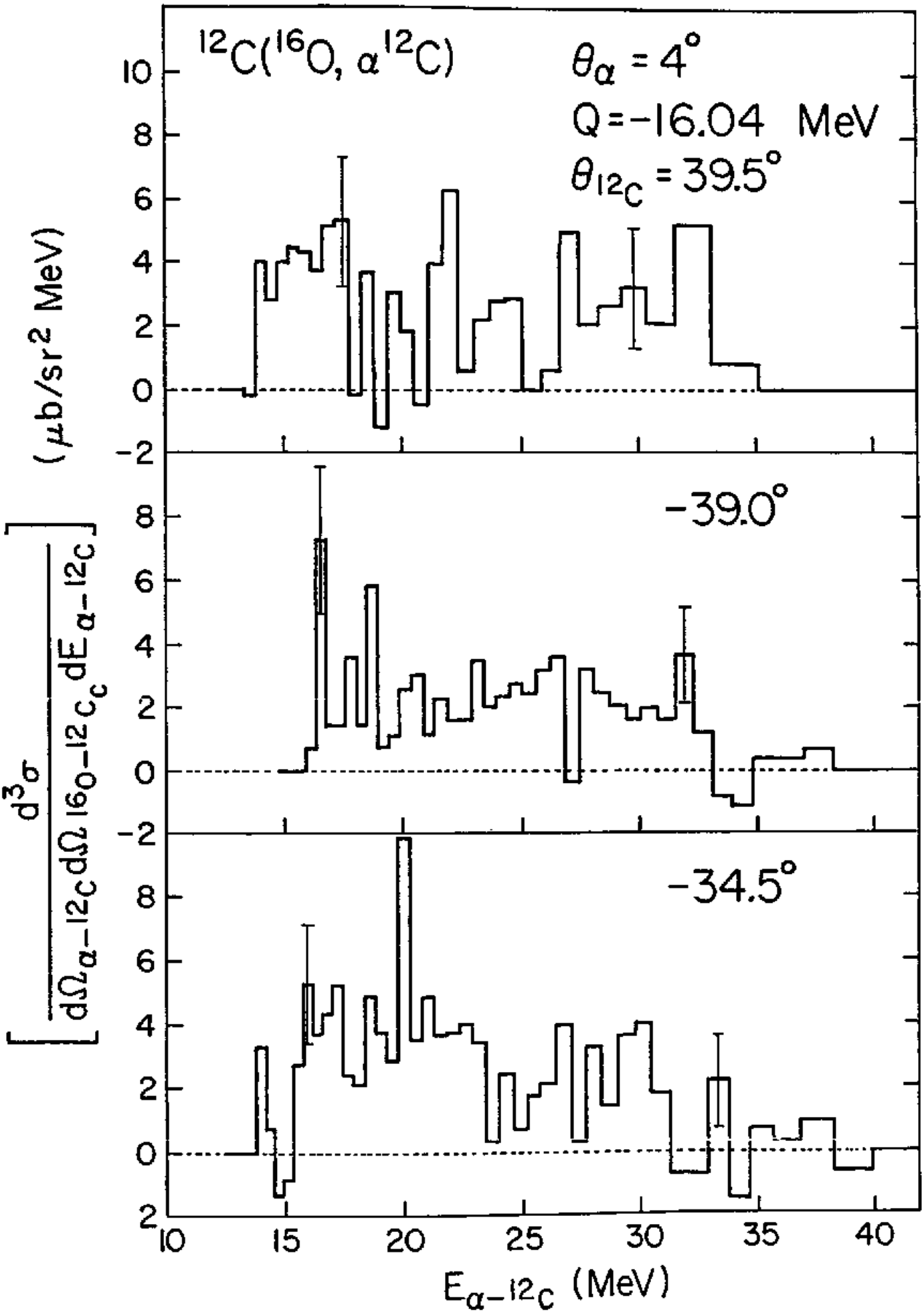
$^{12}C(^{16}O, \alpha^{12}C)$
$\theta_\alpha = 4°$
Q = −16.04 MeV
$\theta_{^{12}C} = 39.5°$
−39.0°
−34.5°
$\left[\frac{d^3\sigma}{d\Omega_{\alpha-^{12}C}\, d\Omega_{^{16}O-^{12}C_c}\, dE_{\alpha-^{12}C}}\right]$ (μb/sr² MeV)
$E_{\alpha-^{12}C}$ (MeV)

Figs. II-9~11. Triple differential cross sections for the $^{12}C+^{12}C+\alpha$ channels in the $^{24}Mg^*$-recoil-center-of-mass system as a function of an excitation energy of the ^{24}Mg. For convenience we multiply those by the factor,

$$A_i = 4\pi * \frac{\Gamma_{tot}}{\Gamma_i} * \frac{2m_{^{12}C} + m_\alpha}{2m_{^{12}C}} \text{ (sr)}, \quad (i;\ c,\ 2^+ \text{ and } 2^+2^+)$$

and compare with a background subtracted single spectrum. Figures 9, 10 and 11 correspond to g.s.-g.s., g.s.-2^+ and 2^+-2^+ channels, respectively. Typical statistical errors are shown by error-bars.

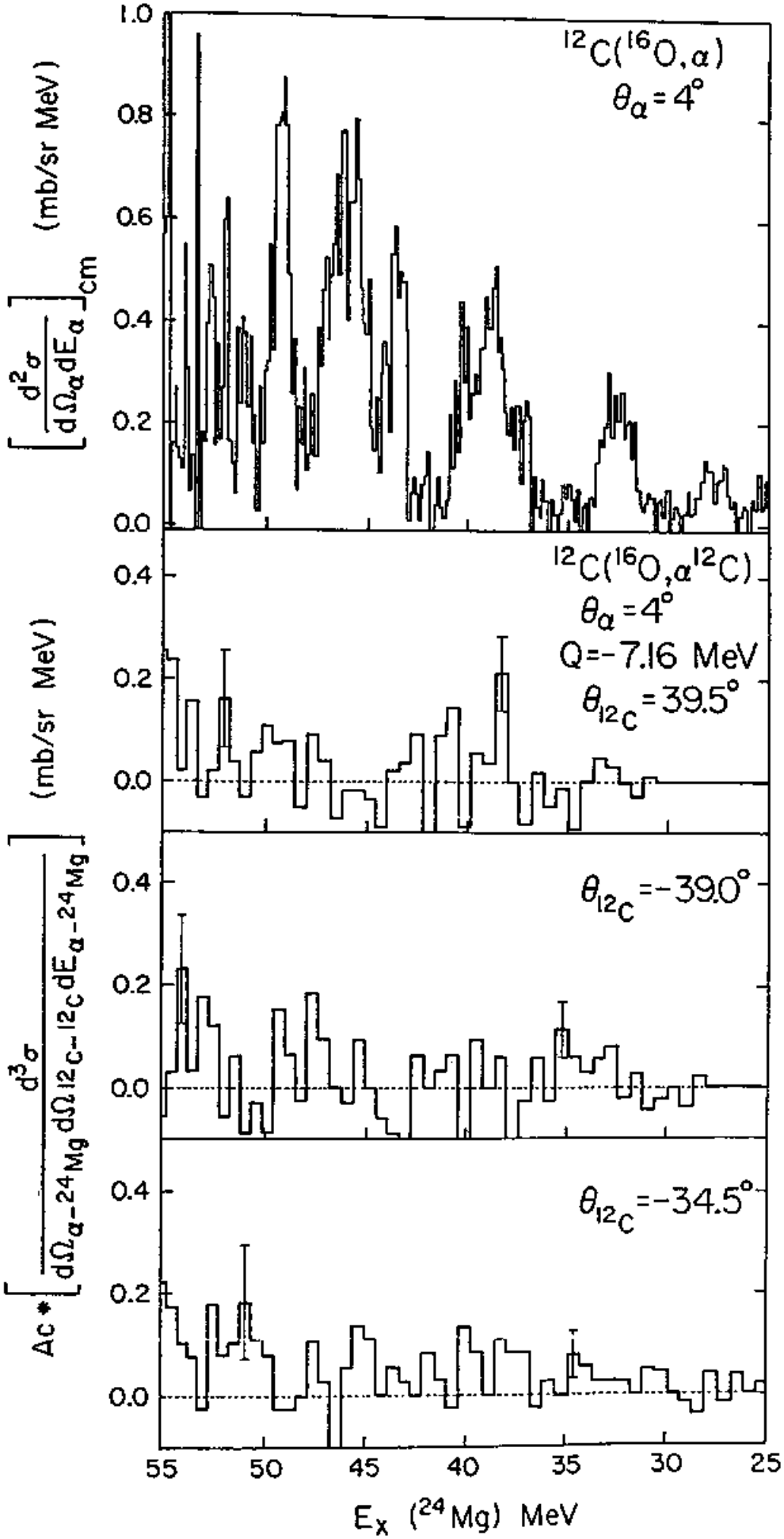
$^{12}C(^{16}O,\alpha)$
$\theta_\alpha = 4°$
$\left[\frac{d^2\sigma}{d\Omega_\alpha dE_\alpha}\right]_{cm}$ (mb/sr MeV)
$^{12}C(^{16}O,\alpha^{12}C)$
$\theta_\alpha = 4°$
Q=-7.16 MeV
$\theta_{^{12}C} = 39.5°$
$\theta_{^{12}C} = -39.0°$
$\theta_{^{12}C} = -34.5°$
$Ac * \left[\frac{d^3\sigma}{d\Omega_{\alpha-^{24}Mg}\, d\Omega_{^{12}C-^{12}C}\, dE_{\alpha-^{24}Mg}}\right]$ (mb/sr MeV)
E_x (^{24}Mg) MeV

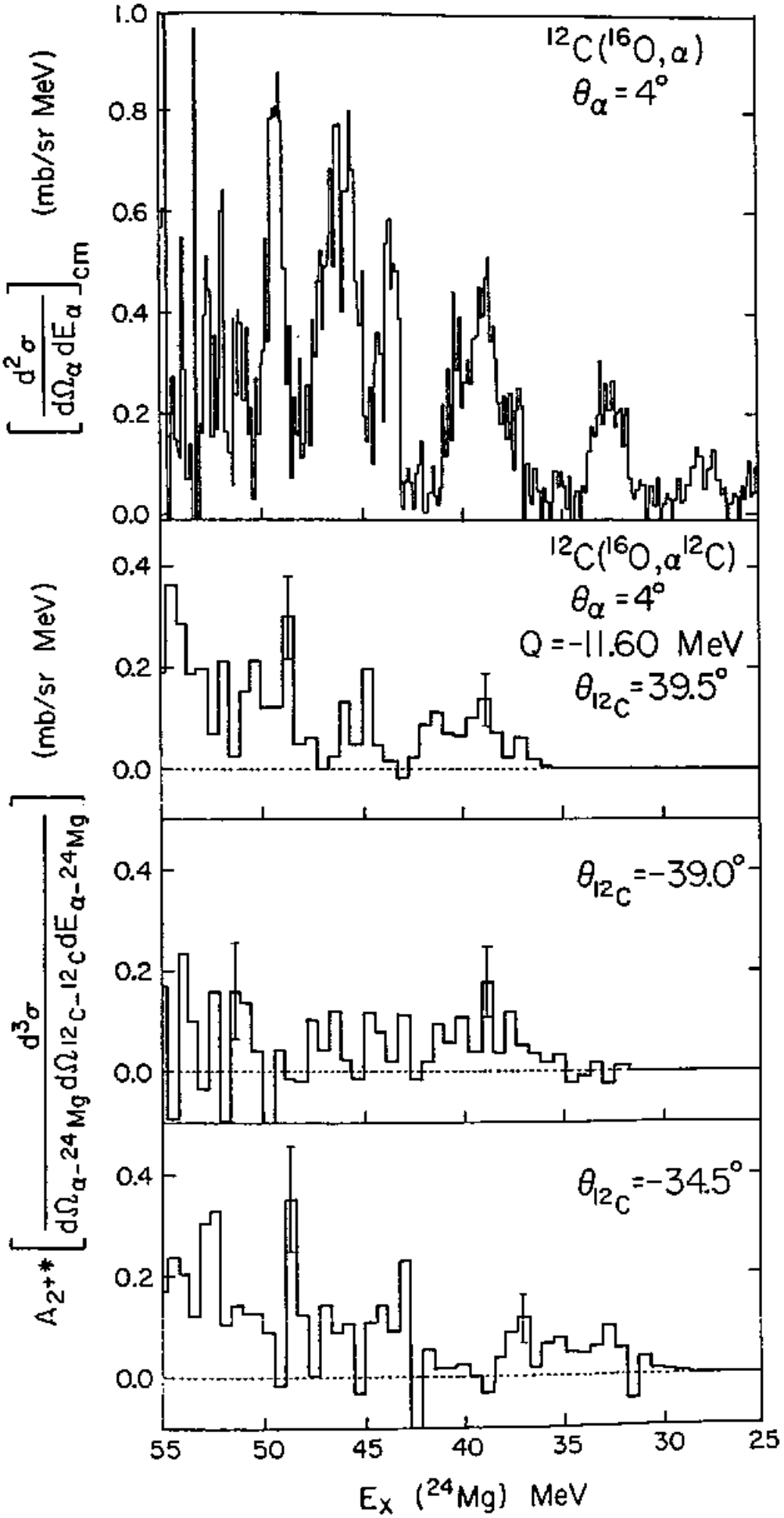
$^{12}C(^{16}O,\alpha)$
$\theta_\alpha = 4°$
$\left[\frac{d^2\sigma}{d\Omega_\alpha dE_\alpha}\right]_{cm}$ (mb/sr MeV)
$^{12}C(^{16}O,\alpha^{12}C)$
$\theta_\alpha = 4°$
Q = -11.60 MeV
$\theta_{^{12}C} = 39.5°$
$\theta_{^{12}C} = -39.0°$
$\theta_{^{12}C} = -34.5°$
$A_{2^+}{}^* \left[\frac{d^3\sigma}{d\Omega_{\alpha-^{24}Mg}\, d\Omega_{^{12}C-^{12}C} dE_{\alpha-^{24}Mg}}\right]$ (mb/sr MeV)
E_x (^{24}Mg) MeV

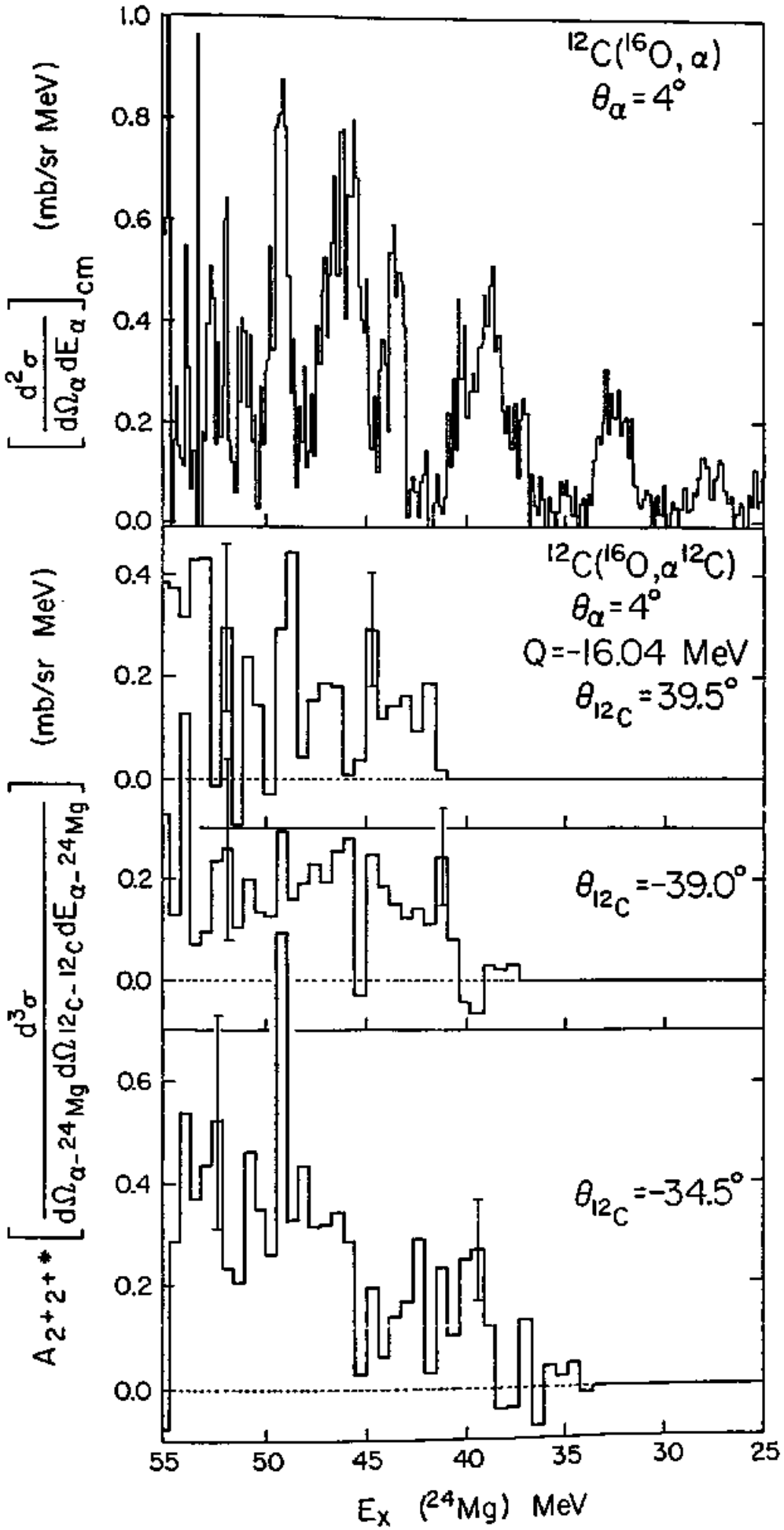
$^{12}C(^{16}O, \alpha)$
$\theta_\alpha = 4°$
$\left[\frac{d^2\sigma}{d\Omega_\alpha dE_\alpha}\right]_{cm}$ (mb/sr MeV)
$^{12}C(^{16}O,\alpha\,^{12}C)$
$\theta_\alpha = 4°$
Q=-16.04 MeV
$\theta_{^{12}C} = 39.5°$
$\theta_{^{12}C} = -39.0°$
$\theta_{^{12}C} = -34.5°$
$A_{2^+2^+}{}^* \left[\frac{d^3\sigma}{d\Omega_{\alpha-^{24}Mg}\, d\Omega_{^{12}C-^{12}C}\, dE_{\alpha-^{24}Mg}}\right]$ (mb/sr MeV)
E_x (^{24}Mg) MeV

Fig. II-12. Triple differential cross sections for $\alpha+^{12}C+X$ channel with the Q-value less than -16.04 MeV in the laboratory system as a function of α energy.

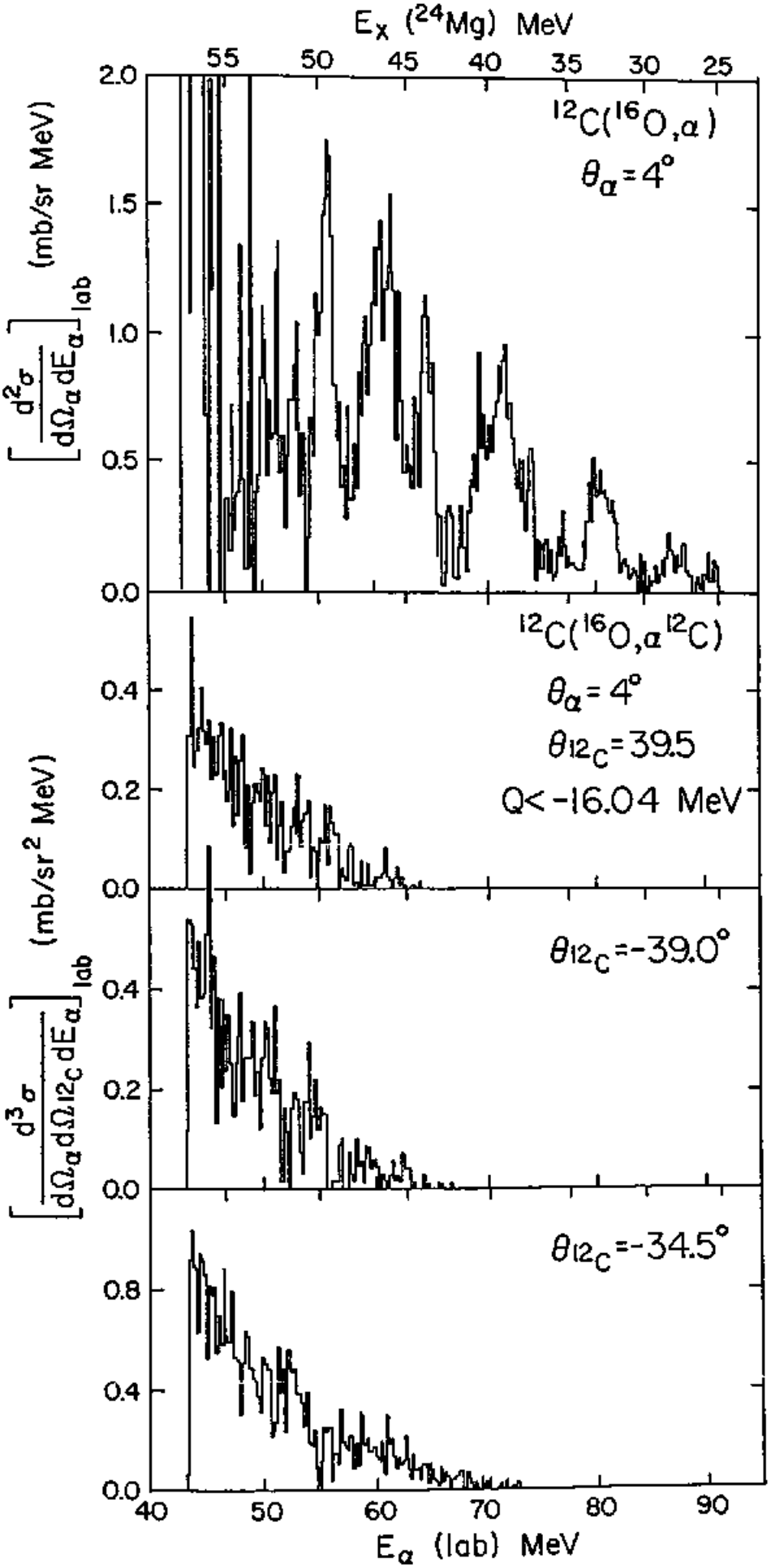
E_x (^{24}Mg) MeV
55
50
45
40
35
30
25
$^{12}C(^{16}O,\alpha)$
$\theta_\alpha = 4°$
$\left[\frac{d^2\sigma}{d\Omega_\alpha dE_\alpha}\right]_{lab}$ (mb/sr MeV)
2.0
1.5
1.0
0.5
0.0
$^{12}C(^{16}O,\alpha\,^{12}C)$
$\theta_\alpha = 4°$
$\theta_{^{12}C} = 39.5$
Q< -16.04 MeV
0.4
0.2
0.0
$\theta_{^{12}C} = -39.0°$
$\left[\frac{d^3\sigma}{d\Omega_\alpha d\Omega_{^{12}C} dE_\alpha}\right]_{lab}$ (mb/sr^2 MeV)
0.4
0.2
0.0
$\theta_{^{12}C} = -34.5°$
0.8
0.4
0.0
40
50
60
70
80
90
E_α (lab) MeV

14^+ state by Cormier et al. [7]. It should be noted that between energy spectra in the center-of-mass system and relative energy spectra there is a difference of scaling factor, $2m_{^{12}C}/(2m_{^{12}C}+m_\alpha)$, in absolute values. To make possible direct comparison between the single spectrum and coincidence spectra, this scaling difference is also included in renormalization factors A_c, A_{2^+} and $A_{2^+2^+}$. Here the subscripts c, 2^+ and 2^+2^+ denote the $^{12}C(g.s.)+ {}^{12}C(g.s)$, $^{12}C(g.s.)+{}^{12}C(2^+)$ and $^{12}C(2^+)+{}^{12}C(2^+)$ channels, respectively. Actual values of A_c, A_{2^+} and $A_{2^+2^+}$ are 3.23, 4.69 and 2.64 steradian, respectively.

D. Discussion

As seen in the α-^{12}C relative energy spectra (Figs. II-6-8). it is very hard to identify correlated peaks at different angle pairs, in contrast with the results of the coincidence measurements with ^{12}C detectors at relatively forward angle [11]. In these figures, we put arrows at the position corresponding to $E_x(^{16}O)$=22.5 MeV, which is the highest relative energy peak in the reported coincident spectra [18]. Absence of the correlated peaks in the α-^{12}C relative energy spectra can be understood by the fact that the relative energies and scattering angles of the center-of-mass of α and ^{12}C systems are too large to have a visible cross sections.

Even in the relative energy spectra between two ^{12}C particles, there is few statistically meaningful peaks, as seen in the Fig. II-9-12. This fact is more clearly seen in the ^{12}C-^{12}C relative energy spectra averaged over three ^{12}C detection angles 39.5°, -39.0° and -34.5° (see Fig. II-13). In this figure arrows indicate the region where three angle data are unavailable. Even if we assume that all

Fig. II-13. Averaged triple differential cross sections over three observed angles for the $^{12}C+^{12}C+\alpha$ channels in the $^{24}Mg^{*}$-recoil-center-of-mass system as a function of an excitation energy of the ^{24}Mg. Typical statistical errors are shown by error-bars.

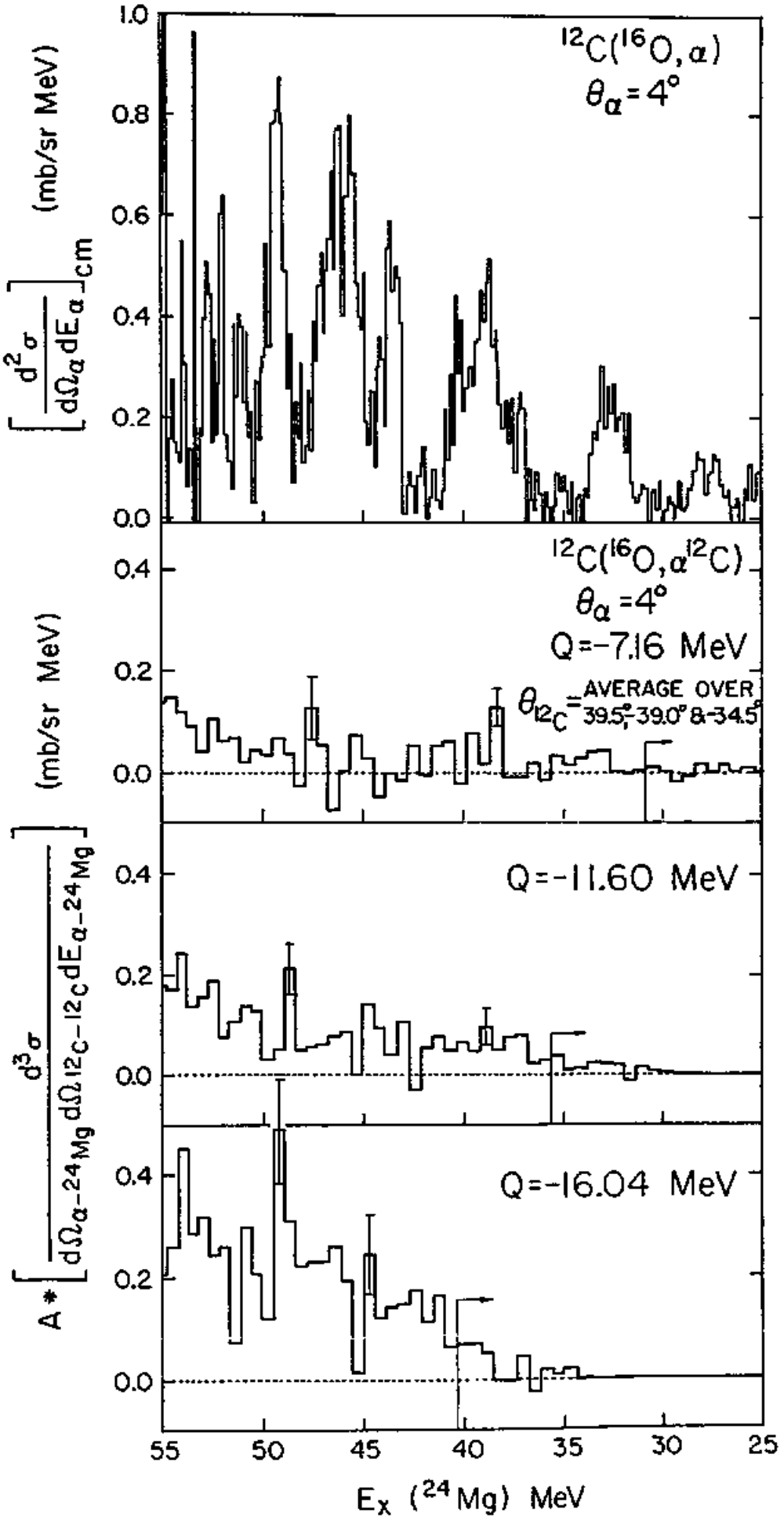
$^{12}C(^{16}O,\alpha)$
$\theta_\alpha = 4°$
$\left[\frac{d^2\sigma}{d\Omega_\alpha dE_\alpha}\right]_{cm}$ (mb/sr MeV)
$^{12}C(^{16}O,\alpha^{12}C)$
$\theta_\alpha = 4°$
Q=-7.16 MeV
$\theta_{^{12}C}$ = AVERAGE OVER 39.5°-39.0° & 34.5°
(mb/sr MeV)
Q=-11.60 MeV
Q=-16.04 MeV
$A^* \left[\frac{d^3\sigma}{d\Omega_{\alpha-^{24}Mg}\, d\Omega_{^{12}C-^{12}C}\, dE_{\alpha-^{24}Mg}}\right]$
E_x (^{24}Mg) MeV

coincident α-^{12}C events correspond to the decay of the molecular resonances, their magnitudes are less than 1/5 of the structures in the single spectrum except for the structure at Ex(^{24}Mg) ~ 49 MeV in the $^{12}C(2^+)+\ ^{12}C(2^+)$ channel. However there is no report that the molecular resonance is observed in this channel at this energy. It should be noted that the above argument about the magnitudes of the structures very much depends on the angular distribution of the decay process of $^{24}Mg^*$. For example, if we assume the decay is axially symmetric about the recoil direction of $^{24}Mg^*$ but has a $1/\sin\theta$ angular distribution with respect to the recoil direction, we can get approximately 60% larger yield ratio between the single and coincidence. But, in both cases, coincident yield can reproduce less than 1/3 of the magnitudes of the structures in the single spectrum.

In summary of this chapter, though we chose more suitable geometry to measure a $^{12}C+^{12}C$ final state interaction than the previous attempt [11], the present coincidence experiments could not reveal it. Possible explanations for this might be summarized as follows:

(i) The structures seen in the α-single experiments originate not from the population of the $^{12}C+^{12}C$ molecular resonances but from other processes like a sequential decay of $^{16}O^*$ proposed by Rae et al. [11].

(ii) The levels in ^{24}Mg populated by a direct ^{12}C transfer reaction on the ^{12}C target have smaller ^{12}C-decay branching ratio than we expected and thus do not contribute much to the coincident yield.

However poor statistics of our data prevent us from drawing a definite conclusion from the present coincidence measurements.

III. INCIDENT ENERGY DEPENDENCE OF THE $^{12}C(^{16}O,\alpha)$ REACTION

A. Introductory Remarks

The results of the coincidence measurements revealed difficulties to tell which reaction mechanism is responsible to the structures, because of the poor statistics. As the other way to separate the different reaction mechanisms, we can conceive careful measurements of the kinematical feature of the structures. It is, however, almost impossible to extract useful information from angular distributions of the structures, since they were not observed clearly at $\theta_{lab} > 15°$ [5]. Considering these facts, we decided to study the energy dependence of the inclusive α spectra of $^{12}C(^{16}O,\alpha)$ reactions in a broad incident particle energy range. We expected that these measurements would make clear following points. First, as the structures due to sequential α decay of the projectile and those due to ^{24}Mg final states follow three-body and two-body kinematics respectively, energy dependence measurement should clearly distinguish those mechanisms. Second, if the structures follow the two-body kinematics, variations of their cross sections as a function of the incident beam energy should provide us good information to separate compound and direct reaction processes. Our results, discussed below, clearly show that most of the prominent structures in the inclusive α spectra do not belong to ^{24}Mg final states but rather to sequential α decays of the ejectiles.

B. Experimental Procedures

The experiments were performed by using the $^{16}O^{4+}$ and $^{16}O^{5+}$ beams at incident energies of E_{lab}=112-191 MeV extracted from the Texas A&M University 224 cm variable energy cyclotron and analyzed by the 160° analyzing magnet. Again in the case of $^{16}O^{4+}$ beam, special care was taken to separate the $^{12}C^{3+}$ component, which has nearly same rigidity as $^{16}O^{4+}$ beam, and results were carefully compared with those of $^{16}O^{5+}$ beam. The incident beam energies were determined by using the calibration formula of the analyzing magnet, which we obtained previously via cross-over technique. The ambiguity of beam energies was estimated to be ±200 keV. The beam was focused on a 157 $\mu g/cm^2$ natural carbon target positioned inside the 40cm-diameter scattering chamber. The target thickness was measured by the energy loss method using the solid state detector with an ^{241}Am α source. The energy loss of the incident beam in the target was estimated to be 450 keV, which might be sufficient to average over statistical fluctuations in cross sections. The size of the beam spot was kept less than 3 mm in diameter. Because the structures which we were interested in were on the huge continuum background, the effect of the stray beams were examined by using a blank target frame from time to time. The results showed no serious contribution from them. Average beam currents on the target were restricted to less than 120 nA (current) in order to minimize the dead time of the acquisition system.

The detection of α-particle at 4° was accomplished by using the Enge split-pole magnetic spectrometer with a 120 cm-long focal plane detector [19] (see Fig. II-2(b)). In order to get a fast timing signal

for a time-of-flight (TOF), a plastic scintillator was installed as a backup counter just behind the focal plane counter. The acceptance of the spectrometer was defined by a single rectangular slit at the entrance. The entrance slit was also used as a Faraday cup. The solid angle and horizontal acceptance were 1.28 msr and ±1.0°, respectively. To minimize the influence of the secondary-α caused by elastically scattered $^{16}O^{6+}$ particle hitting the front window of the detector, the same stripper and stopper foils system as the coincidence measurement was used. The performance test of this system by using a gold target showed the influence of secondary-α created by the foils was less than 0.1% of the total yield of α-particle and that the secondary-α spectrum did not have any distinct structure.

To check the systematic error of detecting system and get data of much finer incident energy steps, the measurement using solid state detectors and a 163 μg/cm^2 carbon target was also performed at incident energies of E_{lab}=133-154 MeV in approximately 3 MeV steps. Each of two counter telescopes, set at 4° and 8° inside a 122 cm-diameter scattering chamber, consisted of four solid state detectors, such as 200 μm ΔE, 1.0 mm E and two more 1.5 mm E detectors. The gains of ΔE and three E signals were optimized independently, and the ratio of the gains was measured by injecting a same amount of charge into the input stage of the preamplifiers. The defining slits for them were 8.0 and 10.0 mm in diameter, respectively. They provided the solid angles and maximum angular acceptances of 1.26 and 0.87 msr and of ±1.15 and ±0.95°, respectively. To stop the elastically scattered ^{16}O particles, thick gold absorber foils were set just in front of the telescopes. The

thickness of them were 112.6 mg/cm^2 and 106.0 mg/cm^2, respectively. These values were measured by the energy loss of elastically scattered α-particles on a carbon target.

The energy calibration for the spectrometer measurement was determined by accumulating spectra from the elastic scattering of ^{16}O (E(^{16}O)= 145.37 MeV) by a 297 μg/cm^2 gold target at 4° under several magnetic fields and fitting those data with a quadratic function. The following sources of error in the calibration were investigated. First, the ambiguity of incident beam energies gave ±0.13% error. Second, the displacement of the focal plane counter from the correct position, where the kinematical broadening is compensated, effected less than ±0.1%. Third, the discrepancy between the measuring magnetic field and the true one caused also less than ±0.1% error. So, the total ambiguity of the calibration was estimated to be less than ±300 keV, in the case of laboratory system α-particle spectra. Indeed, the α-particle energy coming from the $^1H(^{16}O,\alpha)$ reaction agreed with the predicted value within 150 keV at most incident energies. The energy calibration for the counter telescopes were obtained by using the 79.39 MeV α elastic and inelastic scatterings on the same target used for the telescope runs at several angles. The energy loss in the gold absorber foil was taken into account based on the stopping power table [20]. In this case, the total ambiguity of calibration was estimated less than ±500 keV. For both cases, the overall energy resolution was estimated to be 500 keV for the $^{12}C(^{16}O,\alpha)$ reaction, which mainly came from the energy loss in the target.

For both cases, analog signals were digitized and processed on

line by a VAX-11/780 computer data acquisition system. The position or energy spectrum and the particle identification spectrum were calculated digitally by software. The particle identification for the spectrometer measurement was achieved by measuring the TOF (actually the time diffrence between the scintillator signal and the RF signal of the cyclotron), which gives information about an M/z value, and the M^2 value made by the formula, $M^2=\Delta E*(P_0+\text{constant})^2$. Here, M, z, ΔE and P_0 are a particle mass, an atomic charge, a sum of the signals from ΔE wires of the focal-plane counter and a calculated position value, respectively. Using this method, a clear separation between α-particle and triton was easily obtained. For the measurement of the solid state counter telescopes, the identification function, $PI=\Delta E*(E+k\Delta E+E_0)$, was used. Here, E_0 and k were constants which were adjusted to give the optimum isotope separation between α and ^{3}He.

The uncertainties in the absolute cross sections were estimated to be 20% which includes uncertainties of the charge collection, target thickness, and detector efficiency.

C. Experimental Results

The raw inclusive spectra of α-particle taken by the spectrometer at several incident energies are shown in Fig. III-1 with the logarithmic vertical scale versus the α-particle laboratory energy. These energy spectra were made by converting the position spectra considering the energy loss in the target and stripper foil. Over the full incident energy range huge continuum components are observed in the spectra. On the continuum background we can see several distinct structures especially in the low incident energy data. Those structures are

Fig. III-1. Raw inclusive α-spectra at various incident energies taken by the spectrometer. Arrows show the $E_x(^{24}Mg)$=20.2 MeV state. The solid and dashed curves are the theoretical spectra obtained by the code EVA (see text).

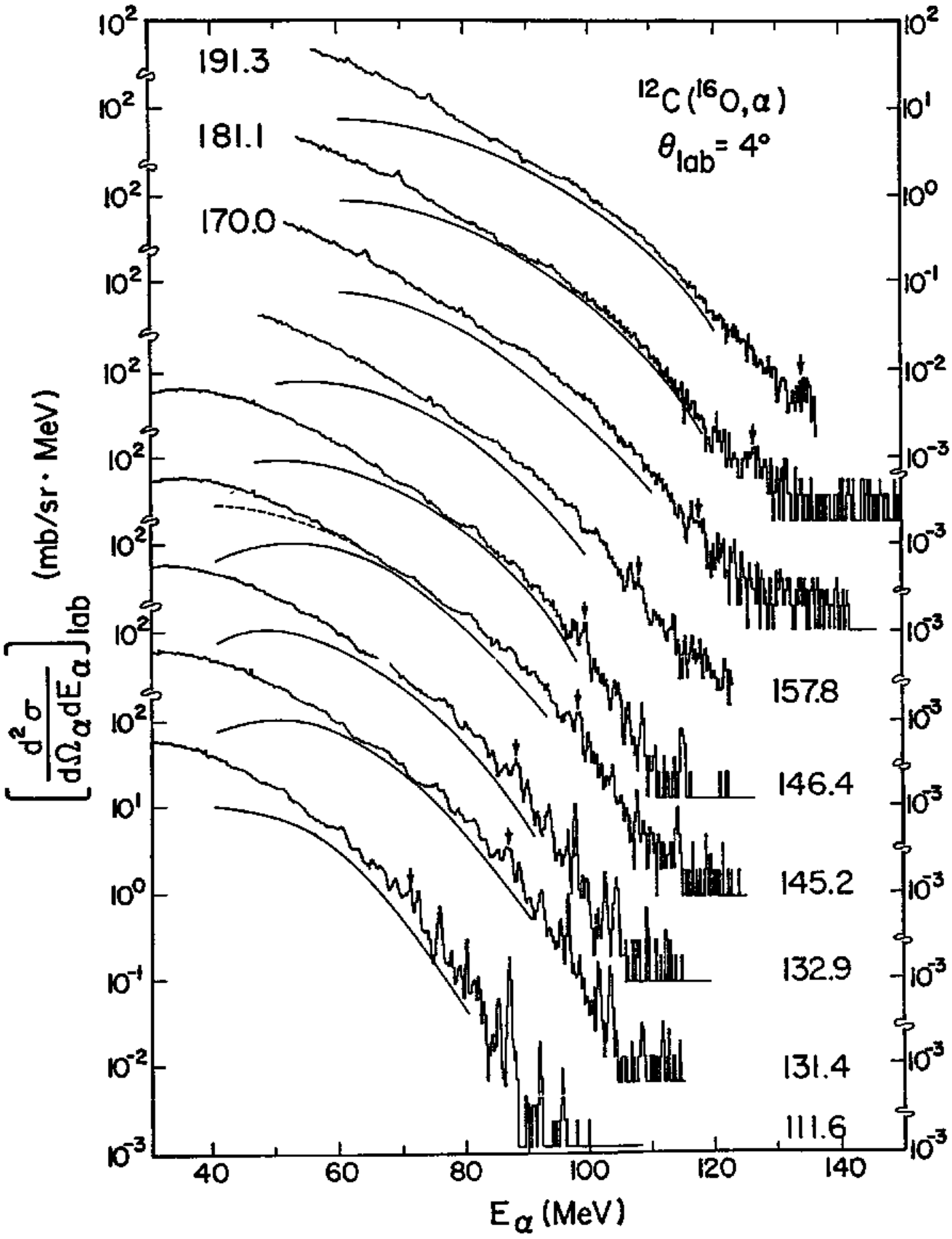
191.3
181.1
170.0
$^{12}C(^{16}O,\alpha)$
θ_{lab}= 4°
157.8
146.4
145.2
132.9
131.4
111.6
$\left[\frac{d^2\sigma}{d\Omega_\alpha dE_\alpha}\right]_{lab}$ (mb/sr · MeV)
E_α (MeV)
40
60
80
100
120
140

gradually disappearing as the incident energy becomes higher and almost vanish at 191 MeV. The similar results were obtained by the solid states counter telescopes as compared in Fig. III-2. The structures are more clearly seen in the background subtracted α-spectra in Fig. III-3(a). The method of the subtraction is same as described in ref. [5]. For convenience, the horizontal axis represents the scale of the excitation energies in the ^{24}Mg system, while the vertical axis gives the absolute double differential cross section in the labratory system with the linaer scale. The positions of the reported molecular resonances also displayed in the figure. Though our new data at 145.2 MeV shows a good agreement with the previous data [14], it is quite clear that there are no distinct structures which strongly correlate with the so-called nuclear molecular states in the region of $E_x(^{24}Mg)$= 30-56 MeV. On the other hand, the structures below E_x=30 MeV could be identified as low lying states of ^{24}Mg. The additional results of the measurements via the solid state detectors are shown in Fig. III-3(b) and III-4. Even though the junction of several solid state detectors caused spurious structures in the spectra, it is obvious that the main parts of structures on the continuum background are continuously moving when the data at different bombarding energies are plotted as a function of ^{24}Mg excitation energy. The fact that most of the structures do not follow the two-body kinematics of the $^{12}C+^{16}O\rightarrow$ $^{24}Mg^{*}+\alpha$ reaction for definite states of ^{24}Mg indicates that their origin could be a much more complicated process, such as a sequential decay. In other words, the α-particles which make up the structures may not be produced in the first direct reaction step.

Fig. III-2. Comparison of inclusive α-spectra taken by the spectrometer and the solid state counter telescope at $\theta_{lab}=4°$.

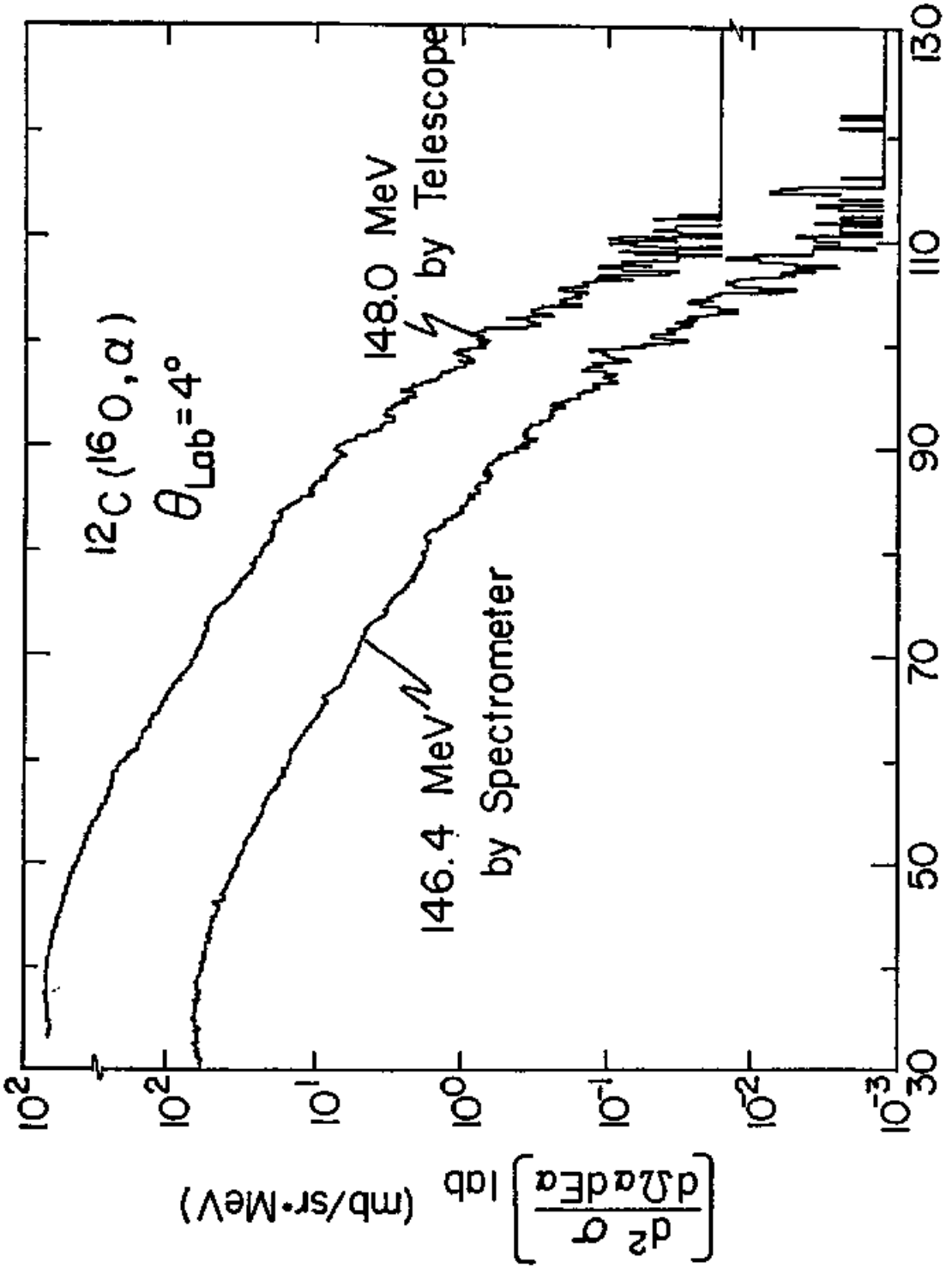
$^{12}C(^{16}O,\alpha)$
$\theta_{Lab}=4°$
148.0 MeV
by Telescope
146.4 MeV
by Spectrometer
$\left[\frac{d^2\sigma}{d\Omega_a dE_a}\right]_{lab}$ (mb/sr•MeV)
E_{lab} (MeV)
10^2
10^2
10^1
10^0
10^{-1}
10^{-2}
10^{-3}
30
50
70
90
110
130

Fig. III-3. Background subtracted α-spectra obtained by the spectrometer (a) and the solid state counter telescope at θ_{lab}=4° (b). For comparison, right-hand side figure also includes the spectra taken by the spectrometer at E_{lab}=157.8, 146.4 and 131.4 MeV. Vertical spacings of the spectra are roughly proportional to differences of incident energies shown in the figure. The positions of the molecular resonances [7] are displayed by dashed lines in the left one. Sprious structures caused by the junction of the solid state detectors are shown by hatched areas and defects of the focal plane counter by open triangles, respectively.

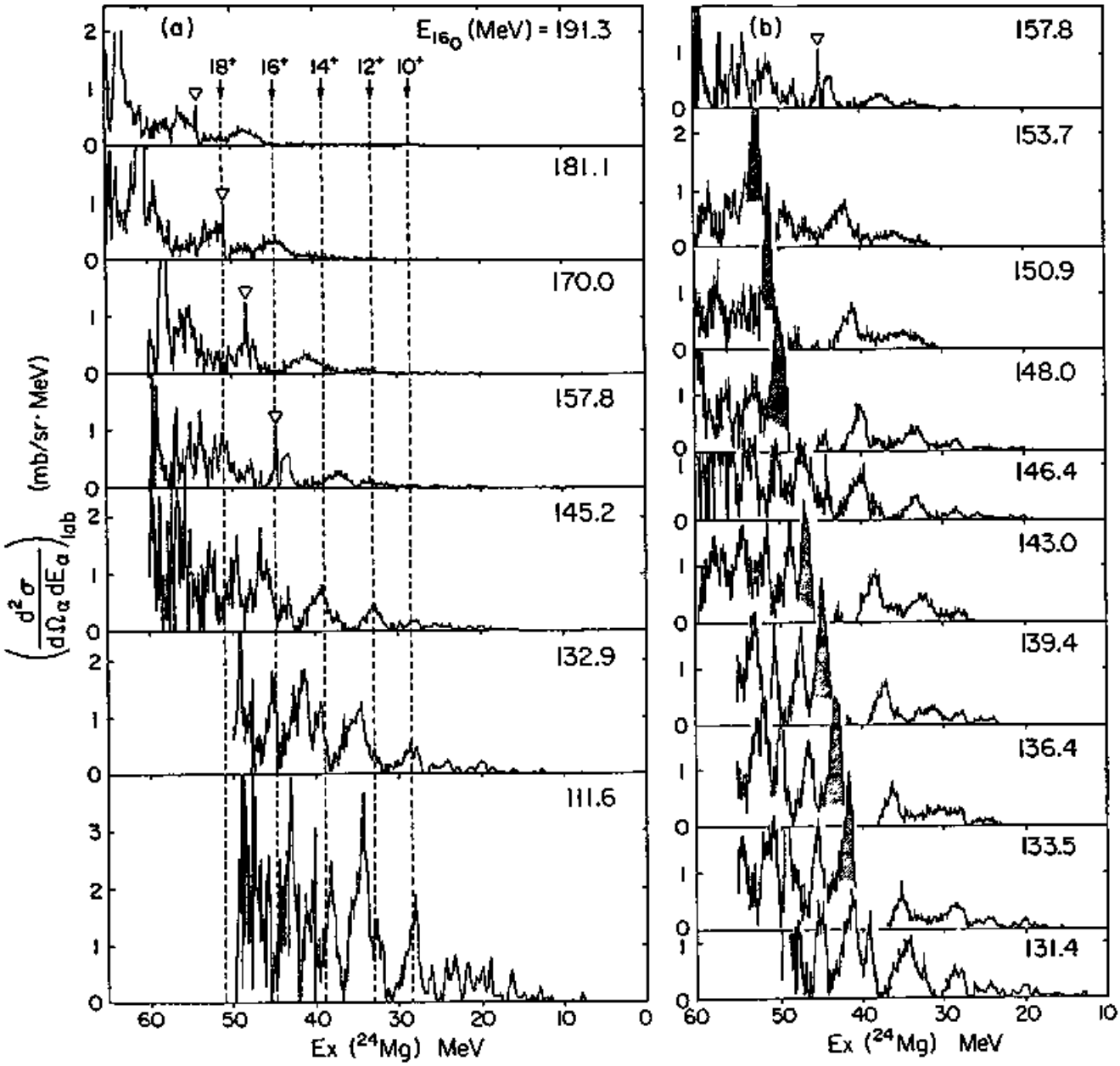
(a)
$E_{^{16}O}$ (MeV) = 191.3
18+
16+
14+
12+
10+
181.1
170.0
157.8
145.2
132.9
111.6
$\left(\frac{d^2\sigma}{d\Omega_\alpha dE_\alpha}\right)_{lab}$ (mb/sr·MeV)
Ex (^{24}Mg) MeV
(b)
157.8
153.7
150.9
148.0
146.4
143.0
139.4
136.4
133.5
131.4
Ex (^{24}Mg) MeV

Fig. III-4. Background subtracted α-spectra obtained by the solid state counter telescope at $\theta_{lab}=8°$. Again vertical scalings of the spectra are roughly proportional to differences of incident beam energies shown in the figure. Spurious structures caused by the junction of the solid state detectors are shown by hatched areas.

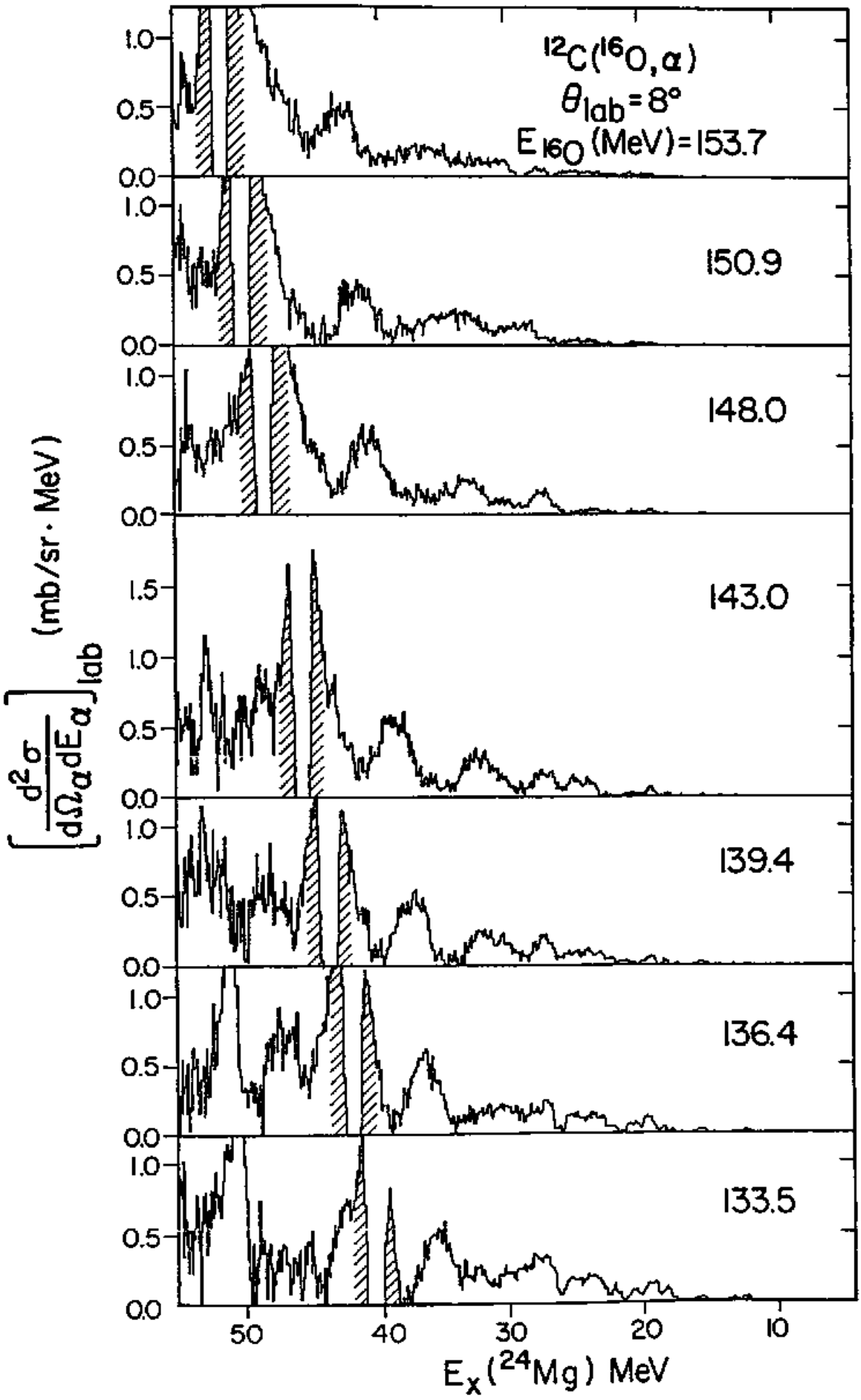
$^{12}C(^{16}O,\alpha)$
$\theta_{lab} = 8°$
$E_{^{16}O}$ (MeV) = 153.7
150.9
148.0
143.0
139.4
136.4
133.5
$\left[\frac{d^2\sigma}{d\Omega_\alpha dE_\alpha}\right]_{lab}$ (mb/sr · MeV)
$E_x(^{24}Mg)$ MeV

D. Discussion

i. Energy Dependence of Background

To understand the energy dependence of continuum parts of inclusive α-spectra, we estimated the contribusions of α-evaporation from the compound ^{28}Si nucleus. For this purpose, we developed the Monte Carlo code EVA [21] which follows a Hauser-Feshbach formalism. The calculation includes the successive evaporation of neutrons, protons and alpha particles. As well known, this type of calculation depends on the transmission coefficients and level densities. However, at the high excitation energies now considered, there is very little knowledge about the level densities of the residual nuclei. Therefore, we calculated the level density following the prescription of Puehlhofer [22] which is used in the code CASCADE. His formula is based on Lang's formula [23] in which the effective excitation energy is defined by subtracting the pairing energy and the rotational energy of a rigid rotor from the actual excitation energy. While in the Lang's formula all parameters are treated as energy-independent, Puehlhofer introduced a sort of energy and angular momentum dependent paramaters. The parameters used in EVA were quoted from the code CASCADE [22]. For the exit channel, the transmission coefficients were obtained by using a Fermi function:

$$T_l = C_a * \{1+\exp[(1-E_a/B_l)/\Delta]\}^{-1}$$

$$B_l = Z_a Z_b e^2/R_c + \{\hbar^2/(2\mu_a)\} l(l+1)/R_l^2$$

$$R_c = r_c(A_a^{1/3}+A_b^{1/3})$$

$$R_l = r_l(A_a^{1/3}+A_b^{1/3}),$$

where the subscripts a and b refer to three different evaporated

particles and the residual nucleus respectively and symbols E, Z ,A and μ denote the energy, charge, mass and reduced mass, respectively. The Δ, r_c and r_l are the phenomenological parameters whose values were adjusted to reproduce the transmission coefficients in the α-channel calculated by the optical potential of the $\alpha+^{24}Mg$ system. (Actual values are Δ=0.1 fm, r_c=1.8 fm and r_l=1.6 fm.) The normalization factors C_a were chosen to be 0.6, 0.8 and 1.0 for p-, n- and α-channel, respectively. For a spin cut-off, we calculate the moment of inertia of the residual nucleus using a parameter r_0=1.3 fm. The results of the calculation are shown in Fig. III-1. The solid curves show the results of the first evaporation step, while the dashed curve in E(^{16}O)=145.2 MeV data displays the result of all available steps together. As seen from the calculation results of 145.2 MeV case, most alpha particles in the interesting region of the spectra come from the first evaporation step. During the calculations, we adjusted the critical angular momentum values to fit the experimental data as good as possible, but no other parameters were changed. As seen, the smooth components of the experimental spectra were well reproduced by the statistical calculation in terms of both shape and magnitude except at low energy region. The obtained critical angular momentum values are shown in Table III-1 compared with theoretical ones predicted by using the statistical yrast line model [24]. They show quite good agreement over the entire energy range we measured. Considering these facts, the continuum background part might mainly come from the compound process. It should be noted that the angular dependence of the background part is also well-explained by the compound process as seen in Fig. III-5.

Fig. III-5. Angular dependence of the raw α-spectrum taken by solid state counter telescopes at E_{lab}=148 MeV. The solid curves are the first evaporation step α-spectra obtained by the code EVA with critical angular momentum 20 $\hbar$.

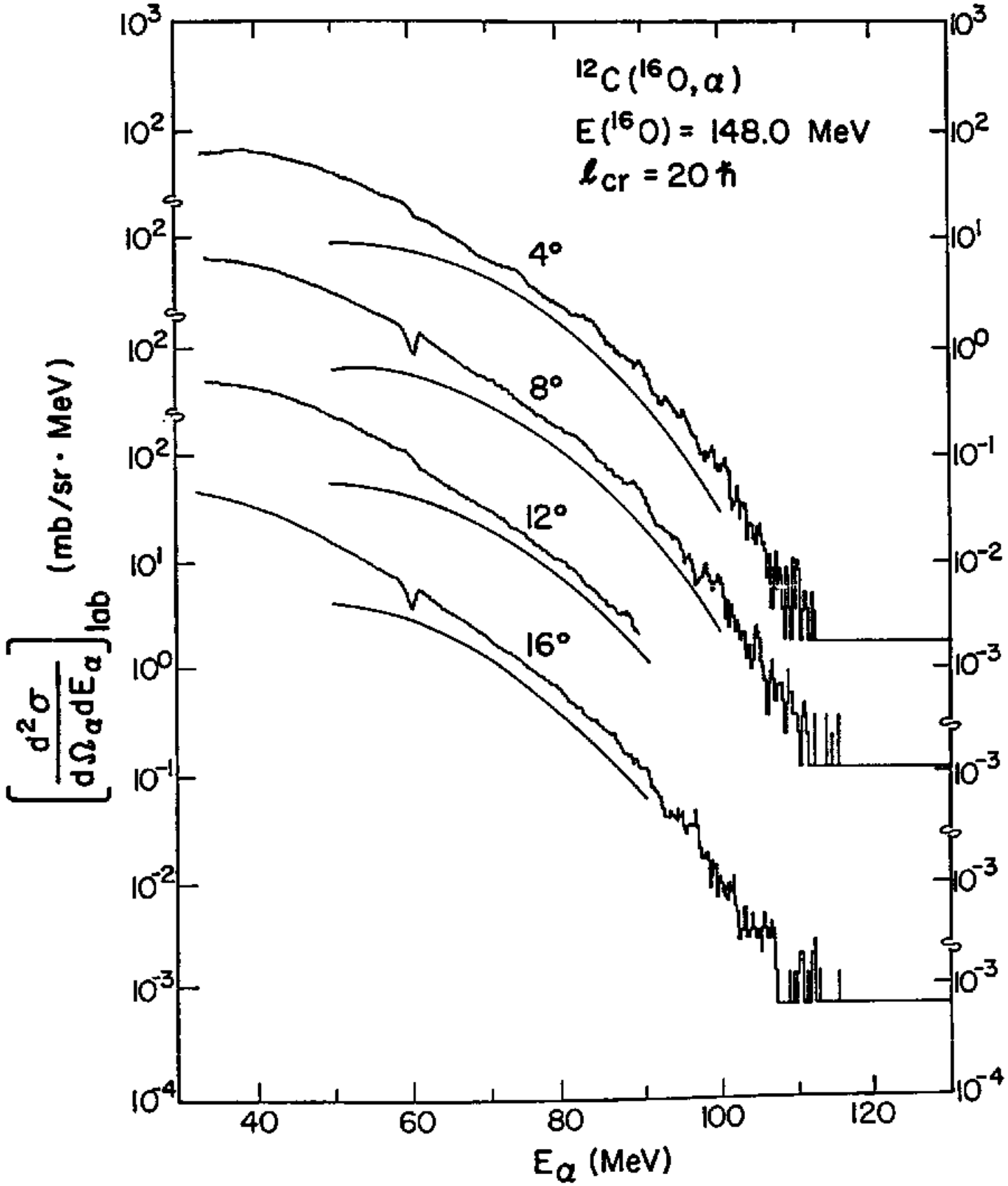
$^{12}C(^{16}O,\alpha)$
$E(^{16}O) = 148.0$ MeV
$\ell_{cr} = 20\hbar$
4°
8°
12°
16°
$\left[\frac{d^2\sigma}{d\Omega_\alpha dE_\alpha}\right]_{lab}$ (mb/sr · MeV)
E_α (MeV)
40
60
80
100
120

Table III-1.

Critical angular momentum for $^{16}O+^{12}C$ system at various incident energies.

E_{lab} (MeV)	111.6	131.4	132.9	145.2	146.4	157.8	170.0	181.1	191.3
L_{cr}(exp)	17	19	19	20	20	20	21	22	22
L_{cr}(th)	18	20	20	21	21	21	22	23	23

For the theoretical calculation we used the parameters r_0=1.15 fm and ΔQ=12.5 MeV. [24]

ii. Energy Dependence of Structures

a) Contribution of Ejectile Sequential Decay

According to the results of a recent measurement of α-H.I. coincidences from $^{12}C(^{16}O,\alpha)$ reaction at E_{lab}=142 MeV [25], α-^{12}C and α-^{16}O coincidences had a resonably large cross section. Moreover, the relative kinetic energy spectra of the α-^{12}C and α-^{16}O at different angle pairs showed several peaks which were correlated. The α-^{12}C coincidence spectra at E_{lab}=140 MeV taken by Rae et al. [11] also showed similar results. These facts strongly suggest the possibility that the sequential ejectile decay processes, $^{16}O^{*}\rightarrow{}^{12}C+\alpha$ and $^{20}Ne^{*}\rightarrow{}^{16}O+\alpha$, play an important role for the structures in the inclusive α spectrum. The ejectiles $^{16}O^{*}$ and $^{20}Ne^{*}$ could be produced by an inelastic scattering or a direct α-pickup reaction, respectively. At incident energies of approximately 10 MeV/nucleon angular distributions for inelastic scattering and direct α transfer reactions likely are strongly peaked at small center-of-mass angles. Therefore we made a simple kinematical calcultion of α-particle energies coming from the ejectile sequential decays, based on the following assumptions. First, only the ejectiles which are scattered within 5° about the beam axis in the laboratory system affect the inclusive α spectrum. Second, only the excitations of $^{16}O^{*}$ and $^{20}Ne^{*}$ which were observed in the coincidence measurements [11,25] need to be taken into account. ($E_x(^{16}O)$=10.4, 11.6, 13.1, 15.8 and 19.4 MeV [11] and $E_x(^{20}Ne)$=10.26, 11.95, 14.33, 15.34, 16.58, 20.47 and 26.7 MeV [25].) Third, the decays of the $^{16}O^{*}$ and $^{20}Ne^{*}$ are isotropic. The equations we actually used are summarized in

Appendix C. The results of the calculation are displayed in Fig. III-6, together with the positions of the observed structures. The solid and dashed lines represent mean energies of the α-particle allowed under the assumptions for $^{20}Ne^*$ and $^{16}O^*$. respectively. It should be noted that the energies do not necessarily agree with the centroid energies of the calculated structures, which strongly depend on angular distributions of the first step reactions. Keeping this in mind, both inelastic and α-pickup sequential decay processes seem to show correlations with the experimantal data.

b) Contribution of Compound Process

While most of the structures in the region of $E_x(^{24}Mg)$=30-56 MeV do not follow the two-body kinematics between the α and ^{24}Mg, those below E_x=30 MeV clearly belong to the excited states of the ^{24}Mg. A typical example of the population of the states in ^{24}Mg is shown in Fig. III-7. To make clear the peaks, the background term is subtracted in this figure. The members of $K^{\pi}=0^+_1$, 0^-, and 2^+ bands, for instance $E_x(^{24}Mg)$= 1.37(2^+), 4.12(4^+), 8.12(6^+), 13.20(8^+), 10.03(5^-), ≈12.45(7^- and 7^+), 16.55(9^-), 9.52(6^+), and 14.14(8^+) MeV, are selectively populated in the low incidet beam energy cases. However, beyond $E(^{16}O)$= 157.8 MeV those states are no more visible. In the region $E_x(^{24}Mg)$=19-30 MeV, where we could expect to see the nuclear molecular resonances, several states are stronly populated. The positions of those peaks are estimated to be $E_x(^{24}Mg)$= 19.2, 20.2, 20.8, 21.8, 23.5, 24.5, 26.1 and 28.2 (±0.2) MeV, which well correlate to the results of Lazzarini et al. [10].

Fig. III-6. Calculated energies of the structures coming from the sequential decays. Each solid or dashed line shows the mean energies of α-particles from a given excitation of the ^{20}Ne or ^{16}O, respectively. The excitation energies included are $E_x(^{20}Ne)$=10.26, 11.95, 14.33, 15.34, 16.58, 20.47, 22.87 and 26.7 MeV [25] and $E_x(^{16}O)$=10.4, 11.6, 13.1, 15.8 and 19.4 MeV [11]. (The higher excitation line appears more right-side.) The observed positions of structures are shown in the figure by squares, while open circles mean smaller structures. The observed widths of the structures are displayed by bars. Solid and dashed arrows show the kinematically allowed regions of α-particle from the ^{20}Ne* and ^{16}O*, respectively. For comparison, the locus corresponding to $E_x(^{24}Mg)$=39.0 MeV, which was claimed as 14^+ molecular state [7], is shown by a dash-dotted line.

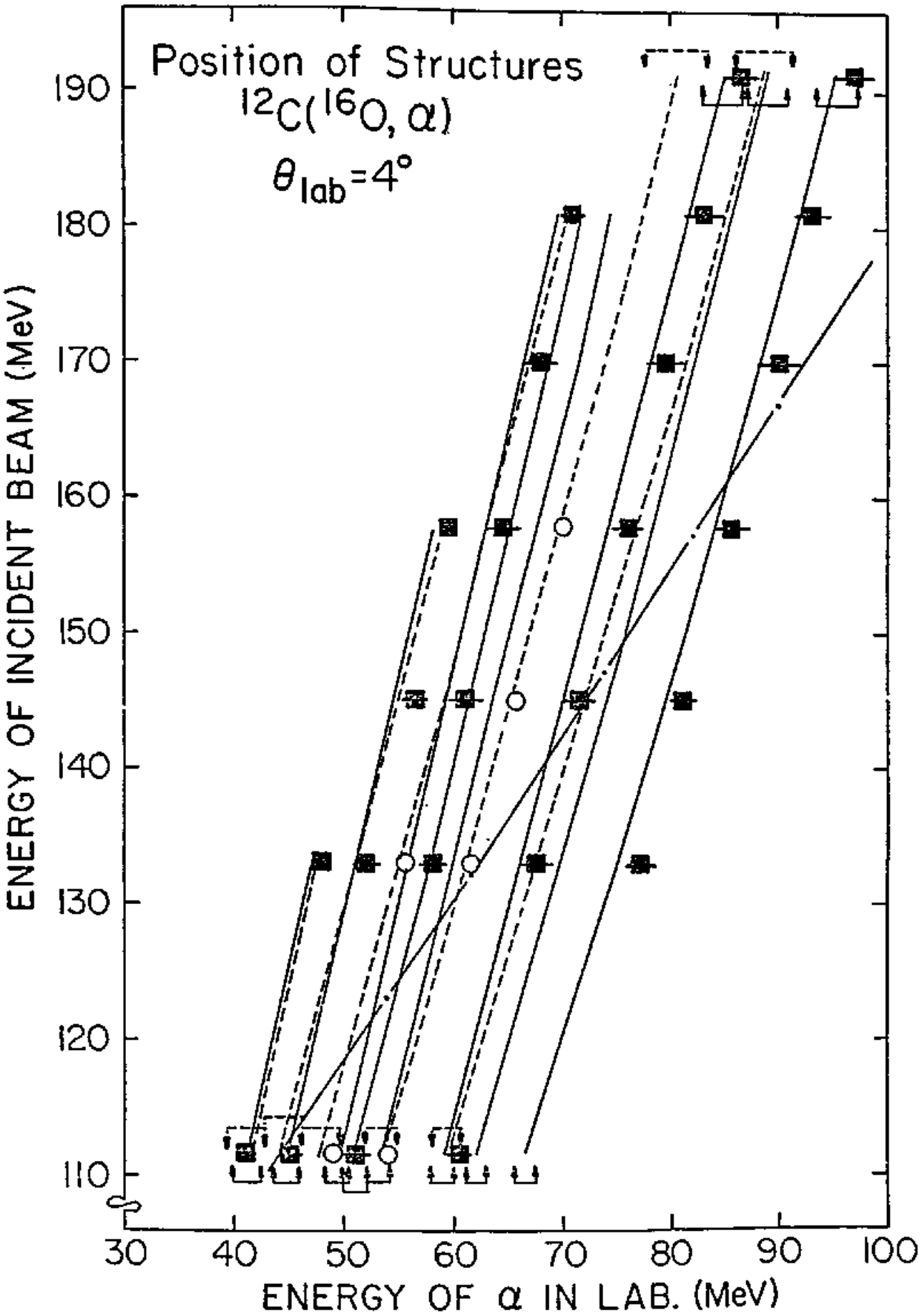
Position of Structures
$^{12}C(^{16}O, \alpha)$
$\theta_{lab}=4°$
ENERGY OF INCIDENT BEAM (MeV)
190
180
170
160
150
140
130
120
110
30
40
50
60
70
80
90
100
ENERGY OF α IN LAB. (MeV)

Fig. III-7. Typical example of the population of the states in the ^{24}Mg. For convenience, the horizontal axis represents the scale of the excitation energies in the ^{24}Mg system, while the vertical axis gives the absolute double differential cross section in the laboratory system with a linear scale.

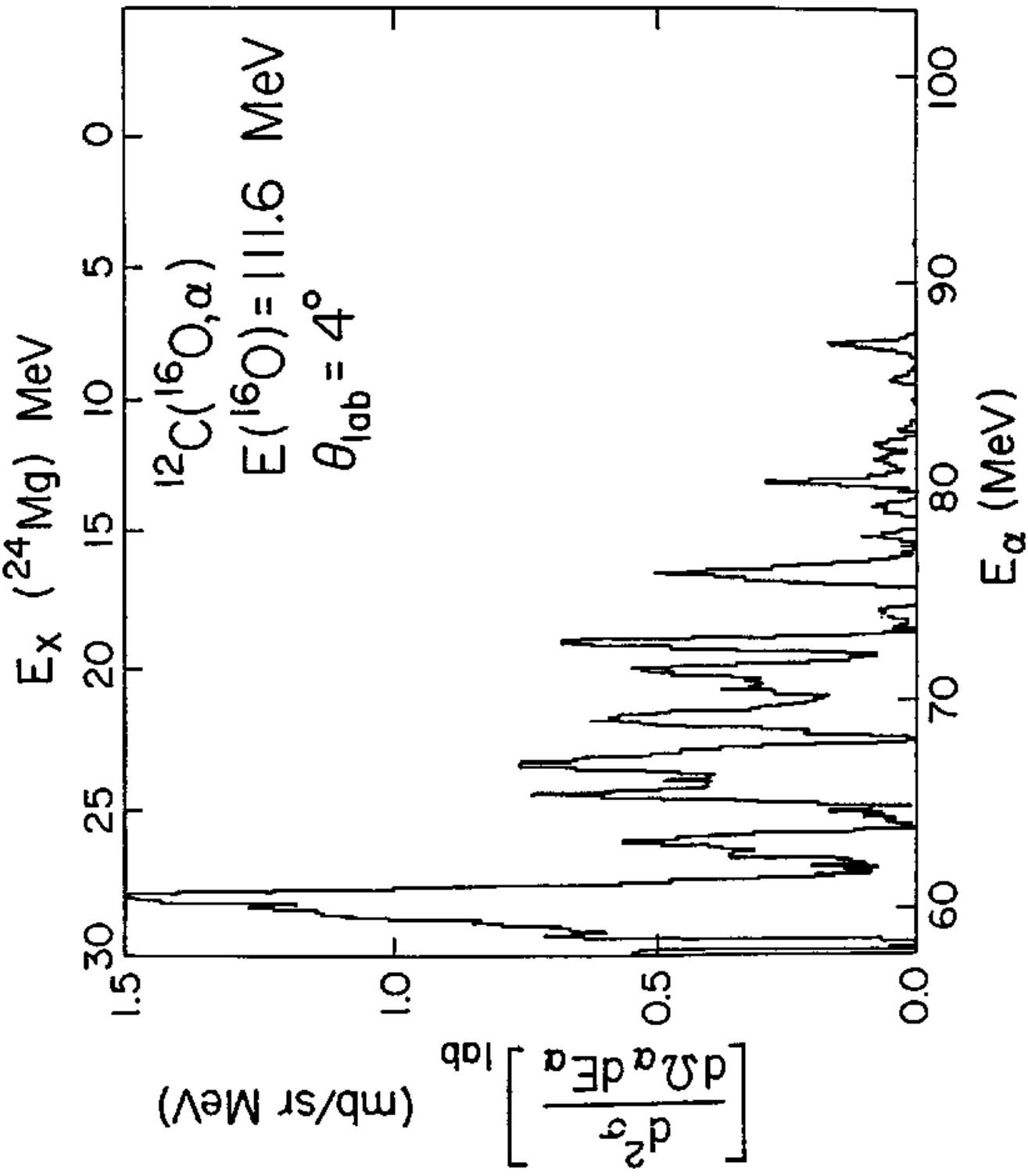
$^{12}C(^{16}O,\alpha)$
$E(^{16}O) = 111.6$ MeV
$\theta_{lab} = 4°$
E_x (^{24}Mg) MeV
E_α (MeV)
$\left[\frac{d^2\sigma}{d\Omega_\alpha dE_\alpha}\right]_{lab}$ (mb/sr MeV)
0.0
0.5
1.0
1.5
0
5
10
15
20
25
30
60
70
80
90
100

As a mechanism of the population of those states, Stwertka et al. [26] and Shimoda et al. [25] suggested the dominance of a compound nucleus formation mainly based on the angular distribution of them. In fact some structure, especially the peak around E_x=28.2 MeV, indicates that it consists of several narrower states and relative intensities among the components strongly fluctuate with the incident beam energy. On the other hand the peak around E_x=20.2 MeV seems to be a single one. (In Fig. III-1 the positions of this peak are indicated by arrows.)

To estimate the contributions of the compound process to the discrete levels, we carried out a calculation using the Hauser-Fechbach formalism. The code STATIS [27] was used for this purpose. In the present energy region, the formation of the compound nucleus is limited by the critical angular momentum rather than the grazing one. Since the values of the critical angular momenta predicted by the statistical yrast line model [24] quite well reproduce the background terms, we used those values for the calculation. Six major decay channels α, d, p, n, ^{8}Be, and ^{12}C were included in the calculation. The transmission coefficients for those exit channels were obtained by the Fermi-function, parameters of which were adjusted to reproduce the results of the optical potential calculations. (The optical potential parameters were quoted from ref. [28].) The level densities were calculated using the Lang formula [23], in which the yrast line was estimated assuming a rigid rotor. The parameters for the Lang formula were mainly taken from ref. [28]. Actual values are listed in Table III-2. Using these parameters, we can get a satisfactory fit to the angular distributions of the $^{12}C(^{16}O,\alpha)^{24}Mg$ reaction to the ground state in the incident beam

TABLE III-2.

Level-density parameters for statistical-model calculation

A_1+A_2	$^{24}Mg+\alpha$	$^{27}Al+p$	$^{27}Si+n$	$^{26}Al+d$	$^{20}Ne+^{8}Be$	$^{16}O+^{12}C$	^{28}Si
a	3.58	3.71	3.71	3.96	3.04	2.18	-
Δ(MeV)	5.13	1.8	1.8	0.0	5.13	5.13	-
E_m(MeV)	9.97	5.25	3.54	3.67	13.33	12.71	-
r_{c0}(fm)	1.42	1.25	1.50	1.45	1.63	1.47	-
E_c(MeV)	-3.42	-2.34	-0.0	-3.05	-0.37	-2.87	-
del_c	8.20	16.3	23.1	15.9	5.10	7.90	-
b	0.3	-0.1	-0.1	-0.1	0.3	0.0	-0.3

E_m; Energy above which continuum level densities were used.

level density$=(2J+1)\{12a^{1/4}(U+t)^{5/4}(2\sigma^2)^{3/2}\}^{-1}\exp\{2(aU)^{1/2}-(J+1/2)^2/2\sigma^2\}$

$U=at^2-t=E-\Delta$

$\sigma=(It/\hbar^2)^{1/2}$

$I=2/5\ mAR^2(1+0.31b+0.44b^2)$

$R=r_0A_1^{1/3}$

$r_0=1.07$ fm

$T_l(E)=[1+\exp\{(E_{Bl}-E)/(del_c*E_{Bl})\}]^{-1}$

$E_{Bl}=Z_1Z_2e^2/R_c+\hbar^2/(2\mu_cR_c^2)(l+1/2)2+E_c$

$R_c=r_{c0}(A_1^{1/3}+A_2^{1/3})$

$\mu_c=mA_1A_l/(A_1+A_2)$

(m=atomic mass unit. Z_1,Z_2,A_1,A_2 are the charges and masses of the particles in channel c.)

energy range of E(^{16}O)=28.5-100 MeV [29]. On the other hand, in the incident energy range of E(^{16}O)=112-191 MeV only very low-lying states of ^{24}Mg, such as E_x(^{24}Mg)= 1.37(2^+) and 4.12(4^+), can be explained by the calculation in terms of the absolute cross section. For most states we get approximately one order or more smaller cross section by this calculation, which shows noticable discrepancy with recent results of a similar calculation [30]. Since we used a parametrization of the transmission coefficients and there is much ambiguity in the density parameters, we cannot conclude that the compound process is unable to explain the population of highly-excited states in ^{24}Mg, especially the states in the excitation energy region of E_x(^{24}Mg)=19-30 MeV, for which we have no information of spins and parities. On the other hand, considering the results of Branford et al. [12] we cannot explain the population of the states in this region by the direct ^{12}C transfer to the nuclear molecular resonances.

In summary of this chapter, we measured the energy dependence of the ^{12}C(^{16}O,α) reaction in the range of E_{lab}=112-191 MeV. We found no experimental evidence that ^{12}C+^{12}C resonance states were observed as final states in the ^{12}C(^{16}O,α) reaction in the E_x(^{24}Mg)=30-56 MeV region where 12^+, 14^+, 16^+, and 18^+ resonances were expected. A continuous movement of the structures as a function of ^{24}Mg excitation energy was observed in this region. A simple kinematical calculation suggests that the structures in the E_x(^{24}Mg)=30-56 MeV region might come from the ^{12}C(^{16}O,α)^{16}O*(α)^{12}C and/or the ^{12}C(^{16}O,^{8}Be)^{20}Ne*(α)^{16}O reaction.

IV. $^{16}O(^{12}C,^{8}Be)^{20}Ne$ REACTION MEASUREMENT

A. Introductory Remarks

The results of the energy dependence measurement revealed that most of the prominent structures could not belong to ^{24}Mg final states. The kinematical feature of those structures were rather well described by the sequential α-decays of the ejectiles $^{16}O^*$ and $^{20}Ne^*$. In order to draw a definite conclusion about the $^{12}C(^{16}O,\alpha)$ reaction mechanism, it is essential to know differences of the inelastic scattering and alpha transfer processes, which make the ejectiles $^{16}O^*$ and $^{20}Ne^*$, between ^{12}C and ^{13}C target cases. About the inelastic scattering processes we have a little information deduced from the results of the coincidence measurements of $^{12}C(^{16}O,\alpha^{12}C)^{12}C$ and $^{13}C(^{16}O,\alpha^{12}C)^{13}C$ reactions at an ^{16}O incident energy of 140 MeV [11]. They showed less than factor of three difference in terms of the cross section, that is not enough to explain the difference between the $^{12}C(^{16}O,\alpha)$ and $^{13}C(^{16}O,\alpha)$ reactions. As for the alpha transfer process, an $^{16}O(^{13}C,^{9}Be)^{20}Ne$ reaction data at $E(^{13}C)$=105 MeV is available [31]. Therefore we decided to measure the $^{16}O(^{12}C,^{8}Be)^{20}Ne$ alpha transfer reaction at the present time.

Of course, the $^{16}O(^{12}C,^{8}Be)^{20}Ne$ reaction itself has a great interest. A ^{20}Ne nucleus is one of the most studied nucleus from both experimental and theoretical viewpoints. This is mainly due to the facts that rotational bands are well developed in ^{20}Ne nucleus and most of them are believed to have an α-clustering configuration. There are several predictions of spectoscopic factors for low-lying states, such as the shell model calculation with SU(3) classification [32], the orthogonality condition model (OCM) calculation [33] etc.. The

comparison of the observed spectroscopic factor with theoretical one might provide us an information on the reaction mechanism or the relative validity of various nuclear models. Once the reaction mechanism is known, then that reaction can be used to extract quantitative spectroscopic informations for much higher excited states.

Up to now, a variety of α-transfer reactions on ^{16}O target have been performed and the selective population of low-lying bands have been found. The lithium-induced reactions (^{6}Li,d) [34] and (7Li,t) [31,35] have been most actively investigated up to approximately 12 MeV/nucleon. This reactions have good spectroscopic overlaps for α-transfers but also have angular momentum mismatch problem due to the large change in mass. In fact most results of these reactions indicated some difficulties to extract the reliable relative spectroscopic factor $S_{\alpha}/S_{\alpha}(g.s.)$ especially in the (^{7}Li,t) reaction cases. However, recent experiment of the (^{6}Li,d) reaction at E(^{6}Li)=75 MeV [34] has shown that the experimental relative spectroscopic factors for the ^{20}Ne ground state band well agreed with theoretical predictions.

Much heavier projectiles like ^{11}B, ^{13}C, ^{14}N, and ^{16}O [31,36,37] have been also used for this kind of investigation. Considering the angular momentum matching, the reactions induced by these projectiles certainly have better situation than the lithium-induced one. On the other hand, most of them have non-zero relative orbital angular momentum between an α-cluster and a core, which necessitates the inclusion of many possible L-transfers. This complexity makes the quantitative analysis of those reactions much more difficult. Moreover, the description of most projectiles as an α-cluster and a core has no justification.

Compares with other projectile induced α-transfer reactions we mentioned above, the ($^{12}C,^{8}Be$) reaction has several advantages. Although the ground state of ^{12}C has a strong shell-model-like character, α-clustering effect is also reported to be important [38]. This fact partially supports the description of ^{12}C ground state as an α-cluster and a ^{8}Be core. The relative orbital angular momentum between the cluster and the core is zero so that the theoretical treatment should be rather simple. Furthermore, the ($^{12}C,^{8}Be$) reaction has good angular momentum matching with good spectroscopic overlap. Special experimental techniques [39] are required to detect outgoing ^{8}Be particles, because the ^{8}Be nucleus is unstable. However, this fact gives us another experimental advantage. Though efficiency of the ^{8}Be detection is not 100% due to necessity of a coincidence measurement, the detection of two coincident α-particles at the energies appropriate to a ^{8}Be ground state decay provides unambiguous particle identification and distinguishes only excitations of the residual nucleus. The results of the ($^{12}C,^{8}Be$) reactions on several targets at E(^{12}C)= 50-65 MeV showed clearly dominance of the direct reaction mechanisms except on ^{12}C and ^{16}O targets [40]. Therefore the $^{16}O(^{12}C,^{8}Be)^{20}Ne$ reaction at approximately 10MeV/nucleon is also very attractive to study highly excited states of ^{20}Ne nucleus.

B. Experimental Procedures

The measurements were performed by using a 109.4 MeV $^{12}C^{3+}$ beam extracted from the Texas A&M University 224 cm variable energy cyclotron. The energy of the beam was selected so that the $^{12}C+^{16}O$ system may get the same center-of-mass energy as in the previous

$^{12}C(^{16}O,\alpha)$ reaction at $E(^{16}O)$=145 MeV. As an ^{16}O target, self-supporting natural Al_2O_3 foil of 148 $\mu g/cm^2$ was used for the purpose of measuring ^8Be particles with good energy resolution at as forward angle as possible. The thickness of the Al_2O_3 target was determined by the energy loss method using the solid state detector with an ^{241}Am α-source. The comparison of $^{27}Al(^{12}C,^{12}C)^{27}Al$ elastic scatterings on Al and Al_2O_3-targets was also used to confirm this result. The incident energy was estimated to be 109.3 MeV at the center of the Al_2O_3 target. To estimate the background coming from a $^{27}Al(^{12}C,^8Be)$ reaction and check true peaks from a $^{16}O(^{12}C,^8Be)$ reaction, ^{27}Al target of 130 $\mu g/cm^2$ thickness and natural silica (SiO) target of 130 $\mu g/cm^2$ thickness were also used.

Since ^8Be ground state ($E_{binding}$=-92 keV) decays promptly ($\tau_{1/2} \approx 10^{-16}$ s), ^8Be particles should be measured indirectly by means of detecting their break-up two α-particles in coincidence. For this purpose, two counter telescopes each of that consisted of 200 μm ΔE and 1.5 mm E silicon surface barrier detectors were used. The thickness of the ΔE detectors were chosen so that the elasticlly scattered ^{12}C can be stopped inside of them. The usage of the ΔE detectors instead of absorber foils was dictated by the need for good energy resolution. The achieved energy resolution was estimated to be 300 keV, which was mainly due to a large angular opening. Two telescopes collimated by circular slits were set as close as posible to get a reasonably large detection efficiency. because a typical full-cone angle for $^8Be_{g.s.}$ breakup was approximately 4°. Actual separation of the telescopes was 3.44° in angle. Both of them had angular acceptance of ±0.9°. To

measure ^{8}Be particles at forward angles, they were installed perpendicular to the reaction plane.

The detection efficiency of this system was calculated as a function of ^{8}Be energy by the program, the formulation of which is summarized in Appendix B (see also ref. [41]). For the present geometry, it was calculated that the effective solid angle ranged between 0.07 and 0.08 msr for the energies of interest.

The gains of four detectors were matched by injecting a same amount of charge into the input stage of the preamplifiers. The energy calibration was roughly obtained by using the elasically scattered ^{12}C by ^{16}O and ^{27}Al, and then adjusted so that prominent known satates of ^{20}Ne* might show correct energies. The ambiguity in the absolute calibration was estimated to be less than ±100 keV.

The electronics which we used for the measurement were convetional one usually used for the particle-particle coincidence measurement. (see Fig. IV-1) Since we expected very high counting rate on ΔE detectors, the fast timing signals for a coincidence were taken from E detectors. In addition, pile-up inspectors were used for removing pile-up events on ΔE counters. The numbers of rejection by this modules were counted and taken into account for final results. Two sets of ΔE and E signals and TAC output were stored on magnetic tape event by event for the later detailed analysis and also roughly analyzed simultaneously for monitoring with a VAX-11/780 on-line computer.

A typical example of the ^{8}Be identification spectra (E_{α_1} vs. E_{α_2} and excitation energy of ^{8}Be) are shown in Fig. IV-2 and IV-3. The central, diagonal band corresponds to $^{8}Be_{g.s.}$ events. Because the

Fig. IV-1. Block-diagram of the electronics set up for the ^{8}Be detection.

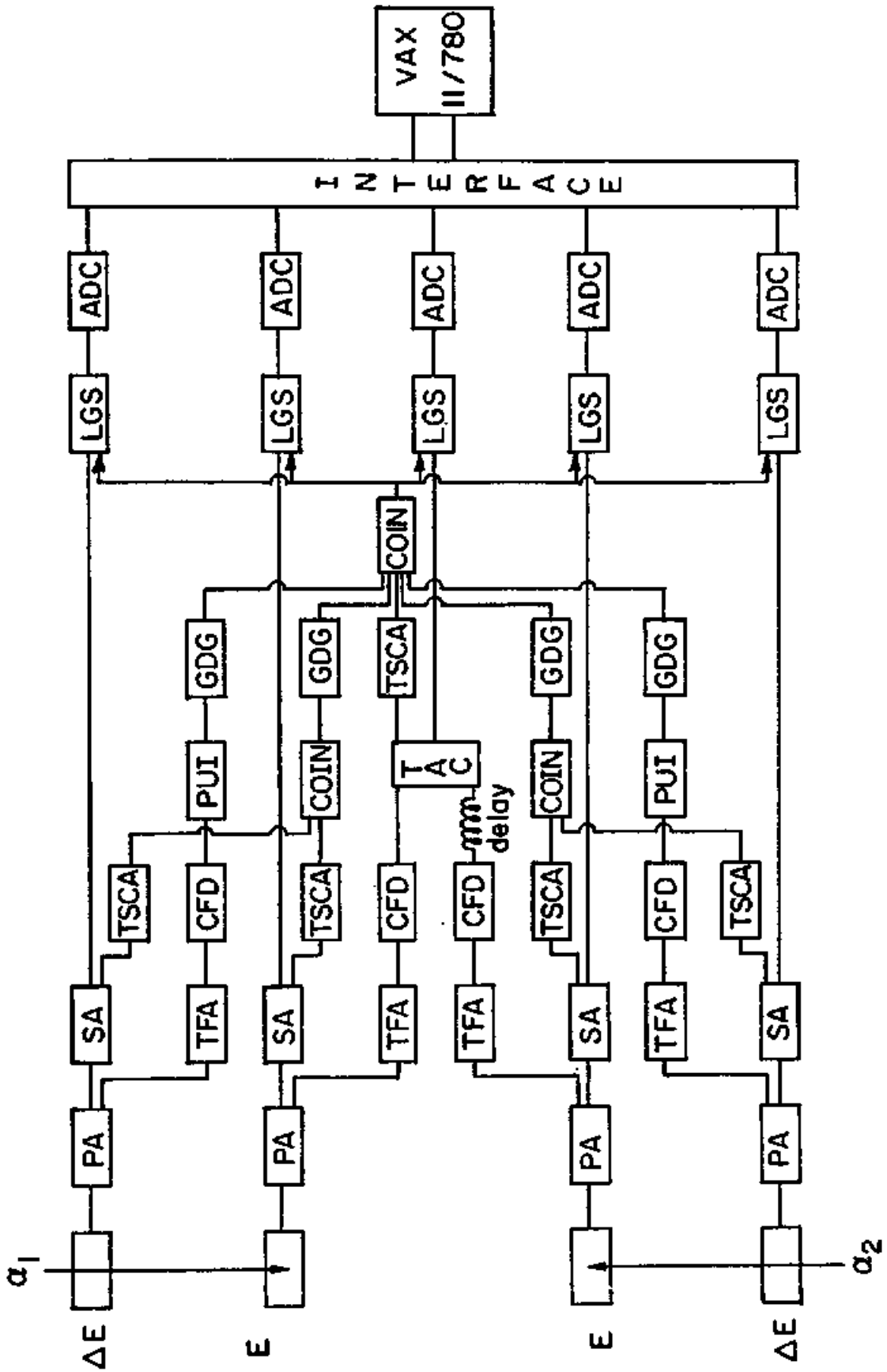
VAX 11/780
INTERFACE
ADC
LGS
COIN
GDG
PUI
TSCA
CFD
TFA
SA
PA
TAC
m delay
α_1
α_2
ΔE
E
E
ΔE

Fig. IV-2. Two-dimensional ^{8}Be identification plot. Labeled bands correspond to strongly excited states in ^{20}Ne.

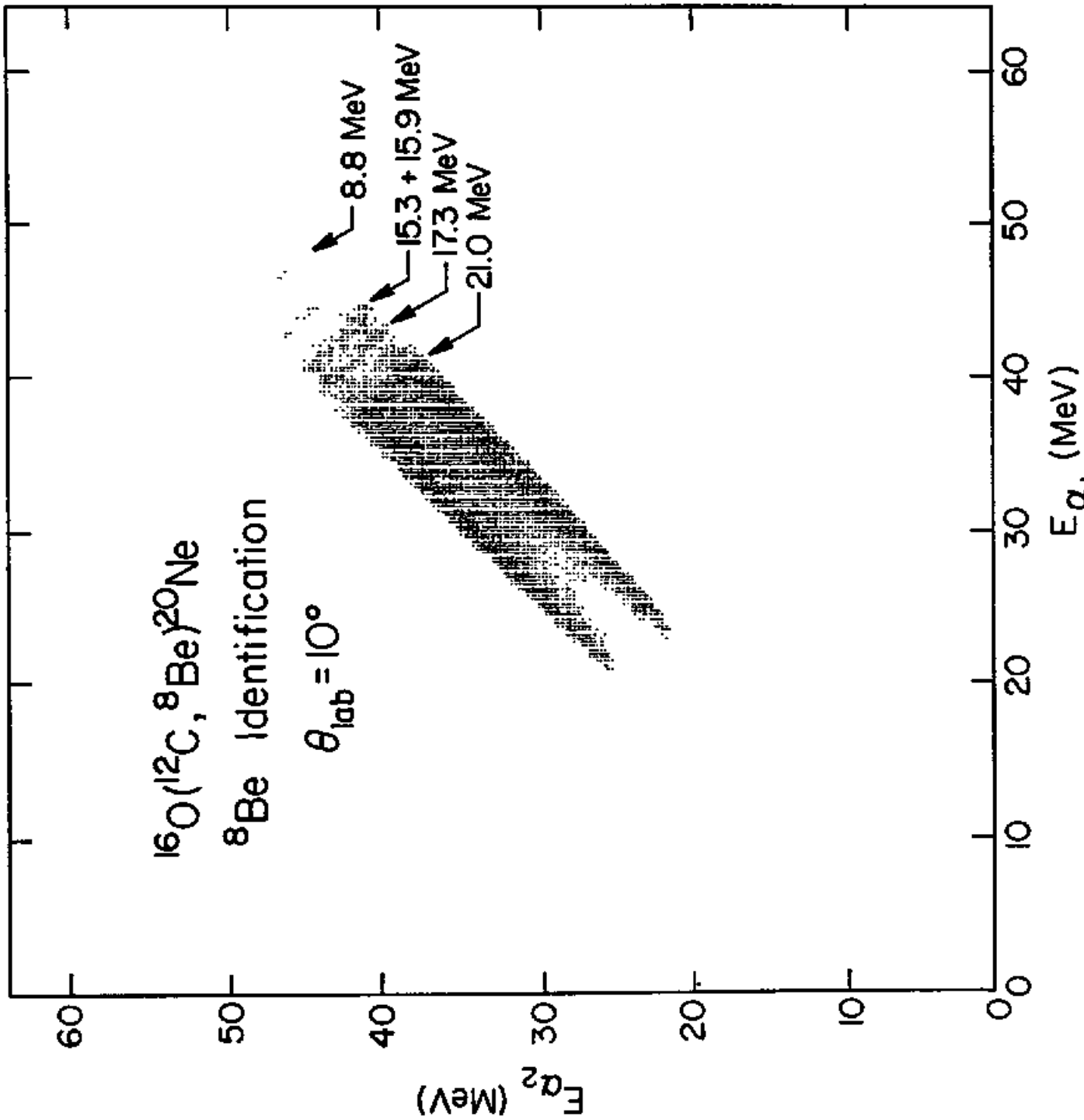
$^{16}O(^{12}C, ^{8}Be)^{20}Ne$
^{8}Be Identification
$\theta_{lab} = 10°$
8.8 MeV
15.3 + 15.9 MeV
17.3 MeV
21.0 MeV
E_{α_2} (MeV)
E_{α_1} (MeV)
0
10
20
30
40
50
60

Fig. IV-3. Typical excitation energy spectra of the ^{8}Be.

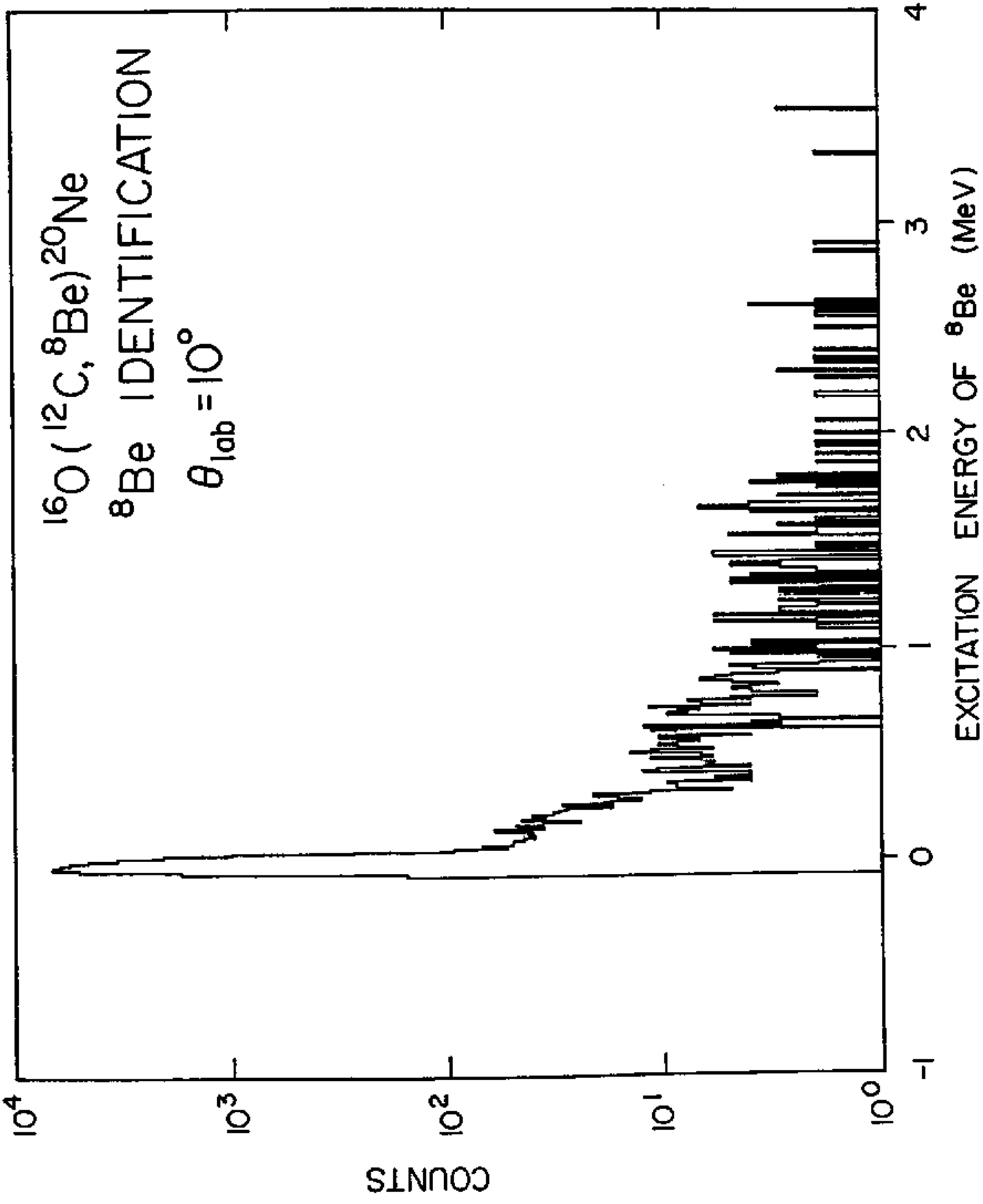
$^{16}O(^{12}C, ^{8}Be)^{20}Ne$
^{8}Be IDENTIFICATION
$\theta_{lab} = 10^{\circ}$
COUNTS
10^{4}
10^{3}
10^{2}
10^{1}
10^{0}
-1
0
1
2
3
4
EXCITATION ENERGY OF ^{8}Be (MeV)

efficiency for detecting $^{8}Be^{*}$ events in this geometry was very low, practically only $^{8}Be_{g.s.}$ events can be seen in the figure. This fact is more clearly shown by the excitation energy spectrum of ^{8}Be. To get true $^{8}Be_{g.s.}$ spectra, only those events that satisfy the time, particle identification (two alpha particles), and relative energy requirements were extracted.

As well known, in higher-energy heavy-ion reactions the angular distributions have no characteristic shape so that only information can be obtained is magnitude of the cross section. Therefore, no attempt was made to obtain spectra at more than four angles; θ_{lab}=5, 7.5, 10 and 12.8°. The uncertainties in the absolute cross sections were estimated to be less than 20% due to uncertainties in the beam collection, target thickness, estimation of the solid angle, etc..

C. Experimental Results

A typical ^{8}Be spectrum from the $^{16}O(^{12}C,^{8}Be)^{20}Ne$ reaction using the Al_2O_3 target is shown in Fig. IV-4 together with a spectrum from the $^{27}Al(^{12}C,^{8}Be)$ reaction at the same laboratory angle. For convenience, the vertical scaling is adjusted so that the same peak-height corresponds to approximately same cross section for $^{27}Al(^{12}C,^{8}Be)$ reaction between two spectra. It is clear that the $^{27}Al(^{12}C,^{8}Be)$ reaction did not show any distinct peaks but a continuum bump that might be coming from a direct breakup of ^{12}C (because the peak position of the bump corresponds to the beam velocity) in the inclusive ^{8}Be spectrum. On the other hand in $^{16}O(^{12}C,^{8}Be)^{20}Ne$ reaction case, several sharp peaks can be observed on the continuum background. The energies,

Fig. IV-4. Energy spectrum of ^{8}Be detected at $\theta_{lab}=10°$. The peaks are identified by their energies, J^{π} and K^{π} values if previously known [42]. The dashed curve indicates the detection efficiency as a function of the ^{8}Be energy and corresponds to the right-hand scale in the figure.

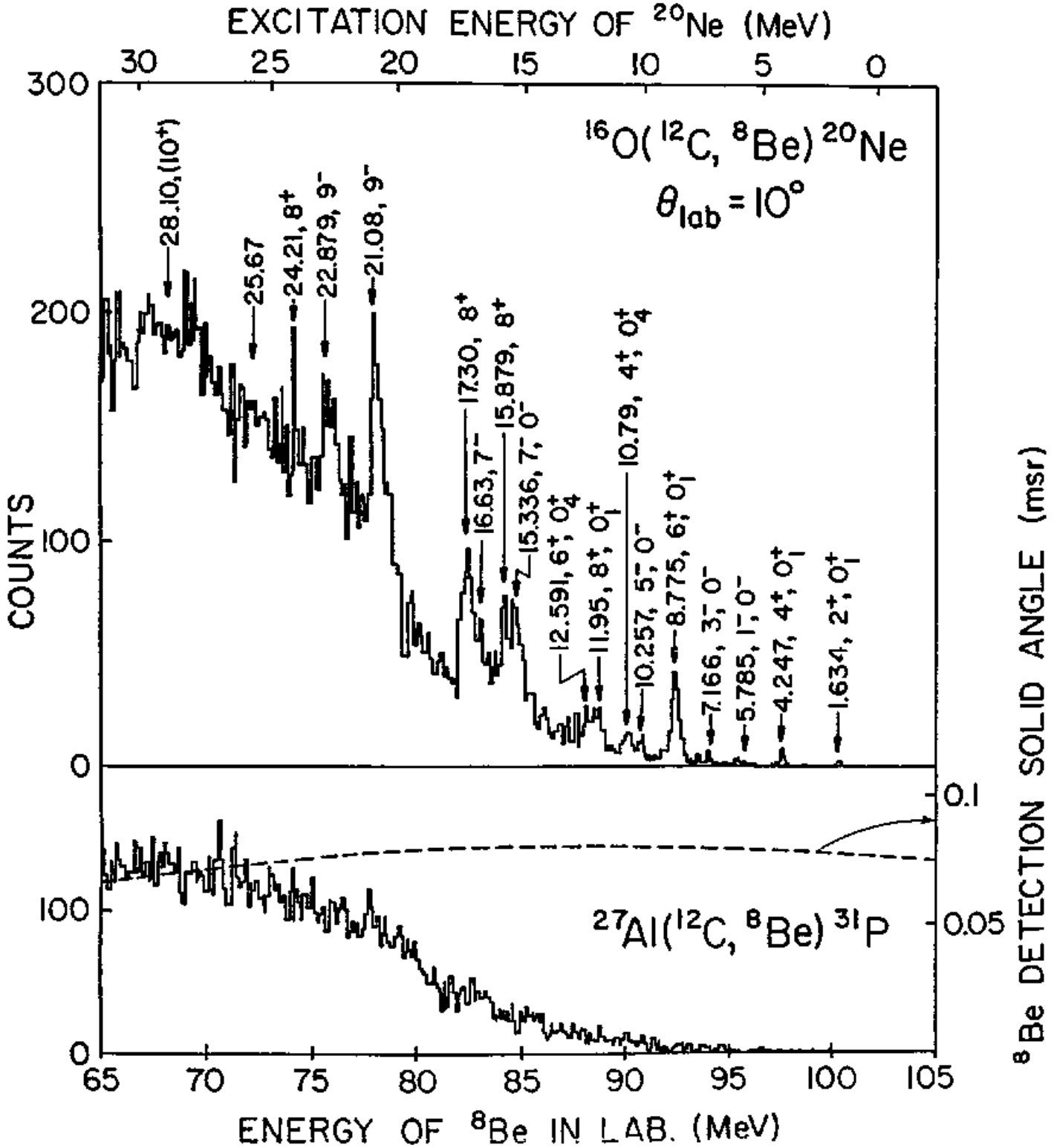
EXCITATION ENERGY OF ^{20}Ne (MeV)
30
25
20
15
10
5
0
300
200
100
0
COUNTS
^{16}O(^{12}C, ^{8}Be)^{20}Ne
θ_{lab} = 10°
28.10, (10$^+$)
25.67
24.21, 8$^+$
22.879, 9$^-$
21.08, 9$^-$
17.30, 8$^+$
16.63, 7$^-$
15.879, 8$^+$
15.336, 7$^-$; 0$^-$
12.591, 6$^+$; 0$^+_4$
11.95, 8$^+$; 0$^+_1$
10.79, 4$^+$; 0$^+_4$
10.257, 5$^-$; 0$^-$
8.775, 6$^+$; 0$^+_1$
7.166, 3$^-$; 0$^-$
5.785, 1$^-$; 0$^-$
4.247, 4$^+$; 0$^+_1$
1.634, 2$^+$; 0$^+_1$
100
0
^{27}Al(^{12}C, ^{8}Be)^{31}P
0.1
0.05
^{8}Be DETECTION SOLID ANGLE (msr)
65
70
75
80
85
90
95
100
105
ENERGY OF ^{8}Be IN LAB. (MeV)

J^{π} and K^{π} values for the states shown in the figure are taken from ref. [42]. It is worth while noting that arrows in the figure show positions of energies calculated by two-body kinematics. Compared to the (^{7}Li,t), (^{11}B,^{7}Li), (^{13}C,^{9}Be) [31], (^{14}N,^{10}B) [36], and low energy (^{12}C,^{8}Be) reaction [40] spectra, the similar, few, strongly populated states are observed. Among more than 150 known excited states of ^{20}Ne below $E_x(^{20}Ne)$=25 MeV, the (^{12}C,^{8}Be) reaction populates practically only members of the $K^{\pi}=0^{+}_{1}$, 0^{-}, and 0^{+}_{4} bands. The population of the 5^{-} state at 8.45 MeV, which has been found in the (^{6}Li,d) [34], (^{7}Li,t) [35] and (^{16}O,^{12}C) [37] reactions, was not clearly observed. Because this level is a member of $K^{\pi}=2^{-}$ band, the structure of which is a 5p-1h, this state can only be populated via the compound or multi-step process involving an 1p-1h ^{16}O core-excitation. Absence of 5^{-} state at 8.45 MeV might suggest there are few contributions coming from those processes.

The $K^{\pi}=0^{+}_{1}$ ground state band, which consists of states 1.63(2^{+}), 4.25(4^{+}), 8.78(6^{+}), and 11.95(8^{+}) MeV, has $(sd)^{4}$ configuration in the shell model and its members are well described in the SU(3) model by the $(\lambda\mu)=(80)$ representation. The α-cluster model with 2N+L=8 oscillator quanta can also describe them well. In that sense, this band is supposed to be strongly populated by a direct α-transfer reaction and it is indeed the case in the (^{12}C,^{8}Be) reaction.

The next candidate which should be populated by the α-transfer process is the $K^{\pi}=0^{-}$ band, known members of which are 5.78(1^{-}), 7.17 (3^{-}), 10.25(5^{-}), and 15.34(7^{-}) MeV states. They have mainly $(sd)^{3}(pf)^{1}$ configuration and their dominant irreducible representation of SU(3) is

the (90). In the cluster model this band is described as having 2N+L=9 quanta. It should be noted that the optimum distance between a ^{16}O-core and an α-cluster was found to be naer the contact distance of the core and cluster for the $K^{\pi}=0^{-}$ band, while quite smaller than that for the $K^{\pi}=0^{+}_{1}$ band. The population of this band is surprisingly large in the (^{12}C,^{8}Be) reaction compared to the other reactions.

The 9^{-} member of the $K^{\pi}=0^{-}$ band has not been firmly established. We found three possible 9^{-} states in our ^{8}Be energy spectra. They locate at 20.7±0.1, 21.1±0.1 and 22.9±0.1 MeV, which strongly correlate to those found in elastic α-scattering on ^{16}O. The 20.7 MeV one is a very small peak, but surely exists on the shoulder of the 21.1 MeV peak at all the angles where we performed the experiments. The 20.7 and 21.1 MeV doublet were also observed in the $^{16}O(^{14}N,^{10}B)^{20}Ne$ [36], $^{16}O(^{11}B,^{7}Li)^{20}Ne$ [31], and $^{16}O(^{13}C,^{9}Be)^{20}Ne$ [31] reactions. There is some doubt that the 22.9 MeV peak consists of only one component, because the width is too broad compared to other peaks. However, the Yale group [43] clearly identified a 9^{-} state at 22.87±0.04 MeV using the $^{16}O(^{12}C,^{8}Be)^{20}Ne^{*}(\alpha)^{16}O$ reaction at $E(^{12}C)$=78 MeV, so we believe the observed peak mainly consist of 9^{-} component at this point. They proposed the 22.87 MeV state as the 9^{-} member of the $K^{\pi}=0^{-}$ band, based on its energy and α-width. On the other hand, Bradlow et al. [31] assigned the 21.0 MeV state as the 9^{-} member of the $K^{\pi}=0^{-}$ band based on the DWBA analysis of the $^{16}O(^{13}C,^{9}Be)^{20}Ne$ reaction. From qualitative judgements, we cannot distinguish those two possibilities.

The $K^{\pi}=0^{+}_{4}$ band is supposed to have a $(pf)^{4}$ configuration with the SU(3) (12,0) representation. This assignment is based on the failure to

observe the 10.79 (4^+) and 12.591 (6^+) MeV states of this band in the $^{18}O(^{11}B,^{9}Li)^{20}Ne$ reaction [44]. The α-cluster model with 2N+L=12 quanta might well describe this band. A peak is seen at around 10.8 MeV in the present spectra, especially at 10°. However, we failed to get the angular distribution of this state, because the peak seemed to consist of several states with similar spins. On the other hand the 12.591 MeV peak was observed claerly at all angles we measured. The 8^+ member of this band has not identified yet. The candidates for 8^+ state are 15.879 and 17.3 MeV ones. Unfortunately, both of them were so strongly populated that we could not tell which one was the true member from a qualitative viewpoint.

For a reference, we show a few excitation energies of much highly excited states, such as 24.21, 25.67 and 28.1 MeV states, observed in the elastic α-scattering on ^{16}O [45] and the $^{16}O(^{6}Li,d)^{20}Ne$ reaction [34] in Fig. IV-4. There are some traces of peaks, but we could not confirm the existence of them from our data.

Angular distributions of the $^{16}O(^{12}C,^{8}Be)^{20}Ne$ reaction to the several distinct excited states in ^{20}Ne were measured. The results are summarized in Figs. IV-5~7. Curves in the figures represent the results of the EFR-DWBA calculations, which will be discussed in the next section. Most of them show a strong decrease of the cross section with an angle, that seems to be characteristic of a direct transfer process. The decreasing of the cross section becomes gradually weaker as the spin of the residual ^{20}Ne becomes larger.

Figs. IV-5~7. The $^{16}O(^{12}C,^{8}Be)^{20}Ne$ angular distributions for states in the ground state band (Fig. IV-5), $K^{\pi}=0^{-}$ band (Fig. IV-6) and $K^{\pi}=0^{+}_{4}$ band (Fig. IV-7). ($E_{x}(^{20}Ne)=22.87$ MeV is exception.) The solid curves are the results of the EFR-DWBA calculations.

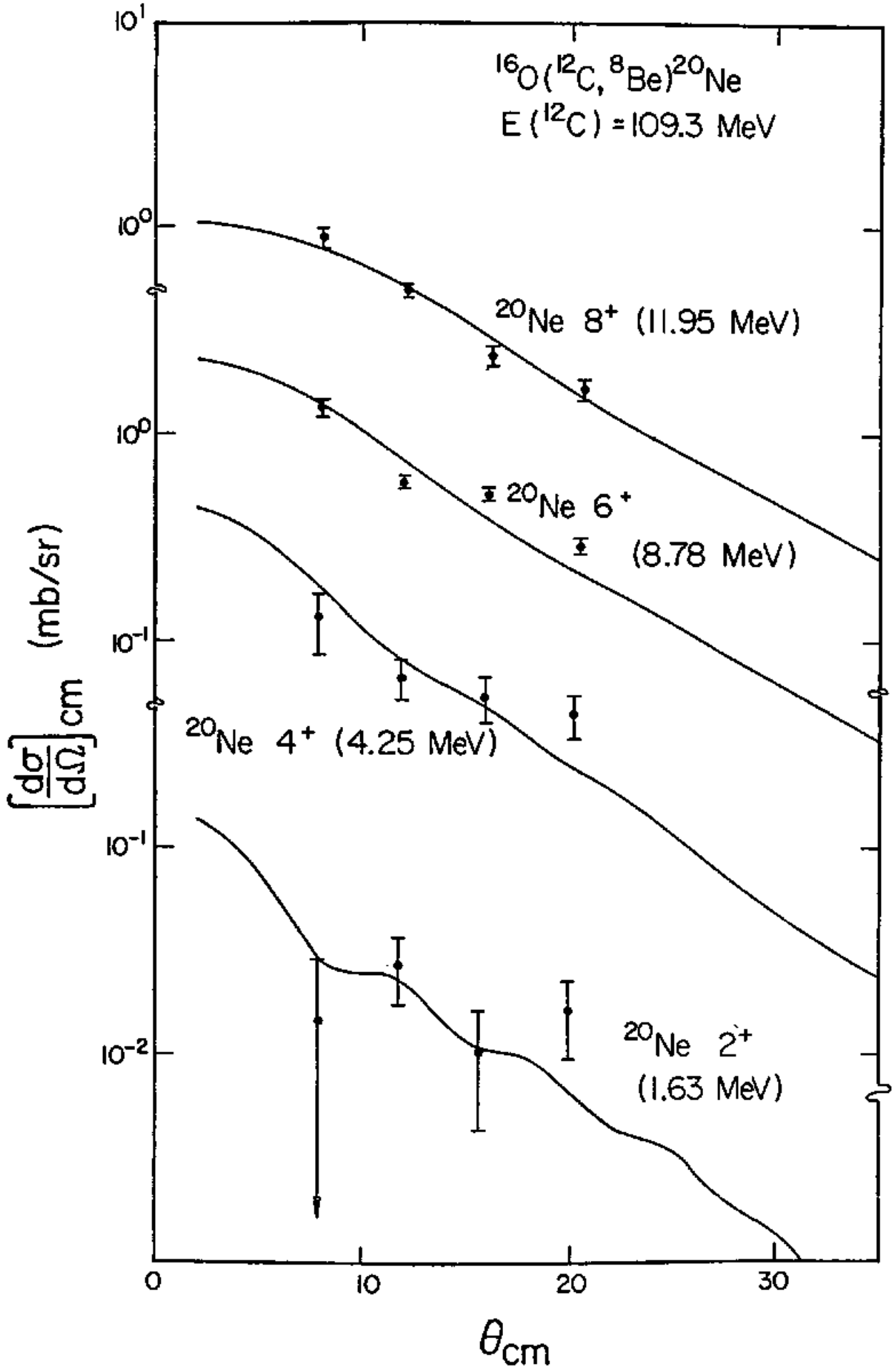
$^{16}O(^{12}C, ^{8}Be)^{20}Ne$
E(^{12}C) = 109.3 MeV
^{20}Ne 8$^+$ (11.95 MeV)
^{20}Ne 6$^+$
(8.78 MeV)
^{20}Ne 4$^+$ (4.25 MeV)
^{20}Ne 2$^+$
(1.63 MeV)
$\left[\frac{d\sigma}{d\Omega}\right]_{cm}$ (mb/sr)
θ_{cm}
10^1
10^0
10^0
10^{-1}
10^{-1}
10^{-2}
0
10
20
30

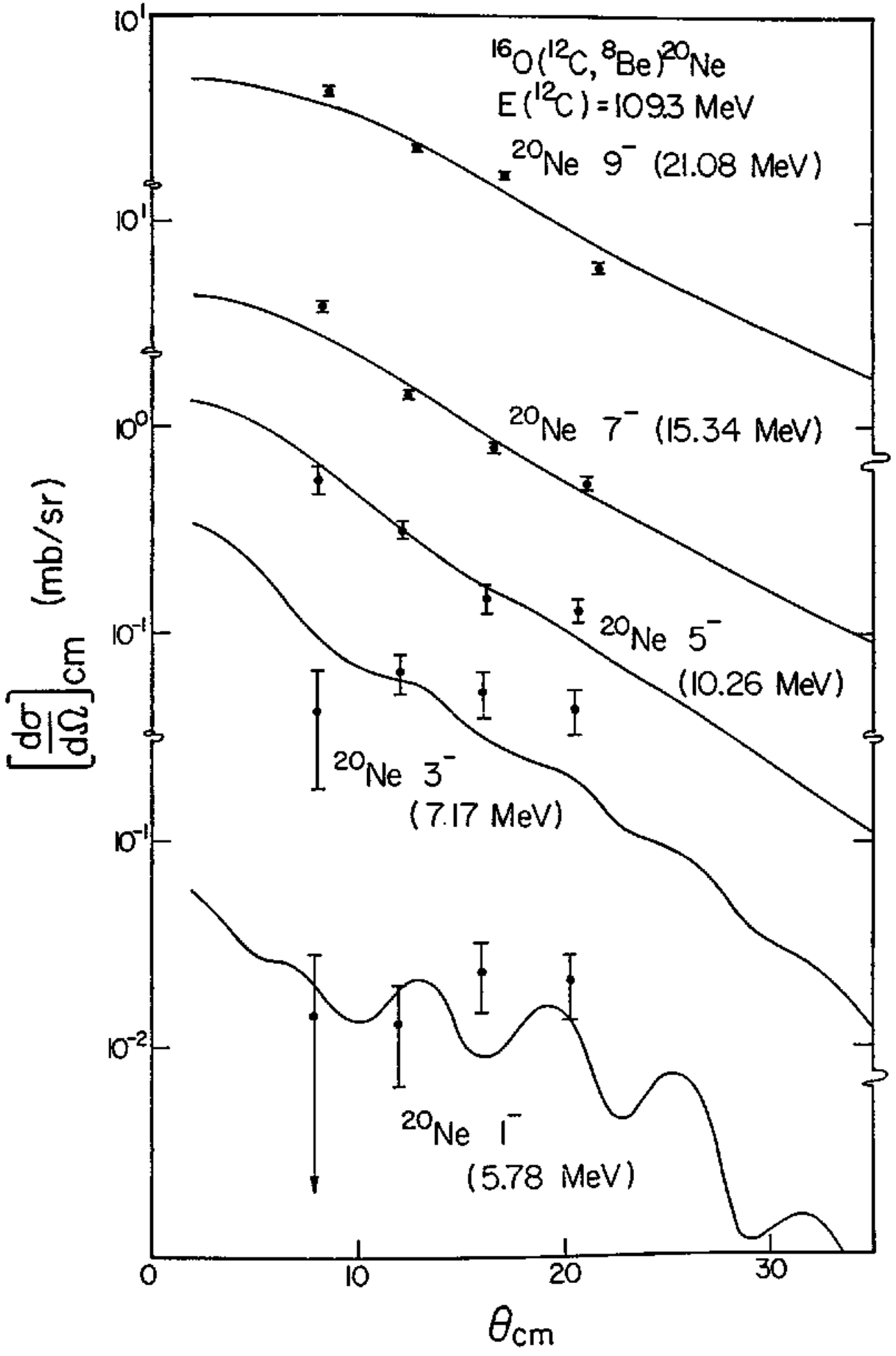
$^{16}O(^{12}C, ^{8}Be)^{20}Ne$
E(^{12}C) = 109.3 MeV
^{20}Ne 9$^-$ (21.08 MeV)
^{20}Ne 7$^-$ (15.34 MeV)
^{20}Ne 5$^-$ (10.26 MeV)
^{20}Ne 3$^-$ (7.17 MeV)
^{20}Ne 1$^-$ (5.78 MeV)
$\left[\frac{d\sigma}{d\Omega}\right]_{cm}$ (mb/sr)
θ_{cm}
10^1
10^0
10^{-1}
10^{-2}
0
10
20
30

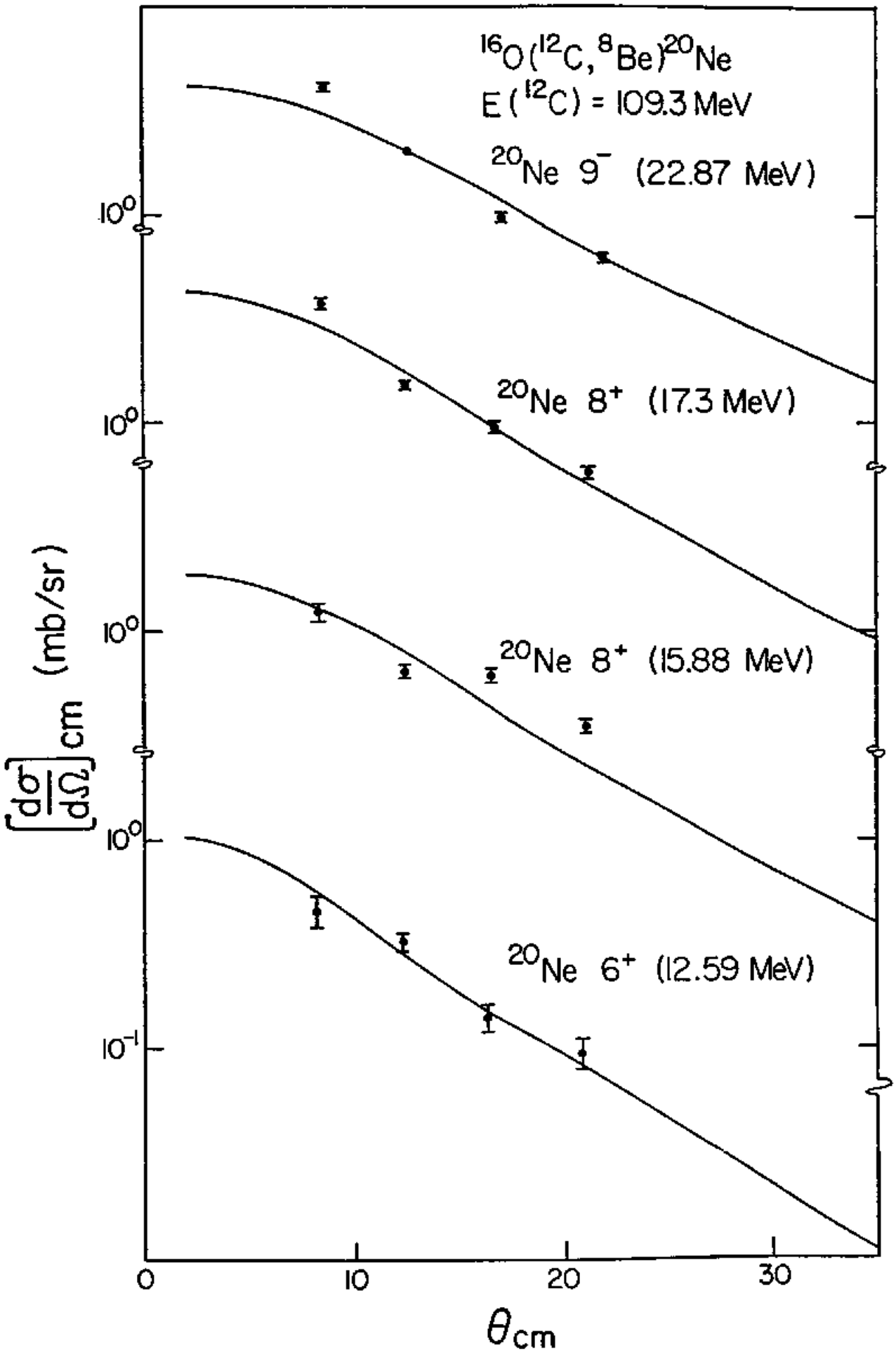
$^{16}O(^{12}C, ^{8}Be)^{20}Ne$
$E(^{12}C) = 109.3$ MeV
^{20}Ne 9^- (22.87 MeV)
^{20}Ne 8^+ (17.3 MeV)
^{20}Ne 8^+ (15.88 MeV)
^{20}Ne 6^+ (12.59 MeV)
10^0
10^0
10^0
10^0
10^{-1}
$\left[\frac{d\sigma}{d\Omega}\right]_{cm}$ (mb/sr)
0
10
20
30
θ_{cm}

D. Discussion

i. DWBA analysis

The heavy-ion induced transfer reactions at approximately 10 MeV/nucleon are generally believed to be direct reactions. On the other hand the same $^{16}O(^{12}C,^{8}Be)^{20}Ne$ reaction at a bombarding energy of 56 MeV indicated the presence of a compound or multi-step direct process. Therefore contributions of the process via the compound nucleus formation were estimated with the Hauser-Feshbach formalism. The program STATIS [27] was used for the calculation. The value of the critical angular momentum was estimated to be ~21 $\hbar$ by using the statistical yrast line model [24]. Six major decay channels α, d, p, n, ^{8}Be, and ^{12}C were included in the calculation. The transmission coefficients for those exit channels were obtained by the Fermi-function, which we used for the analysis of the energy dependence measurements of the $^{12}C(^{16}O,\alpha)$ reactions. The level density parameters were also same ones that we used. (see table III-1) The results for the observed states in ^{20}Ne are of the order of 10-100 nb/sr, at least two orders of magnitude smaller than the experimental results in Fig. IV-4. Thus the compound process may be negligible.

Following this, we assumed that the $^{16}O(^{12}C,^{8}Be)^{20}Ne$ reaction proceeds through a one-step α-cluster transfer process. The angular distributions were analyzed with the revised version of the EFR-DWBA code SATURN-MARS developed by Tamura and Low [46,47]. Because the α-transfer reaction has a stronger non-locality than the one-nucleon transfer reaction, minor modification was made. The post form was used consistently in present analysis. Though DeVries reported that in a

multinucleon transfer reaction A(a,b)B (B=A+x, a=b+x) it is necessary to include the Coulomb parts of V_{bx}, V_{bA}, and U_{bB}^{opt} interaction terms even in post form [48], no attempt was made to include them at this time. Therefore we expect that the results of analysis have approximately 30% ambiguity from this effects. As usual, the experimental differential cross section $(d\sigma/d\Omega)_{exp}$ is assumed to be related to the theoretical one $(d\sigma/d\Omega)_{DWBA}$ calculated by DWBA code as follows:

$$(d\sigma/d\Omega)_{exp}=S_1S_2(d\sigma/d\Omega)_{DWBA}.$$

Here, S_1 and S_2 denote the α-spectroscopic factors for the projectile and residual nucleus, respectively.

Most of states observed lie above the α-threshold energy of ^{20}Ne and thus the corresponding $\alpha-^{16}O$ systems are in the continuum. To analyze those unbound states which have rather broad widths, the usage of slightly bound state approximation, replacing the wave function of the continuum state by that of a bound sate, has no justification. Bradlow et al. [31] suggested that the usage of Gamow states to obtain form factors could be important for calculating absolute cross sections to unbound states. However, according to their results, in most cases the difference between cross sections obtained by using Gamow and slightly bound state wave functions was not more than factor of two. Therefore at this time we use the slightly bound state approximation to get the α-wave function in the ^{20}Ne. In the following, we consistently use the binding energy of 0.1 MeV for the unbound states, while using the experimental Q-value of the reaction. Radial wave functions of the $\alpha-^{8}Be$ and $\alpha-^{16}O$ systems were calculated using the Woods-Saxon potential

with the parameters $R=1.2A^{1/3}$ fm, where A is the mass of the core nucleus, and a=0.65 fm. For the Coulomb potential, we used the same radius as one of the Woods-Saxon potential. Using these values we can obtain the α-cluster wave functions in ^{20}Ne nucleus which are quite resemble to those made by Buck et al. [49]. The potential depth was adjusted to reproduce the binding energy of α-cluster in the α-core system (see Table IV-1). The number of nodes N of the radial wave functions was determined by the harmonic oscillator energy conservation relation formula:

$$2N + L = \sum_i (2n_i + l_i),$$

where L is the angular momentum of the α-cluster in the projectile or final state and n_i and l_i are the number of nodes and orbital angular momentum of the four nucleons with respect to the core. The actual values of N and L were determined based on the configuration we discussed in the previous section and are listed in Table IV-1.

The optical potential parameters for making distorted wave are usually chosen by fitting the elastic scattering for the channel of interest. But this procedure makes a lot of ambiguity in the parameters obtained, because all potentials which have the same shape in the nuclear surface region give similar results of forward angle cross section. Since there are well examined potential parameters used for the analysis of the ^{16}O(^{13}C,^{9}Be)^{20}Ne reaction at E(^{13}C)=105 MeV [31], we used those parameters. The actual values are listed in Table IV-2.

Table IV-1.

The well depth for states in ^{20}Ne

E_x (MeV)	J^π	N	2N+L	V_0 (MeV)	$E_{binding}$ (MeV)
1.634	2^+	3	8	136.647	-3.097
4.247	4^+	2	8	133.020	-0.484
8.775	6^+	1	8	136.327	
11.95	8^+	0	8	140.021	
5.785	1^-	4	9	151.297	
7.166	3^-	3	9	154.368	
10.257	5^-	2	9	159.534	
15.336	7^-	1	9	163.843	
21.08	9^-	0	9	168.152	
22.78	9^-	0	9	168.152	
12.591	6^+	3	12	257.468	
15.879	8^+	2	12	264.332	
17.30	8^+	2	12	264.332	

The well depth for ground states in ^{12}C and ^{13}C

	J^π	N	2N+L	V_0 (MeV)	$E_{binding}$ (MeV)
^{12}C	0^+	2	4	96.904	-7.367
^{13}C	$1/2^-$	1	4	98.344	-10.648

Table IV-2.

Optical-model parameters used in the DWBA analysis

Channel	V (MeV)	r_R (fm)	a_R (fm)	W (MeV)	r_I (fm)	a_I (fm)	r_C (fm)
$^{12}C+^{16}O$ $^{13}C+^{16}O$	65.5	1.02	0.731	45.0	1.035	0.600	1.25
$^{8}Be+^{20}Ne$ $^{9}Be+^{20}Ne$	190.0	-1.30	0.720	45.0	-1.300	1.200	-1.30

The form factor is a Woods-Saxon type one.
$R=r_0(A_1^{1/3}+A_2^{1/3})$, unless r_0 is indicated as negative in which case $R=|r_0|A^{1/3}$

ii. Results of the DWBA calculations

The results of the DWBA calculations are compared with the experimental angular distributions in Figs. IV-5~7. The theoretical curves have been normalized to the experimental data. The effect of the finite angular opening of the detection system is not taken into account in the calculation. General tendency of the angular distributions is fairly well reproduced by the calculations. Values of the spectroscopic factor S_2 for each state was calculated from the normalization factor S_1S_2 assuming S_1=0.5567 which was predicted by Kurath [50]. The obtained values are summarized in Table IV-3 together with the theoretical values. As seen in this table, the experimental spectroscopic factors show more or less reasonable values except for 8^+ and 9^- states. Possible interpretations for the discrepancy at the high spin states might be as follows. Though the α-cluster wave functions in the ^{20}Ne nucleus obtained by the Woods-Saxon potential are resemble to those made by Buck et al. [49], there are still noticeable differences between them especially in the case of the high-spin members of the $K^\pi=0^-$ band. This may cause large disagreement of the experimental spectroscopic factors with the theoretical ones in the case of high-spin states. Moreover different choices of optical potentials for both the incident and the exit channels lead to vastly different absolute spectroscopic factors. Though the relative spectroscopic factors within the $K^\pi=0^+_1$ band seem independent of the choices of optical potentials, those within the $K^\pi=0^-$ band show somewhat differences. Considering this ambiguity, it is impossible to extract physically meaningful information from our data at this time.

Table IV-3.

α-spectroscopic factor in ^{20}Ne

E_x(MeV)	J^π	(^{12}C, ^{8}Be) 109MeV [present]	(^{12}C, ^{8}Be) 56MeV [40]	(^{13}C, ^{9}Be) 105MeV [present]	OCM [33]	SU(3) [32]
1.634	2^+	0.44	0.181	0.31	0.295	0.229
4.247	4^+	0.18	0.075	0.50	0.280	0.229
8.775	6^+	0.69	-	0.75	0.264	0.229
11.95	8^+	1.59	-	0.97	0.236	0.229
5.785	1^-	1.46	-	-	0.718	0.334
7.166	3^-	0.36	-	-	0.703	0.334
10.257	5^-	0.27	-	-	0.699	0.334
15.336	7^-	1.17	-	0.55	0.676	0.334
21.08	9^-	8.56	-	1.38	-	0.334
22.87	9^-	7.76	-	-	-	0.334
12.591	6^+	0.087	-	0.071	-	-
15.879	8^+	0.232	-	0.099	-	-
17.30	8^+	0.528	-	0.150	-	-

iii. Comparison with the $^{16}O(^{13}C,^{9}Be)^{20}Ne$ reaction

As mentioned in the first section of this chapter, to understand the origin of the structures in the $^{12}C(^{16}O,\alpha)$ reaction, it is necessary to compare the $^{16}O(^{12}C,^{8}Be)^{20}Ne$ reaction with the $^{16}O(^{13}C,^{9}Be)^{20}Ne$ one.

Similar α-transfer data of the $^{16}O(^{13}C,^{9}Be)^{20}Ne$ reaction at $E(^{13}C)$=105 MeV [31] are available. The angular distributions of this reaction are displayed in Figs. IV-7~9. Because the incident beam energy is similar to our present measurement and the α spectroscopic factor of $^{13}C_{g.s.}$ is as large as the one of $^{12}C_{g.s.}$, we expected more or less same results. However, two large differences were found between the $(^{12}C,^{8}Be)$ and $(^{13}C,^{9}Be)$ reactions. First, as the spin value of the residual ^{20}Ne nucleus is getting larger, the cross sections of the $(^{12}C,^{8}Be)$ reaction become significantly larger than those of the $(^{13}C,^{9}Be)$ reaction. In fact, though both reactions to the 1.63(2^+) and 4.25(4^+) MeV states show similar cross sections each other, the $^{16}O(^{12}C,^{8}Be)^{20}Ne$ reaction to the 15.4(7^-) and 21.08(9^-) MeV states have at least one order larger cross sections than the $^{16}O(^{13}C,^{9}Be)^{20}Ne$ reaction to the same states. Second, the angular distributions of the $(^{12}C,^{8}Be)$ reaction are much steeper than those of the $(^{13}C,^{9}Be)$ in the forward angle region. In order to examine whether these differences are explained by a kinematical matching condition or not, we performed EFR-DWBA calculation for the $^{16}O(^{13}C,^{9}Be)^{20}Ne$ reaction by using the same optical potentials. The parameters for the radial wave functions of the ^{8}Be-α and ^{16}O-α systems were also chosen as same as those for the $^{16}O(^{12}C,^{8}Be)^{20}Ne$ reaction (see Table IV-1 and

Figs. IV-8-10. The $^{16}O(^{13}C,^{9}Be)^{20}Ne$ angular distributions for the states in the ground state band (Fig. IV-8), $K^{\pi}=0^{-}$ band (Fig. IV-9) and $K^{\pi}=0^{+}_{4}$ band (Fig. IV-10) from ref. [31]. The solid curves are our results of the EFR-DWBA calculations.

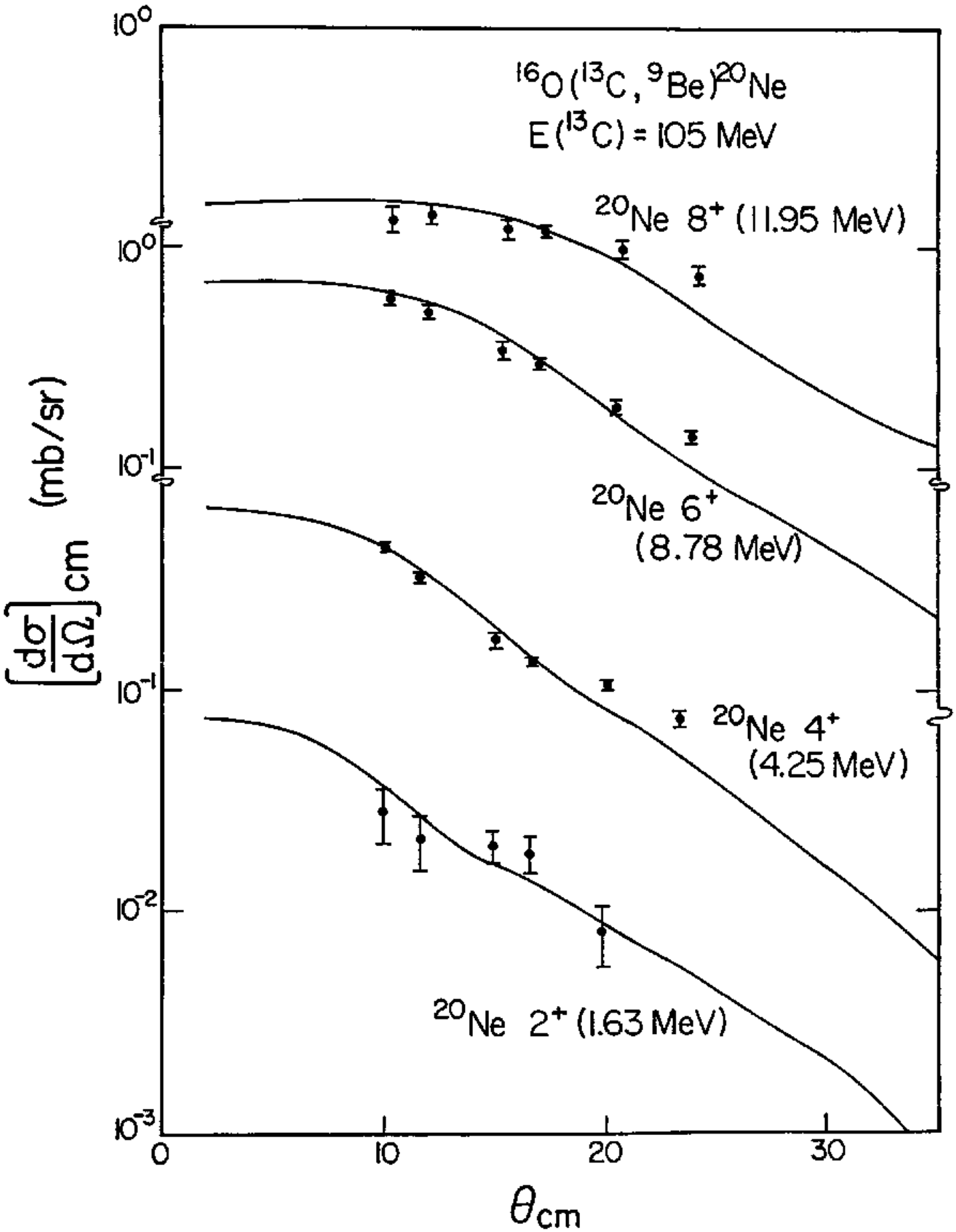
$^{16}O(^{13}C, ^{9}Be)^{20}Ne$
$E(^{13}C) = 105$ MeV
^{20}Ne 8$^+$ (11.95 MeV)
^{20}Ne 6$^+$ (8.78 MeV)
^{20}Ne 4$^+$ (4.25 MeV)
^{20}Ne 2$^+$ (1.63 MeV)
$\left[\frac{d\sigma}{d\Omega}\right]_{cm}$ (mb/sr)
θ_{cm}
10^0
10^0
10^{-1}
10^{-1}
10^{-2}
10^{-3}
0
10
20
30

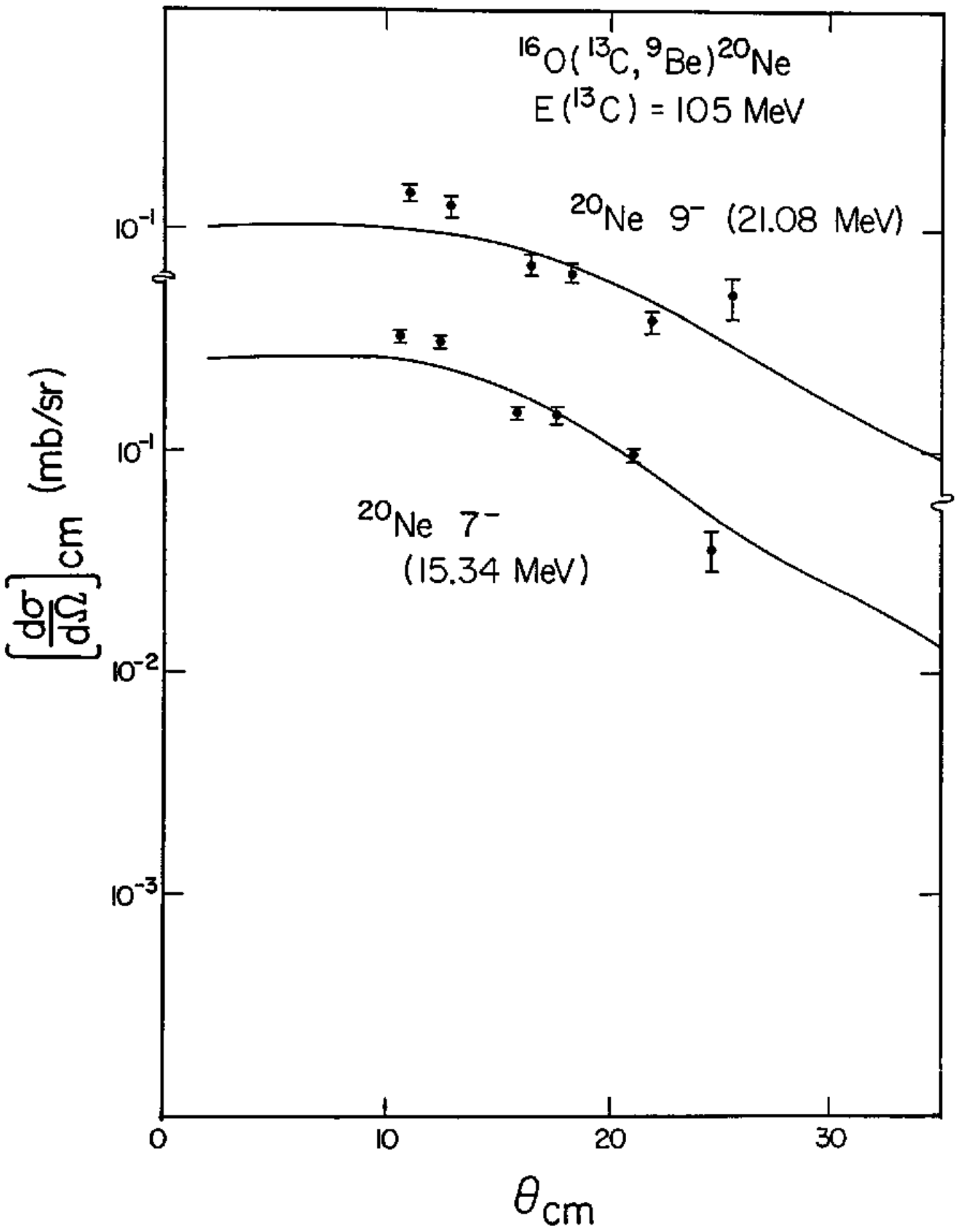
$^{16}O(^{13}C, ^{9}Be)^{20}Ne$
$E(^{13}C) = 105$ MeV
^{20}Ne 9^- (21.08 MeV)
^{20}Ne 7^-
(15.34 MeV)
$\left[\frac{d\sigma}{d\Omega}\right]_{cm}$ (mb/sr)
10^{-1}
10^{-1}
10^{-2}
10^{-3}
0
10
20
30
θ_{cm}

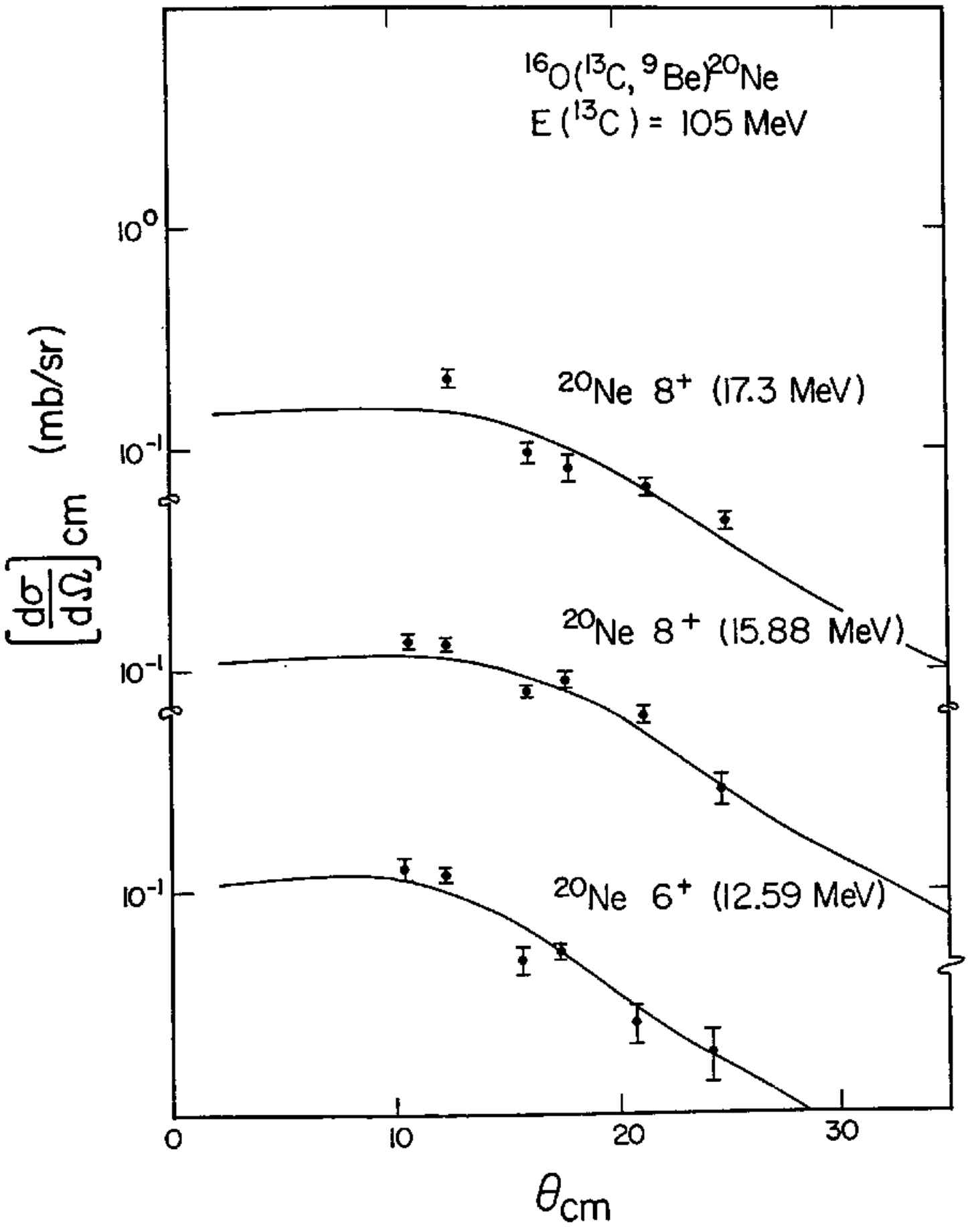
$^{16}O(^{13}C, ^{9}Be)^{20}Ne$
E(^{13}C) = 105 MeV
^{20}Ne 8$^+$ (17.3 MeV)
^{20}Ne 8$^+$ (15.88 MeV)
^{20}Ne 6$^+$ (12.59 MeV)
10^0
10^{-1}
10^{-1}
10^{-1}
$\left[\frac{d\sigma}{d\Omega}\right]_{cm}$ (mb/sr)
0
10
20
30
θ_{cm}

2). The results of the DWBA calculations are superimposed on the data in Figs. IV-8~10. The differences of the angular distributions between the ($^{12}C,^{8}Be$) and ($^{13}C,^{9}Be$) reactions are quite well reproduced by the calculation. Assuming that the ^{13}C spectroscopic factor is 0.4066 [50], we obtained the spectroscopic factors for the ^{20}Ne states from the normalization factor S_1S_2. The results (see Table IV-3) show large discrepancy with those from the $^{16}O(^{12}C,^{8}Be)^{20}Ne$ reaction. It should be noted, however, that the differences of the spectroscopic factors obtained by two reactions are smaller than those of their actual cross sections. This might mean that the kinematical matching condition qualitatively explains the differences between those two reactions. However the ambiguity of the DWBA calculation, which we have already mentioned, prevents us from drawing a definite conclusion that the differences of magnitudes are originated by the kinematical matching condition.

iv. Comparison with the $^{12}C(^{16}O,\alpha^{16}O)$ coincidence measurement

According to Sanders et al. [43] the α branching ratios (Γ_{α_0}/Γ) for the strongly populated states in ^{20}Ne via $^{16}O(^{12}C,^{8}Be_{g.s.})^{20}Ne^{*}$ reaction are roughly 100% with the exception of those for the 17.3 MeV (8^{+}) and 21.08 MeV (9^{-}) levels. This fact strongly implies that if the α-^{16}O coincidence measurement is performed in this system, prominent enhancements could be observed in the relative energy spectrum between α and ^{16}O particles. In fact results of recent coincidence measurement showed similar pattern of the structures in the α-^{16}O relative energy

spectra [25]. However, the energy assignment of those states; Ex(^{20}Ne)=8.8, 12.0, 14.3, 16.6, 20.5 and 27.0 MeV are somewhat different from our present results. The energy discrepancies might not be surprising if we consider the uncertainties involved in the analyses. Supposing first five of those states correspond to 8.775, 11.95+12.591, 15.336+15.879, 16.63+17.30, and 21.08 MeV states (unfortunately, we could not find the state correlate to 27.0 MeV one observed in the coincidence measurement), we can compare two experimental results. Since we have no information about the angular distribution of the decay process, we assume an isotropic decay. The decay branching ratio is supposed to be 100%. The results are summarized in Fig. IV-11. Closed circles represent coincidence data, while open circles mean α-transfer data. In this figure we do not show any error, but approximately 20% errors are expected. Despite there are consistently about a factor of two difference in absolute values, two experimental results show similar feature. This fact clearly shows that the α-transfer process can affect to the inclusive α-spectrum of the ^{12}C(^{16}O,α) reaction. The differences of magnitudes might come from the unfounded assumption of the decay process and the experimental error.

In summary of this chapter, we measured the ^{16}O(^{12}C,^{8}Be)^{20}Ne reaction at E(^{12}C)=109 MeV. This reaction showed many features as a direct reaction. In fact, the DWBA calculation can reproduce the general tendency of the angular distributions quite well. On the other hand, considering the fact that the absolute spectroscopic factors predicted by the DWBA calculation have large ambiguity, any assignments

Fig. IV-11. Comparison of the $^{16}O(^{12}C,^{8}Be)^{20}Ne$ single data (open circles) with the $^{12}C(^{16}O,\alpha^{16}O)^{8}Be$ coincidence data (closed circles) [25].

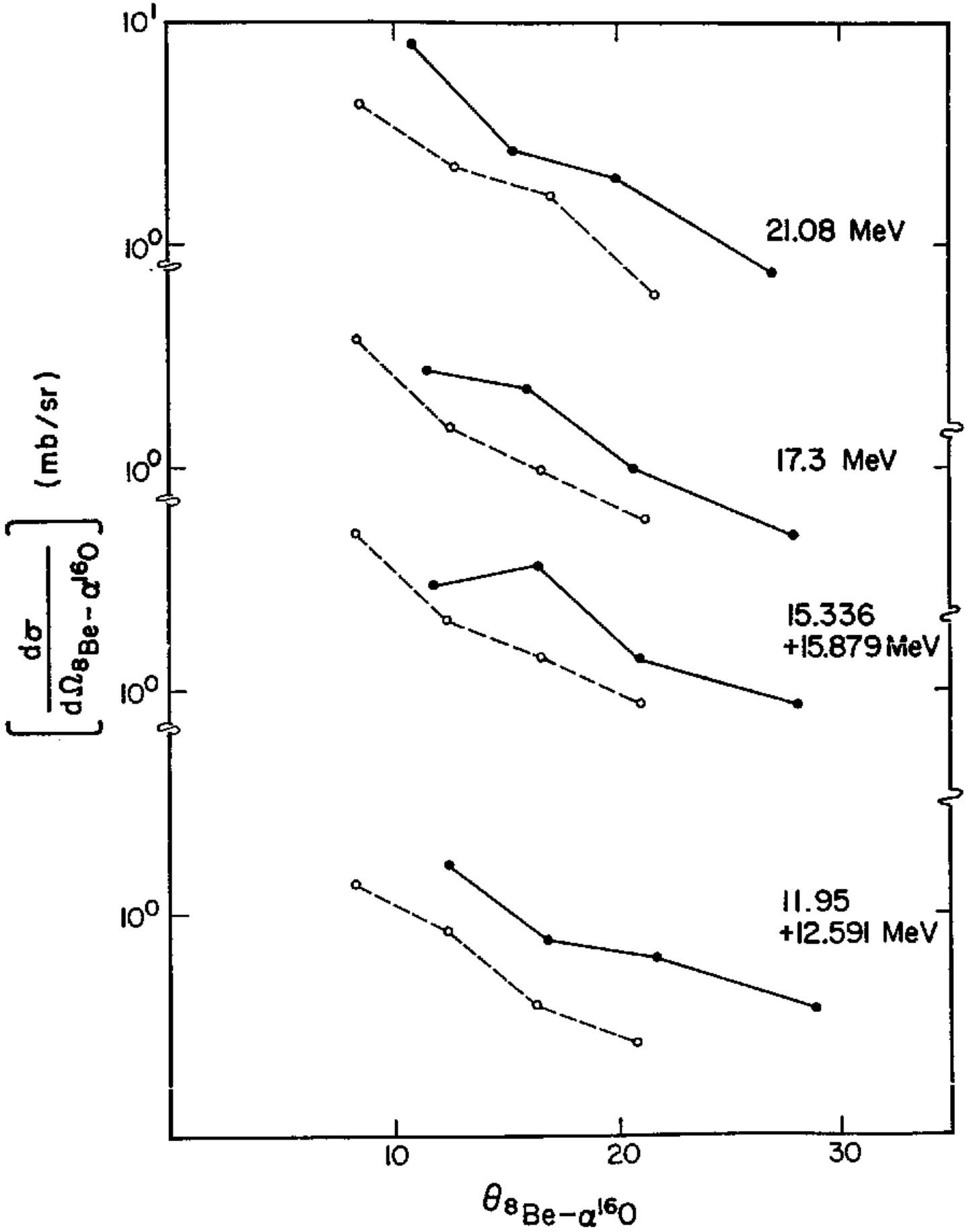
10¹
10⁰
10⁰
10⁰
10⁰
21.08 MeV
17.3 MeV
15.336
+15.879 MeV
11.95
+12.591 MeV
10
20
30
θ 8Be−α16O
[dσ / dΩ 8Be−α16O] (mb/sr)

of high-spin members of the rotational bands in ^{20}Ne cannot be performed. Compared with the $^{16}O(^{13}C,^{9}Be)^{20}Ne$ reaction, the $^{16}O(^{12}C,^{8}Be)^{20}Ne$ reaction shows approximately one order larger cross sections for the $E_x(^{20}Ne)>$ 15 MeV states. Since this large difference is able to explain the fact that the $^{12}C(^{16}O,\alpha)$ reaction show distinct structures, while the $^{13}C(^{16}O,\alpha)$ reaction does not, the sequential α-decay process of the $^{20}Ne^*$ might be an orign of the structures. To understand the difference of the $^{16}O(^{12}C,^{8}Be)^{20}Ne$ and $^{16}O(^{13}C,^{9}Be)^{20}Ne$ reactions, further careful investigations, especially theoretical ones, are required.

V. COMPREHENSIVE DISCUSSION

So far we have only described the experimental results of three different measurements related to the $^{12}C(^{16}O,\alpha)$ reaction independently. In this chapter we will try to extract the most consistent interpretation for the origin of the structures in the inclusive α-spectrum using those results. At the last part of this chapter, we will mention about the target dependence of the $(^{16}O,\alpha)$ reaction. Before going into a detailed discussion, we summarize our experimantal results once more together with the reported experimental results.

(i) The results of our coincidence measurement implied that the structures we observed in the inclusive α-spectrum of the $^{12}C(^{16}O,\alpha)$ reaction are not coming from the population of the molecular resonances or that the structures correspond to the molecular resonances but they do not have large ^{12}C-decay widths.

(ii) The results of the incident energy dependence measurement clearly showed that most of the structures in the $E_x(^{24}Mg)$=30-56 MeV region do not follow the two-body kinematics of the $^{12}C+^{16}O->^{24}Mg^*+\alpha$ reaction. The simple kinematical calculation suggested that the structures in this region might come from the sequential ejectile decay process of the $^{16}O^*$ and/or $^{20}Ne^*$.

(iii) The results of the coincidence measurements of the $^{12}C(^{16}O,\alpha^{12}C)^{12}C$ and $^{13}C(^{16}O,\alpha^{12}C)^{13}C$ reactions performed by Rae et al. [11] showed the importance of the sequential projectile decay process of the $^{16}O^*$ in these reactions. But the difference of the coincidence yield for this

process between two reactions were less than factor of two.

(iv) The results of the recent measurements of α-H.I. coincidences from the $^{12}C(^{16}O,\alpha)$ reaction performed by RCNP group [25] showed that the sequential decay process of the $^{20}Ne^*$ also plays an important role in the single α-spectrum.

(v) The results of the $^{16}O(^{12}C,^{8}Be)^{20}Ne$ reaction measurement supported the existence of the sequential decay process of the $^{20}Ne^*$. Moreover, a large cross section difference between the $^{16}O(^{12}C,^{8}Be)^{20}Ne$ and $^{16}O(^{13}C,^{9}Be)^{20}Ne$ reactions was found.

Considering the absence of the structures in the $^{13}C(^{16}O,\alpha)$ reactions, these facts strongly suggest that the sequential decay process of the $^{20}Ne^*$ has responsibility to show prominent structures in the inclusive α-spectrum of the $^{12}C(^{16}O,\alpha)$ reaction and that the molecular resonances are not so strongly populated by this reaction.

To check this explanation, we have attempted to calculate the magnitudes of the structures induced in the inclucive α-spectrum due to the sequential processes. For this purpose, we calculated spectra of α-particles coming from these processes at E_{lab}=145.2 MeV. We assumed the decay of $^{16}O^* \rightarrow {}^{12}C+\alpha$ and $^{20}Ne^* \rightarrow {}^{16}O+\alpha$ to be isotropic and integrated the α-^{12}C and α-^{16}O coincidence data [25] over all ^{12}C- and ^{16}O-directions following the prescription which is summarized in Appendix C. For interpolations and extrapolations of the angular distributions of the $^{16}O^*$ and $^{20}Ne^*$. we took into account the actual angular distribution of the $^{16}O(^{12}C,^{8}Be)^{20}Ne$ reaction. The results are shown in Fig. V-1 together with the background subtracted inclusive α-spectrum. The solid and dashed curves represent structures due to

Fig. V-1. Alpha spectra due to the sequential α-decay of the $^{20}Ne^*$ and $^{16}O^*$ by using the coincidence data [25]. The solid and dashed curves correspond to the $^{20}Ne^*$ and $^{16}O^*$ decay, respectively. The largest peaks are comig from $E_x(^{20}Ne)$=21.08 and $E_x(^{16}O)$=11.6 MeV, respectively. For comparison background subtracted α-spectrum is superimposed on the figure using the same scale.

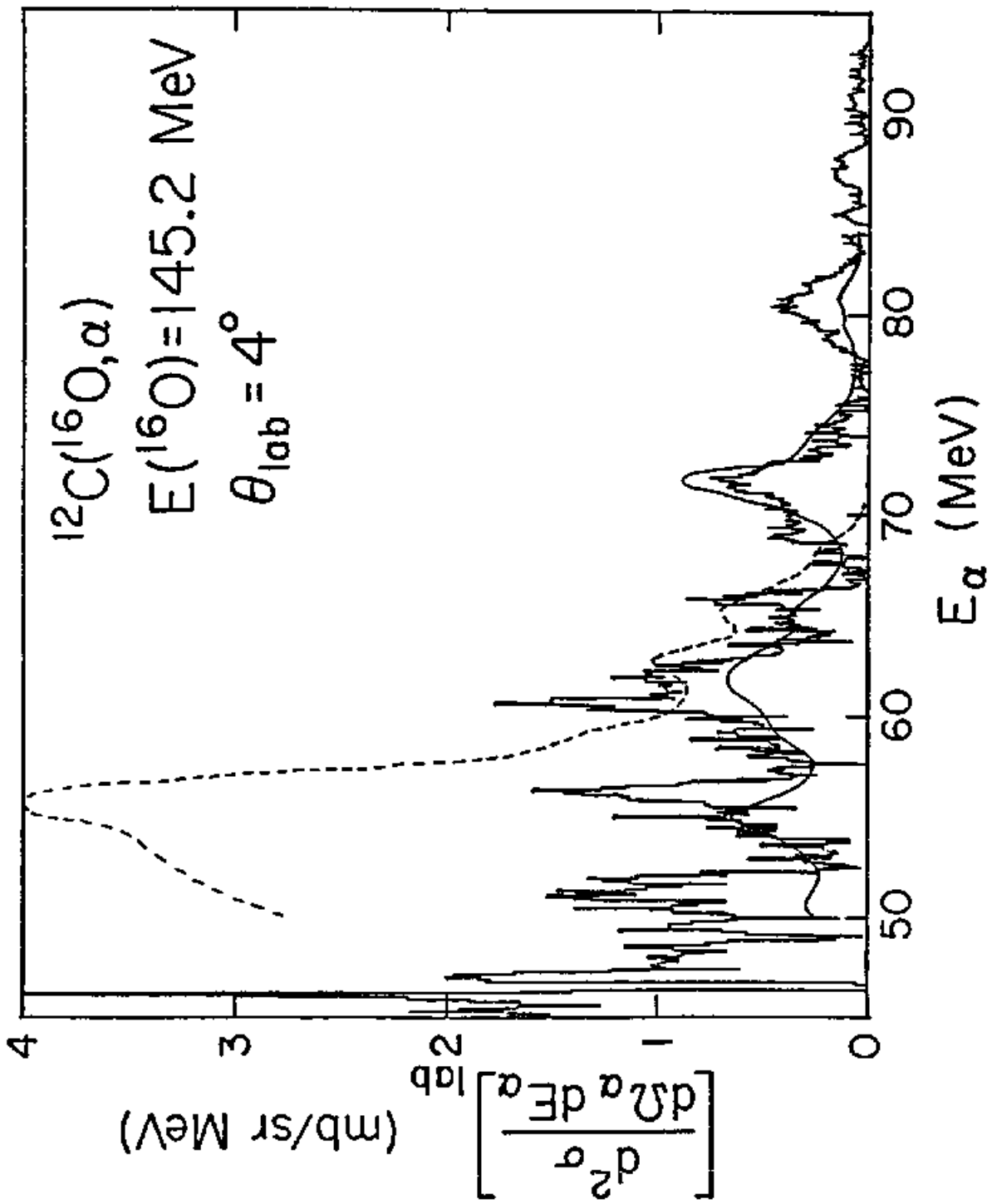
$^{12}C(^{16}O,\alpha)$
$E(^{16}O)=145.2$ MeV
$\theta_{lab} = 4°$
$\left[\frac{d^2\sigma}{d\Omega_\alpha\, dE_\alpha}\right]_{lab}$ (mb/sr MeV)
E_α (MeV)
0
1
2
3
4
50
60
70
80
90

the sequential decay of the $^{20}Ne^*$ and $^{16}O^*$. respectively. As seen in this figure, the calculated structures are comparable to those we observed in the inclusive α-spectrum. Moreover the positions of the structures are also reproduced by this calculation. Most of the structures seem to be explained by the sequential decay process of the $^{20}Ne^*$ except for the peak around E_α=56 MeV. This peak probably comes from the sequential decay of the $^{16}O^*$, because that process can make a huge structure around E_α=56 MeV according to our calculation. If this interpretation is correct, we might observe similar structure in the $^{13}C(^{16}O,\alpha)$ reaction at the same α energy. Unfortunately, the experimental data of the $^{13}C(^{16}O,\alpha)$ reaction obtained by Takahashi et al. [19] did not include this energy region, so we can not check our interpretation at this time. In case of the $^{13}C(^{16}O,\alpha)$ reaction, we cannot expect to observe significant structures from the $^{20}Ne^*$ seqeuntial decay, since the $^{16}O+^{13}C\rightarrow ^{20}Ne^*+^{9}Be$ reaction has approximately one order smaller cross section than the $^{16}O+^{12}C\rightarrow ^{20}Ne^*+^{8}Be$ reaction. It should be noted that the calculated magnitudes and positions of the structures very much depend on the angular distribution of the decay processes of the $^{16}O^*$ and $^{20}Ne^*$. For instance, if we assume the decays are axially symmetric about the recoil direction of the $^{16}O^*$ or $^{20}Ne^*$ but have a $1/\sin\theta$ angular distribution with respect to the recoil direction, we get approximately factor of three larger structures and their positions change naerly 500 keV. Even though there is such ambiguity of the caculation, we might conclude that most of the structures we observed in the inclusive α-spectrum of the $^{12}C(^{16}O,\alpha)$ reaction come from the sequential ejectile decay processes, especially from the $^{20}Ne^*$.

If we examine the angular dependence of the structures carefully, as seen in Fig. V-2, small movements of them in term of the excitation energy of the ^{24}Mg are observed. This fact again suggests the sequential ejectile processes. It would be fair to mention the difficulties of reproducing the rapid decrease of the magnitudes of the structures as a function of a laboratory angle. If we assume the isotropic decay of the ejectiles $^{20}Ne^*$ and $^{16}O^*$, the decrease is not large enough, while if we assume that the decays have a $1/\sin\theta$ angular distribution around the recoil direction, the rate of decreasing is similar to the experimental one. Since the results of the calculation strongly depend on the angular distributions of the decay processes, we would just point out that the sequential decay picture is not inconsistent with the observed angular dependence.

Because now we know that the most components of the prominent structures in the inclusive α spectra of the $^{12}C(^{16}O,\alpha)$ reaction are coming from the ejectile sequantial α-decay processes, we should re-examine the target dependence data. The experimental results of a $^{16}O(^{14}N,^{10}B)^{20}Ne$ reaction at $E_{lab}(^{14}N)$= 155 MeV, θ_{lab}=9.3° [36] showed that the cross sections for the $E_x(^{20}Ne)$=15.3(7^-) and 21.08(9^-) states were several hundred μb/sr. These values are comparable to the $^{16}O(^{13}C,^{9}Be)^{20}Ne$ reaction but approximately one order smaller values than those of the $^{16}O(^{12}C,^{8}Be)^{20}Ne$ reaction. This fact strongly suggests that the structures due to the sequential decay of the $^{20}Ne^*$ could not appear in the inclusive α-spectrum of the $^{14}N(^{16}O,\alpha)$ reaction, and that is indeed the case. About $^{16}O(^{16}O,^{12}C)^{20}Ne$ and $^{16}O(^{20}Ne,^{16}O)^{20}Ne$ reactions, there are no informations right now. We calculate the expected positions of the structures due to the

Fig. V-2. Angular dependence of the structures taken by solid state counter telescopes at E(^{16}O)=148 MeV. For convenience, the horizontal axis represents the scale of the excitation energies in the ^{24}Mg system.

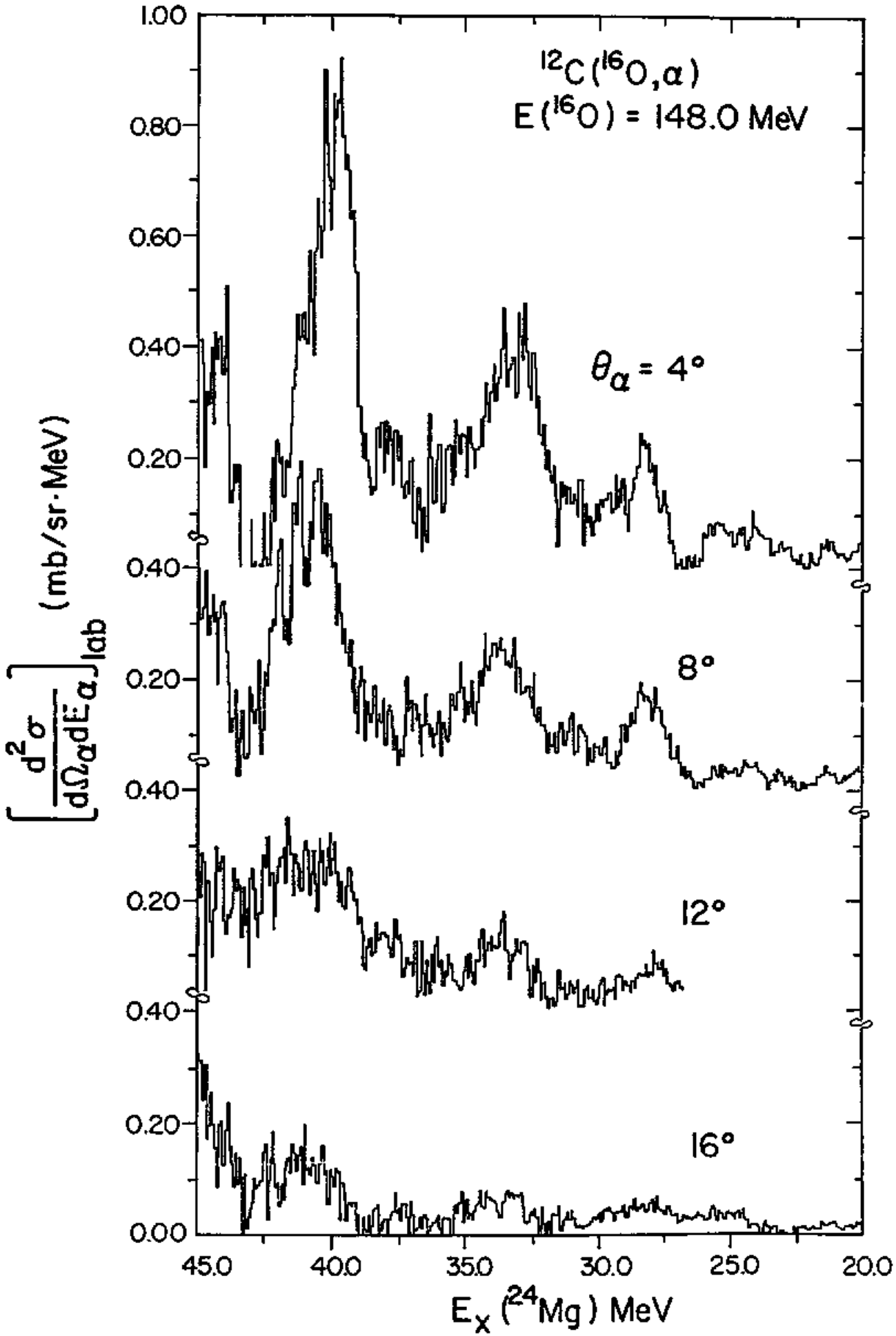
$^{12}C(^{16}O,\alpha)$
$E(^{16}O) = 148.0$ MeV
$\theta_\alpha = 4°$
8°
12°
16°
$\left[\frac{d^2\sigma}{d\Omega_\alpha dE_\alpha}\right]_{lab}$ (mb/sr·MeV)
E_x (^{24}Mg) MeV
1.00
0.80
0.60
0.40
0.20
0.00
45.0
40.0
35.0
30.0
25.0
20.0

sequential decay of the $^{20}Ne^*$ and $^{16}O^*$ using the simple kinematics (Appendix C-(a)). The same assumptions which we mentioned in III D were also used. But at this time we used correct excitation energies of $^{20}Ne^*$ obtained by the $^{16}O(^{12}C,^{8}Be)^{20}Ne$ reaction except for $E_x(^{20}Ne)$= 26.7 MeV. The results are shown in Figs. V-3~7 together with the experimental data [19]. As seen in these figures, most of the prominent structures might be understood by the sequential decay processes of the $^{20}Ne^*$, although we cannot exclude the contribution of the $^{16}O^*$.

Fig. V-3-7. Expected positions of the structures due to the sequential α-decay processes. Solid and dashed arrows correspond to those due to the $^{20}Ne^*$ and $^{16}O^*$, respectively. The excitation energies included are $E_x(^{20}Ne)$=26.7, 22.87, 21.08, 17.30, 15.88, 15.34, 12.59, 11.95, 10.79, 10.26 and 8.78 MeV and $E_x(^{16}O)$=19.4, 15.8, 13.1, 11.6 and 10.4 MeV [11]. (The higher excitation appears more right-side.) The experimental data are taken from ref. [14].

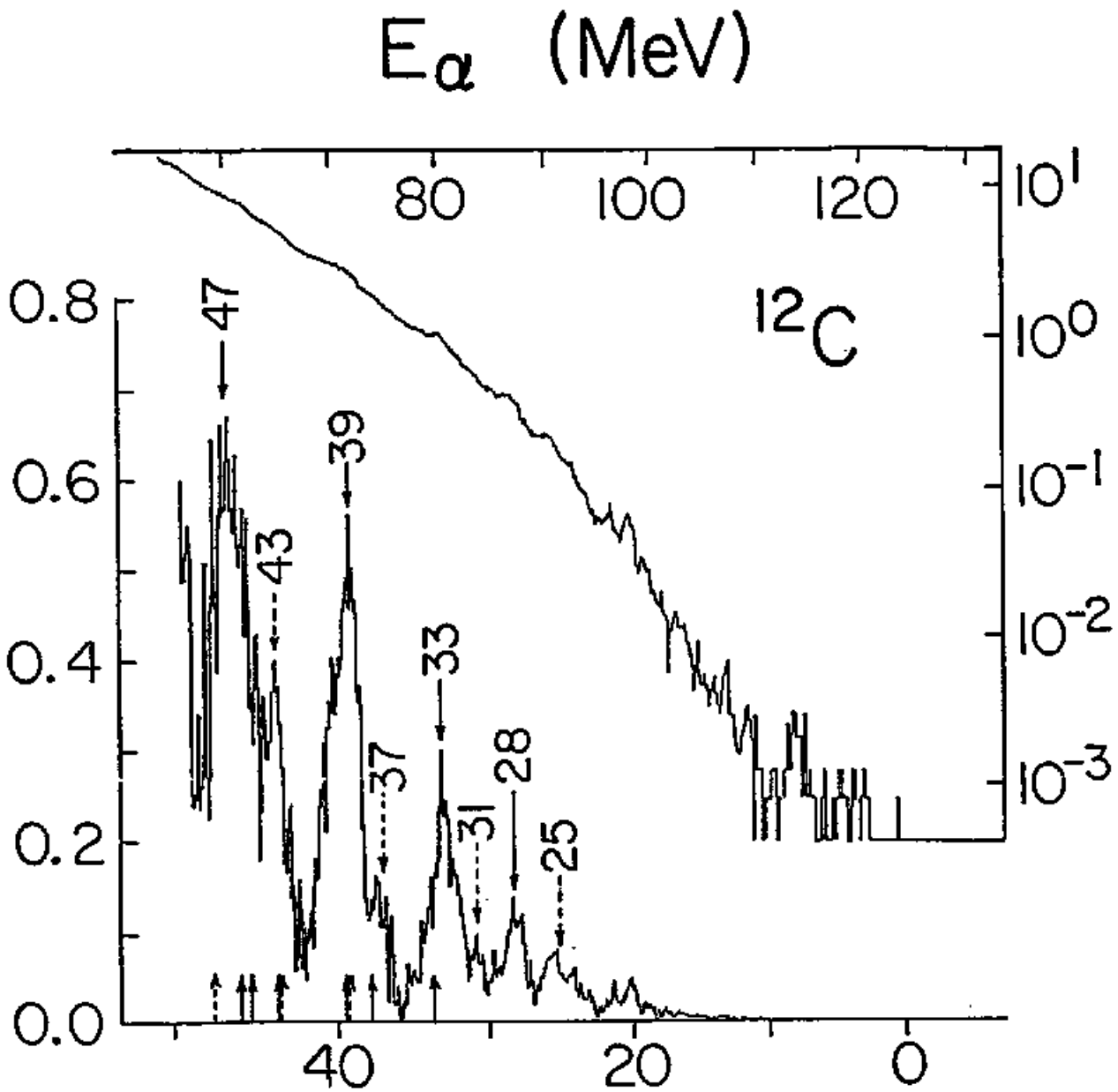
E_α (MeV)
80
100
120
10^1
10^0
10^{-1}
10^{-2}
10^{-3}
^{12}C
0.8
0.6
0.4
0.2
0.0
47
43
39
37
33
31
28
25
40
20
0

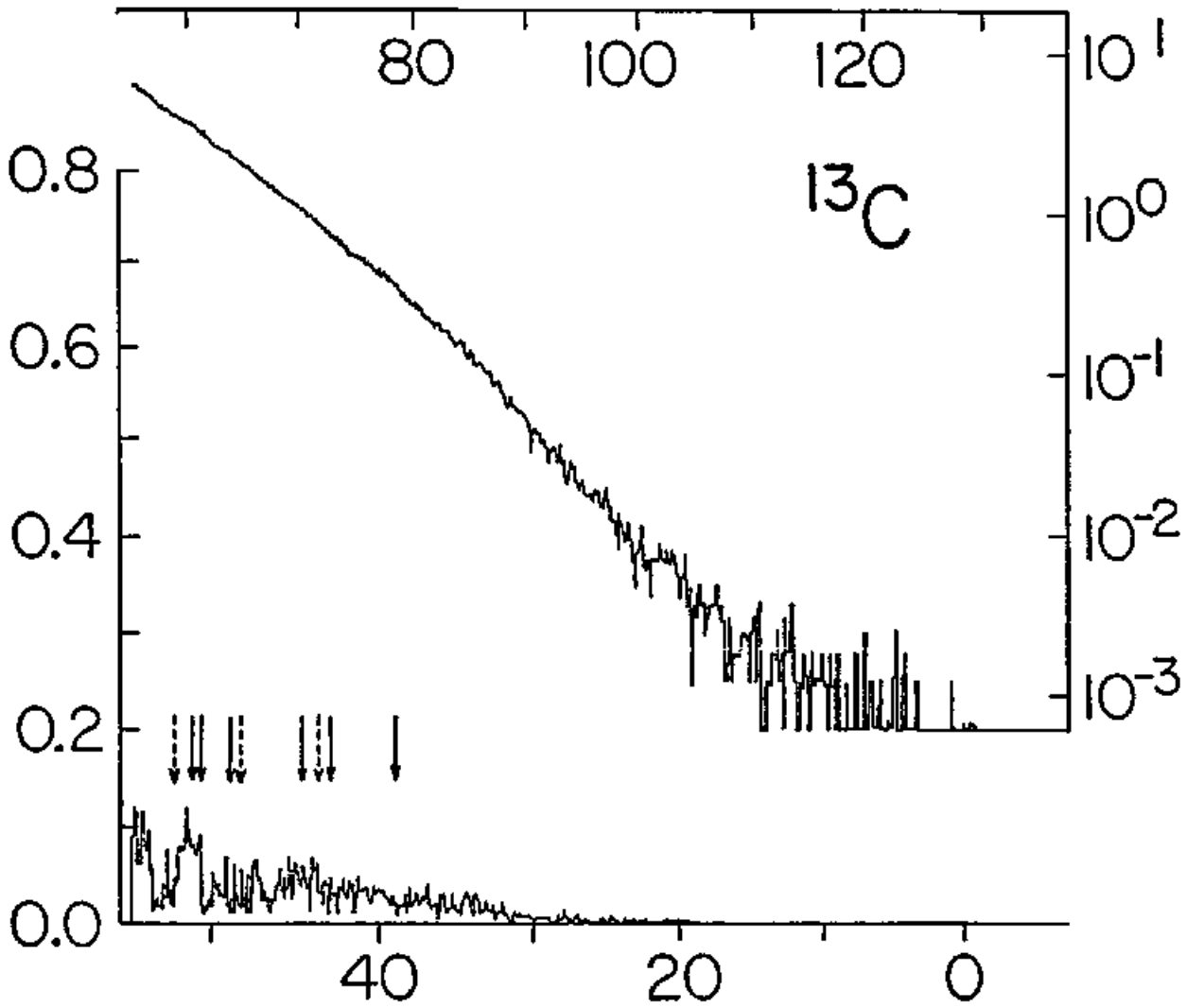
80
100
120
10^{1}
0.8
^{13}C
10^{0}
0.6
10^{-1}
0.4
10^{-2}
0.2
10^{-3}
0.0
40
20
0

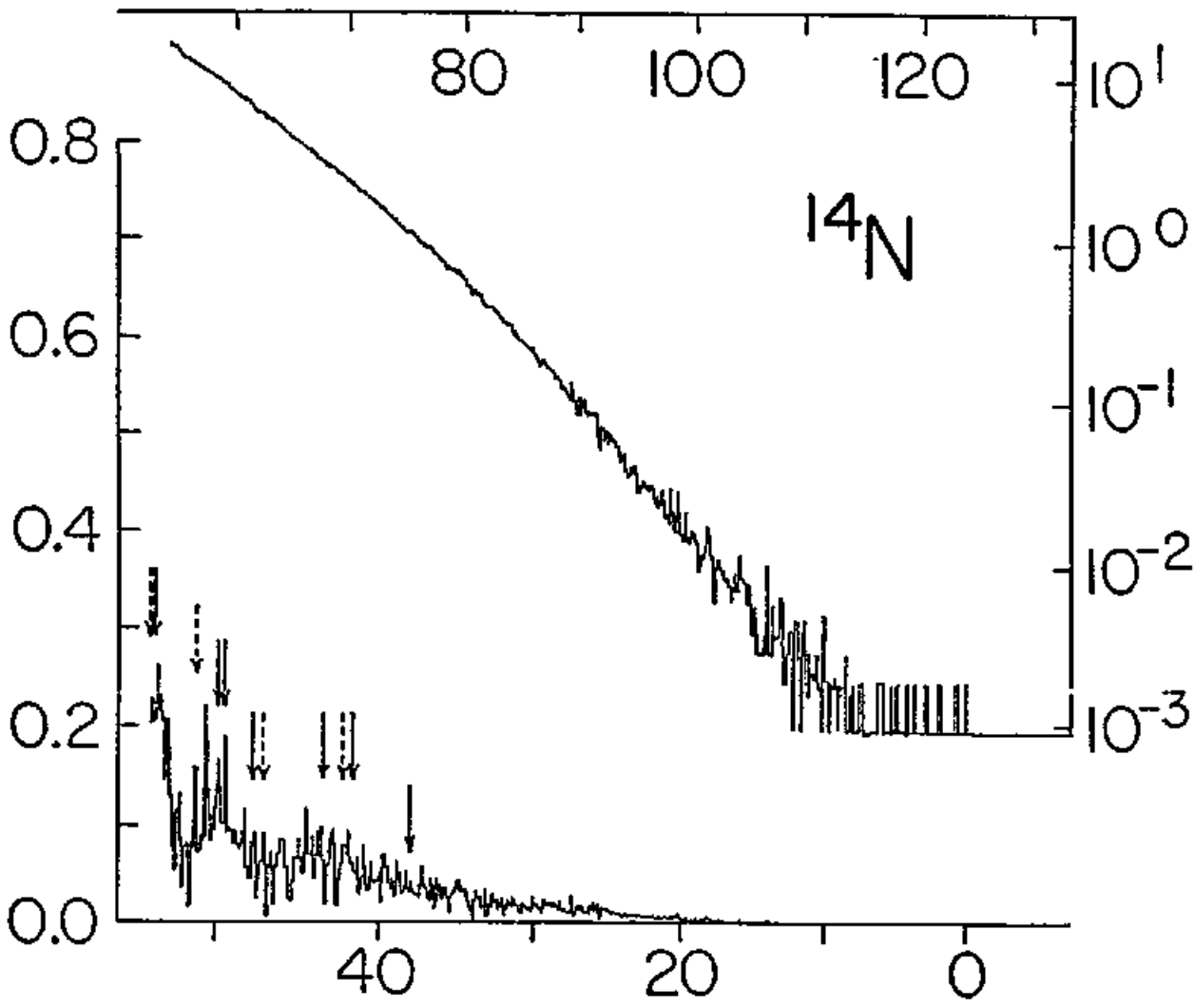
80
100
120
10^{1}
0.8
^{14}N
10^{0}
0.6
10^{-1}
0.4
10^{-2}
0.2
10^{-3}
0.0
40
20
0

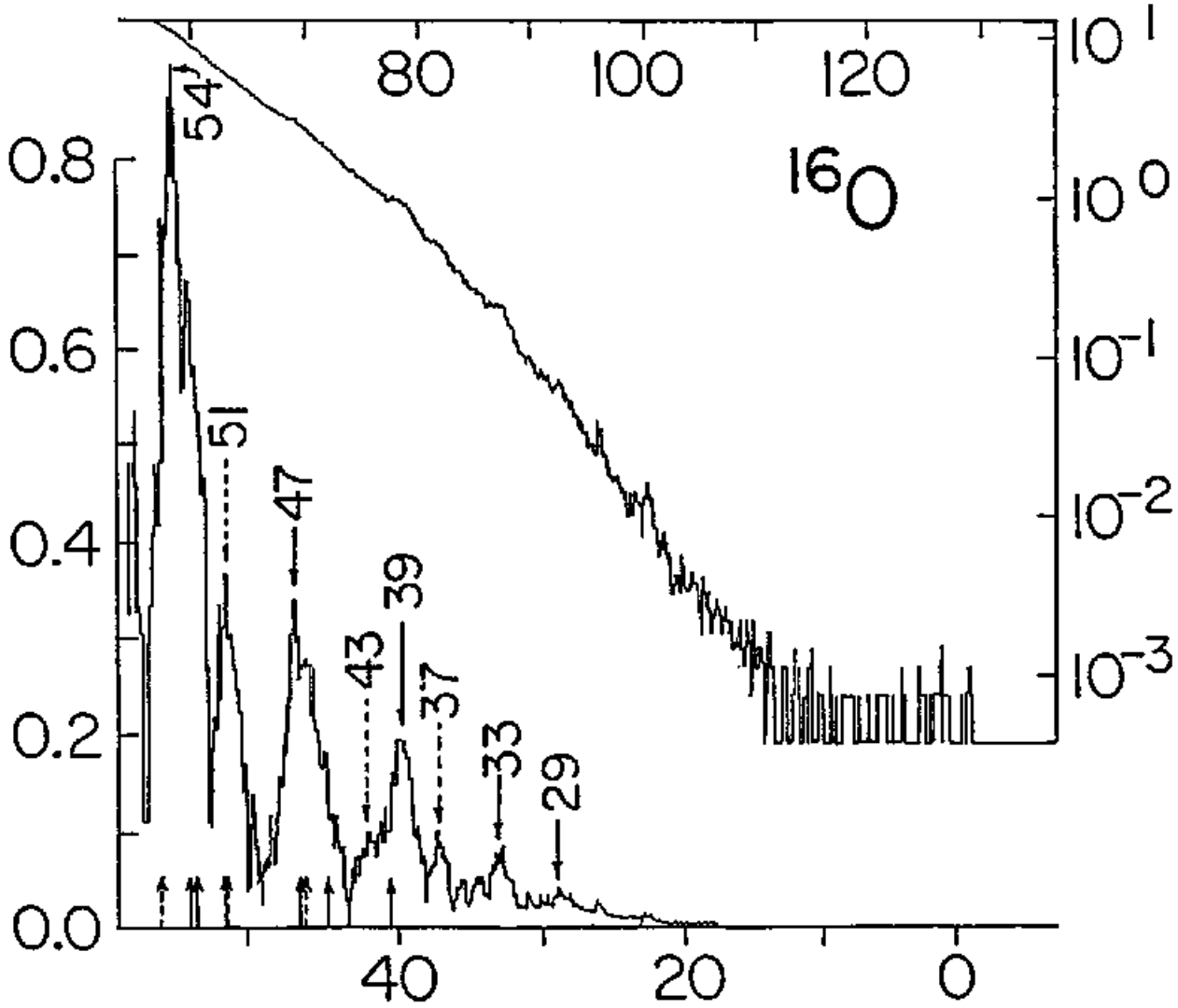
80
100
120
^{16}O
54
51
47
43
39
37
33
29
0.8
0.6
0.4
0.2
0.0
40
20
0
10^{1}
10^{0}
10^{-1}
10^{-2}
10^{-3}

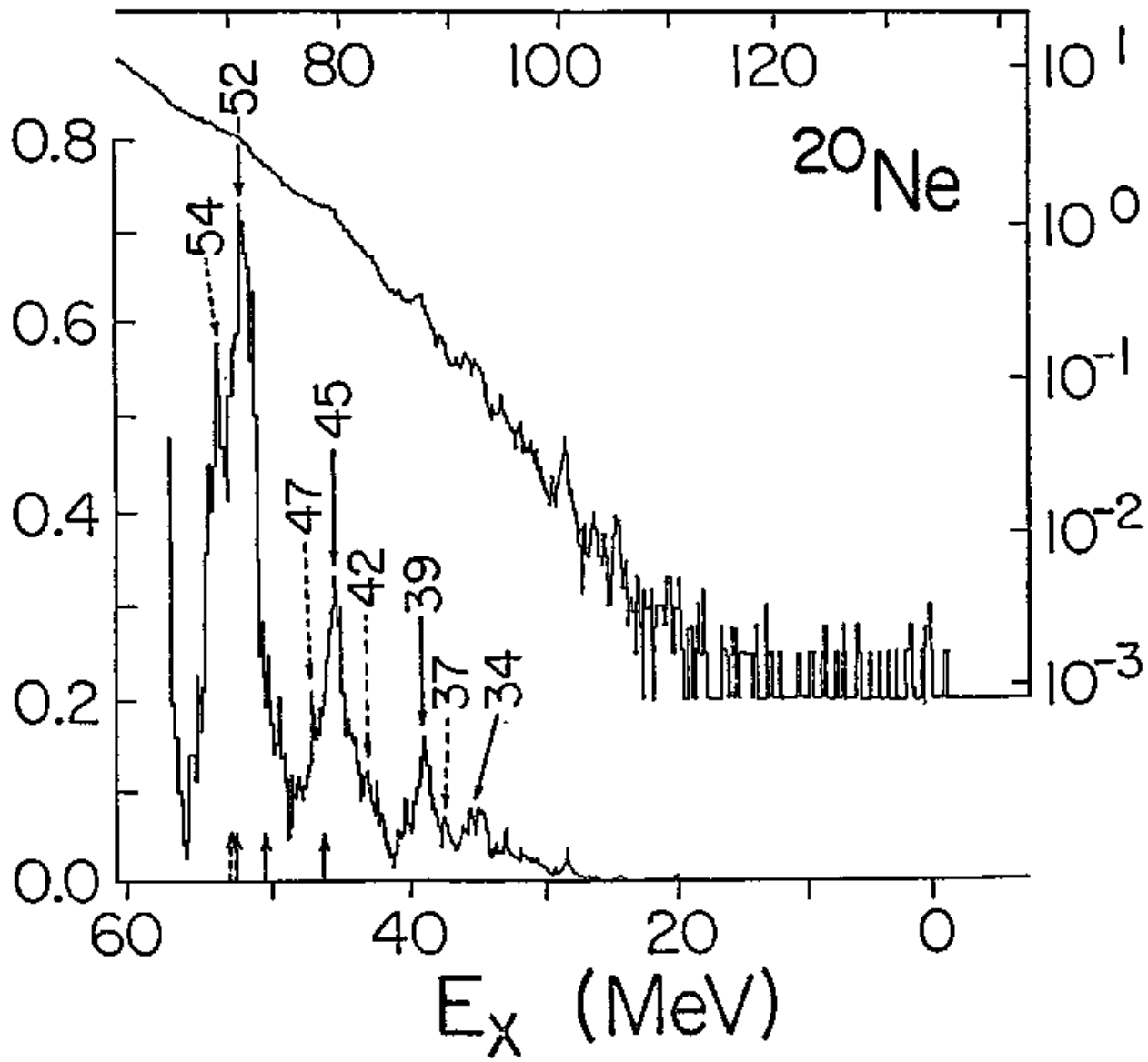
80
100
120
52
^{20}Ne
54
45
47
42
39
37
34
0.8
0.6
0.4
0.2
0.0
10^{1}
10^{0}
10^{-1}
10^{-2}
10^{-3}
60
40
20
0
E_x (MeV)

VI. SUMMARY

The coincidence measurement of the α-^{12}C and ^{12}C-^{12}C particles induced by the 145 MeV ^{16}O bombardment of ^{12}C, the incident energy dependence measurement of the $^{12}C(^{16}O,\alpha)$ reaction, and the measurement of the $^{16}O(^{12}C,^{8}Be)^{20}Ne$ reaction at E_{lab}=109 MeV were carried out in order to determine the origin of the structures in the inclusive α-spectra of the $^{12}C(^{16}O,\alpha)$ reaction. Contrary to the previous suggestion, we could not find out any evidence of existence of the molecular resonances as a final state interaction of the $^{12}C(^{16}O,\alpha)$ reaction. The measurement of the incident energy dependence of the $^{12}C(^{16}O,\alpha)$ reaction clearly showed that the most part of the structures in the inclusive α-spectrum is coming from the sequential ejectile decay processes of the $^{16}O^*$ and $^{20}Ne^*$. Considering the difference between the $^{12}C(^{16}O,\alpha)$ and $^{13}C(^{16}O,\alpha)$ reactions, the sequential decay of the $^{20}Ne^*$ is favorable, because the cross sections of the $^{20}Ne^*$ formation in the $^{12}C+^{16}O\rightarrow^{20}Ne+^{8}Be$ reaction is much larger than those in the $^{13}C+^{16}O\rightarrow^{20}Ne+^{9}Be$ reaction. In fact, using the sequential decay process of the $^{20}Ne^*$. we can explain most of the experimental results qualitatively. But several questions have still remained, like why the $^{16}O(^{12}C,^{8}Be)^{20}Ne$ reaction shows different behavior from the $^{16}O(^{13}C,^{9}Be)^{20}Ne$ reaction and so on. It is desired to carry out further investigations about the α-transfer reactions on the ^{16}O target, especially theoretical one.

ACKNOWLEDGEMENTS

The experiments reported in this thesis were performed at the Cyclotron Institute, Texas A&M University under the direction of Profs. K. Nagatani and R. E. Tribble. I would like to thank Profs. D. H. Youngblood, K. Nagatani and S. Kobayashi for giving me opportunity to visit Texas A&M University during my graduate course in Kyoto University. While staying there, I have taken great advantage to perform experiments owing to technical staffs and machine operators. I am very grateful to them.

I also thank many collaborators, Drs. N. Takahasi, E. Takada, R. E. Neese, Y.-W. Lui, E. Ungricht, Ms. D. M. Tanner, and Mr. Y. Mihara for the experimental works. For the detecting system, I am very indebted to Drs. N. Takahashi and Y.-W. Lui. For the modification of acquisition program, I owe much to Mr. Y. Mihara. Without discussion with Dr. E. Ungricht, I could not have gotten any interpretation of the $^{12}C(^{16}O,\alpha)$ reaction.

For the theoretical aspect, Profs. T. Tamura and M. Ichimura, Drs. T. Izumoto and Y. Kondo have given me many useful ideas.

It is impossible to forget the helps that Prof. K. Nagatani, my actual supervisor, has given me. Without his suitable advices and guidances, this investigation would not have been possible. After his leaving, Prof. R. E. Tribble had taken care of my research. I greatly appreciate his helpful suggestions. Finally, I should thank my parents and lots of my friends for their constant encouragement and moral support that have helped me to continue researching work throughout my graduate course.

This work was supported in part by the U. S. Department of Energy and the R. A. Welch Foundation.

REFERENCES

[1] D.A. Bromley, J.A. Kuehner, and E. Almqvist, Phys. Rev. Lett. 4 (1960) 365.

[2] N. Anyas-Weiss, J.C. Cornell, P.S. Fisher, P.N. Hudson, A. Menchaca-Rocha, D.J. Millener, A.D. Panagiotou, D.K. Scott and D. Strottman, Phys. Rep. 12 (1974) 201.

[3] F.S. Goulding and B.G. Harvey, Ann. Rev. of Nucl. Sci., 25 (1975) 167.

[4] J.O. Newton and S.H. Sie, Nucl. Phys. A334 (1980) 499.

[5] K. Nagatani, T. Shimoda, D. Tanner, R. Tribble and T. Yamaya, Phys. Rev. Lett. 43 (1979) 1480.

[6] D.A. Bromley, Proc. Int. Workshop on resonances in heavy-ion collisions, Bad Honnef, Germany, 1981 ed. K.A. Eberhard (Springer-Verlag, 1982) p.3;
P. Taras, Proc. Third Int. Conf. on clustering aspects of nuclear structure and nuclear reactions, Winnipeg, Canada, 1978, AIP Conf. Proc. 47 (1978) 234

[7] T.M. Cormier, J. Applegate, G.M. Berkowitz, P. Braun-Munzinger, P.M. Cormier, J.W. Harris, C.M. Jachcinski, L.L. Lee Jr., J. Barrette and H.E. Wegner, Phys. Rev. Lett. 38 (1977) 940;
T.M. Cormier, C.M. Jachcinski, G.M. Berkwitz, P. Braun-Munzinger, P.M. Cormier, M. Gai, J.W. Harris, J. Barrette, and H.E. Wegner, Phys. Rev. Lett. 40 (1978) 924.

[8] R.L. McGrath, D. Abriola, J. Karp, T. Renner, and S.Y. Zhu, Phys. Rev. C24 (1981) 2374.

[9] V. Metag, A. Lazzarini, K. Lesko, and R. Vandenbosch, Phys. Rev. C25 (1982) 1486.

[10] A.J. Lazzarini, E.R. Cosman, A. Sperduto, S.G. Steadman, W. Thoms and G.R. Young, Phys. Rev. Lett. 40 (1978) 1426.

[11] W.D. Rae, R.G. Stokstad, B.G. Harvey, A. Dacal, R. Legrain, J. Mahoney, M.J. Murphy and T.J.M. Symons, Phys. Rev. Lett. 45 (1980) 884.

[12] D. Branford, M.J. LeVine, J. Barrette and S. Kubono, Phys. Rev. C23 (1981) 549.

[13] M. Ichimura, E. Takada, T. Yamaya and K. Nagatani, Phys. Lett. 101B (1981) 31.

[14] N. Takahashi, T. Yamaya, R. Tribble, E. Takada, Y.-W. Lui, D. Tanner and K. Nagatani, Phys. Lett. 108B (1982) 177.

[15] A. Szanto de Toledo, M. M. Coimbra, N. Carlin Filho, T. M. Cormier and P. M. Stwertka, Phys. Rev. Lett. 47 (1981) 632.

[16] H.V. Klapdor, G. Rosner, H.Reiss, and M. Schrader, Nucl. Phys. A244 (1975) 157.

[17] N. Takahashi, E. Ungricht, T. Murakami, Y.-W. Lui, R. Neese, D. Tanner, R. Tribble and K. Nagatani, Phys. Lett. 110B (1982) 445.

[18] J.S. Karp, D. Abriola, R.L. McGrath, W.A. Watson, and J. Cheng-Lie, Bull. Am. Phys. Soc. 27 (1982) 698.

[19] N. Takahashi, T. Yamaya, E. Takada, Y.-W. Lui and K. Nagatani, Nucl. Instr. and Meth. 196 (1982) 253.

[20] L.C. Northcliffe, and R.F. Schilling, Nucl. Data Tables, A7 (1970) 233.

[21] E. Ungricht, "Progress in Research", Texas A&M University Cyclotron Institute Report, September 1982 (unpublished).

[22] F. Puehlhofer, Nucl. Phys. A280 (1977) 267.

[23] D.W. Lang, Nucl. Phys. 77 (1966) 545.

[24] S.M. Lee, T. Matsuse and A. Arima, Phys. Rev. Lett. 45 (1980) 165.

[25] T. Shimoda, S. Shimoura, T. Fukuda, M. Tanaka, H. Ogata, I. Miura, E. Takada, M.-K. Tanaka, K. Takimoto, and K. Katori, to be published;
K. Katori, T. Shimoda, T. Fukuda, H. Ogata, I. Miura and M. Tanaka, Reserch Center for Nuclear Physics, Osaka, annual report (1980) p.119, unpublished.

[26] P.M. Stwertka, T.M. Cormier, M. Herman, N. Nicolas, A. Szanto de Toledo, M.M. Coimbra, and N. Carlin Filho, Phys. Rev. Lett. 49 (1982) 640.

[27] R.G. Stockstad, Internal Report 52, Wright Nuclear Structure Laboratory, Yale University, May 1972 (unpublished).

[28] L.R. Greenwood, K. Katori, R.E. Malmin, T.H. Braid, J.C. Stoltzfus, and R.H. Siemssen, Phys. Rev. C6 (1972) 2112.

[29] A. Szanto de Toledo, T.M. cormier, M. Herman, B. Lin, P.M. Stwertka, M.M. Coimbra, and N. Carlin Filho, Phys. Rev. Lett. 47 (1981) 1881.

[30] T.M. Cormier, A. Szanto de Toledo, M.M. Coimbra, N. Carlin Filho, P.M. Stwertka, M, Herman, N. Nicolis, Phys. Lett. 118B (1982) 303.

[31] H.S. Bradlow, W.D. Rae, P.S. Fisher, N.S. Godwin, G. Proudfoot, and D. Sinclair, Nucl. Phys. A314 (1979) 171.

[32] M. Ichimura, A. Arima, E.C. Halbert, and T. Terasawa, Nucl. Phys. A204 (1973) 16.

[33] T. Matsuse and M. Kamimura, Prog. Theor. Phys. 49 (1973) 1765.

[34] T. Tanabe, M. Yasue, K. Sato, K. Ogino, Y. Kadota, Y. Taniguchi, K. Obori, K. Makino, and M. Tochi, Phys. Rev. C24 (1981) 2556; K.P. Artemov, V.Z. Gol'dberg, I.P. Petrov, V.P. Rudakov, I.N. Serikov, and V.A. Timofeev, Sov. J. Nucl. Phys. 23 (1976) 257; and references therein.

[35] M.E. Cobern, D.J. Pisano, and P.D. Parker, Phys. Rev. C14 (1976) 491.

[36] K. Nagatani, C.W. Towsley, K.G. Nair, R. Hanus, M. Hamm, and D. Strottman, Phys. Rev. C14 (1976) 2133.

[37] F. Pougheon, P. Roussel, M. Bernas, F. Diaf, B. Fabbro, F. Naulin, E. Plagnol, and G. Rotbard, Nucl. Phys. A325 (1979) 481.

[38] Y. Fujiwara, H. Horiuchi, K. Ikeda, M. Kamimura, K. Kato, Y. Suzuki, and E. Uegaki, Suppl. Prog. Theor. Phys. 68 (1980) 29.

[39] G.J. Wozniak, N.A. Jelley, and J. Cerny, Nucl. Instr. and Meth. 120 (1974) 29.

[40] E. Mathiak, K.A. Eberhard, J.G. Cramer, H.H. Rossner, J. Stettmeir, and A. Weidinger, Nucl. Phys. A259 (1976) 129.

[41] R.E. Brown, J.S. Blair, D. Bodansky, N. Cue, and C.D. Kavalosky, Phys. Rev. 138 (1965) B1394.

[42] F. Ajzenberg-Selove, Nucl. Phys. A300 (1978) 1.

[43] S.J. Sanders, L.M. Martz, and P.D. Parker, Phys. Rev. C20 (1979) 1743.

[44] D. Strottman, N. Anyas-Weiss, J.C. Cornell, P.S. Fisher, P.N. Hudson, A. Menchaca-Rocha, A.D. Panagiotou, and D.K. Scott, Phys. Lett. 47B (1973) 16.

[45] C. Bergman, and R.K. Hobbie, Phys. Rev. C3 (1971) 1729.

[46] T. Tamura and K.S. Low, Comp. Phys. Comm. 8 (1974) 349.

[47] T. Tamura, T. Udagawa, K.E. Wood, and H. Amakawa, Comp. Phys. Comm. 18 (1979) 163.

[48] R.M. DeVries, Phys. Rev. C11 (1975) 2105.

[49] B. Buck, C.B. Dover, and J.P. Vary, Phys. Rev. C11 (1975) 1803.

[50] D. Kurath, Phys. Rev. C7 (1973) 1390.

APPENDICES

A. Three-body Kinematics

In this appendix we summarize the notations of the three-body system and the relevant explicit transformations that were used for the data analyses. In following equations, the subscripts p and t refer to the projectile and target particle, the subscripts i, j, and k refer to the three final particles and the superscripts l and c refer to laboratory and center-of-mass systems, respectively. The symbols m_i, p_i and E_i denote the mass, momentum, and energy of particle i. Using these, we define the following reduced masses and momentum vectors:

$$M=m_i+m_j+m_k$$
$$=m_p+m_t, \tag{A1}$$

$$\mu_{ij}=m_i m_j/(m_i+m_j). \tag{A2}$$

$$\mu_{i-jk}=m_i(m_j+m_k)/M, \tag{A3}$$

$$\vec{P}=\vec{p}_i+\vec{p}_j+\vec{p}_k$$
$$=\vec{p}_p+\vec{p}_t, \tag{A4}$$

$$\vec{p}_{ij}=\mu_{ij}(\vec{p}_i/m_i-\vec{p}_j/m_j), \tag{A5}$$

$$\vec{p}_{k-ij}=\mu_{k-ij}[\vec{p}_k/m_k-(\vec{p}_i+\vec{p}_j)/(m_i+m_j)]$$
$$=(m_i+m_j)\vec{P}/M-\vec{p}_i-\vec{p}_j$$
$$=\vec{p}_k-m_k\vec{P}/M. \tag{A6}$$

Here, M is the total mass, $\vec{P}$ is the total momentum, $\vec{p}_{k-ij}$ is the relative momentum vector of particle k with respect to the center-of-mass system of particles i, j, and k, and $\vec{p}_{ij}$ is the relative momentum vector between particles i and j. First of all, let us consider an observation of only one particle at (θ_i^l, ϕ_i^l). The relations of the energy and angle of particle i between the center of mass system and the laboratory system can be written down as follows:

$$E_i^c = E_i^l - 2a_i (E_i^l)^{1/2} \cos\theta_i^l + (a_i)^2, \tag{A7}$$

$$\cos\theta_i^c = \frac{(E_i^l)^{1/2}\cos\theta_i^l - a_i}{(E_i^l - 2a_i (E_i^l)^{1/2}\cos\theta_i^l + (a_i)^2)^{1/2}}, \tag{A8}$$

$$\phi_i^c = \phi_i^l. \tag{A9}$$

Here a_i denotes the value defined by

$$a_i = (m_i m_p E_p^l)^{1/2}/(m_p + m_t). \tag{A10}$$

From these relations, it is easy to reduce a transformation of a cross section in the laboratory and center-of-mass system:

$$\frac{d^2\sigma^l}{dE_i^l\, d\phi_i^l\, d(\cos\theta_i^l)} = \left|\frac{E_i^l}{E_i^c}\right|^{1/2} \frac{d^2\sigma^c}{dE_i^c\, d\phi_i^c\, d(\cos\theta_i^c)}. \tag{A11}$$

In a case of two particles coincidence measurement, we can determine the scattered directions (θ_i^l, ϕ_i^l) and (θ_j^l, ϕ_j^l) and energies of two particles. Substituting those values into following relation, which

can be derived from the momentum and energy conservation:

$$Q = [E_i^1(m_i+m_k)+E_j^1(m_j+m_k)-2(m_p m_i E_p^1 E_i^1)^{1/2}\cos\theta_i^1$$

$$-2(m_p m_j E_p^1 E_j^1)^{1/2}\cos\theta_j^1+2(m_i m_j E_i^1 E_j^1)^{1/2}\cos\theta_{ij}^1]/m_k-E_p^1(1-m_p/m_k), \quad (A12)$$

"Q-value" of the reaction can be obtained. Here

$$\cos\theta_{ij}^1 = \cos\theta_i^1\cos\theta_j^1 + \sin\theta_i^1\sin\theta_j^1\cos(\phi_i^1 - \phi_j^1). \quad (A13)$$

The total kinetic energy can then be written

$$E_{tot}=E_p+E_t+Q$$

$$=p_i^2/(2m_i)+p_j^2/(2m_j)+p_k^2/(2m_k)$$

$$=P^2/(2M)+E_{ij}+E_{k-ij}, \quad (A14)$$

where

$$E_{ij}=p_{ij}^2/2\mu_{ij} \quad (A15)$$

is the relative kinetic energy of particle i and j, and

$$E_{k-ij}=p_{k-ij}^2/(2\mu_{k-ij})$$

$$=E_k^C M/(m_i+m_j) \quad (A16)$$

is the kinetic energy of particle k in the center-of-mass system of all three particles. It should be noted that all quantities mentioned above can be defined in terms of the momenta and masses of the two particles i and j that are detected experimentally.

For a fixed value of Q we can get the transfer relation between

the triple differential cross section of laboratory and center-of-mass systems using the phase space relation:

$$d\vec{p}_{i-jk}d\vec{p}_{jk}=d\vec{p}_i d\vec{p}_j=d\vec{p}_j d\vec{p}_k=d\vec{p}_k d\vec{p}_i. \tag{A17}$$

The obtained relations are as follows:

$$\frac{d^3\sigma}{dE_{k-ij}d\Omega_{ij}d\Omega_{k-ij}} = \frac{\mu_{ij}\mu_{k-ij}p_{ij}p_{k-ij}}{m_i m_j p_i p_j} *$$

$$\left|\frac{-\{(m_j+m_k)-m_j\vec{P}\cdot\vec{p}_j/p_j^2+m_j\vec{p}_i\cdot\vec{p}_j/p_j^2\}}{\{(m_i+m_k)-m_i\vec{P}\cdot\vec{p}_i/p_i^2+m_i\vec{p}_i\cdot\vec{p}_j/p_i^2\}}\left(\frac{m_j}{m_i+m_j}-\frac{m_i}{m_i+m_j}\vec{p}_i\cdot\vec{p}_j/p_i^2\right)\right.$$

$$\left.+\left(\frac{m_i}{m_i+m_j}-\frac{m_j}{m_i+m_j}\vec{p}_i\cdot\vec{p}_j/p_j^2\right)\right| \frac{d^3\sigma}{dE_i^1 d\Omega_i^1 d\Omega_j^1} \tag{A18}$$

and

$$\frac{d^3\sigma}{dE_{ki}d\Omega_{ki}d\Omega_{j-ki}} = \frac{\mu_{ki}p_{ki}p_{j-ki}}{m_i p_i p_j}\left|1-\frac{m_j\vec{P}\cdot\vec{p}_j}{Mp_j^2}\right| \frac{d^3\sigma}{dE_i^1 d\Omega_i^1 d\Omega_j^1}. \tag{A19}$$

Other useful relations for a fixed value of Q can be obtained from (A12);

$$\frac{dE_i^1}{dE_j^1} = \frac{-\{(m_j+m_k) - m_j\vec{P}\cdot\vec{p}_j/p_j^2 + m_j\vec{p}_i\cdot\vec{p}_j/p_j^2\}}{\{(m_i+m_k) - m_i\vec{P}\cdot\vec{p}_i/p_i^2 + m_i\vec{p}_i\cdot\vec{p}_j/p_i^2\}}, \tag{A20}$$

and from (A4) and (A15);

$$\frac{dE_{ij}}{dE_j^1} = \frac{dE_i^1}{dE_j^1}\,(m_j-m_i\vec{p}_i\cdot\vec{p}_j/p_i^2)/(m_i+m_j) + (m_i-m_j\vec{p}_i\cdot\vec{p}_j/p_j^2)/(m_i+m_j). \tag{A21}$$

B. Efficiency Calculation of ^{8}Be Detection

In this appendix we discuss the kinematics of a $^{8}Be_{g.s.}$ breakup and the details of the effective solid angle caculation which was used for the data analysis. (The notation of Ref. [41] will be used.)

Since the $^{8}Be_{g.s.}$ has no spin, its alpha decay is isotropic in the ^{8}Be rest system. Two breakup alpha particles from relatively fast moving ^{8}Be will travel within a cone whose axis is the direction of the original ^{8}Be. The half-angle α_{max} of the cone is given by

$$\alpha_{max}=\sin^{-1}(B/E8)^{1/2}, \tag{B1}$$

where B is a breakup energy (92 KeV for $^{8}Be_{g.s.}$) and E8 is a laboratory energy of ^{8}Be. In Fig. B-1(a) the velocity diagram of the $^{8}Be_{g.s.}$ breakup is shown. As seen in the figure, in a case of $\alpha<\alpha_{max}$ one alpha particle detecting angle α in the laboratory system corresponds to two different breakup angles $\psi^{\pm}$ in the ^{8}Be rest system. In other words, there are two possible angles α_c^{+} and α_c^{-} for a breakup companion. The kinematic relations of these quantities are given as follows:

$$\psi^{\pm}=\cos^{-1}\{-(E8/B)^{1/2}\sin^{2}\alpha\pm\cos\alpha\,[1-(E8/B)\sin^{2}\alpha]^{1/2}\}, \tag{B2}$$

$$\psi_c^{\pm}=\pi-\psi^{\pm}, \tag{B3}$$

and

$$\alpha_c^{\pm}=\cos^{-1}\{[(B)^{1/2}\cos\psi_c^{\pm}+(E8)^{1/2}]/[B+E8+2(Bx8)^{1/2}\cos\psi_c^{\pm}]^{1/2}\}. \tag{B4}$$

Because the decay of the $^{8}Be_{g.s.}$ is isotropic, the possibility of

Fig. B-1(a). Velocity diagram for the breakup of the ^{8}Be into two α-particles.

(b). Geometry of two detectors and the directions of the ^{8}Be and its breakup two α-particles.

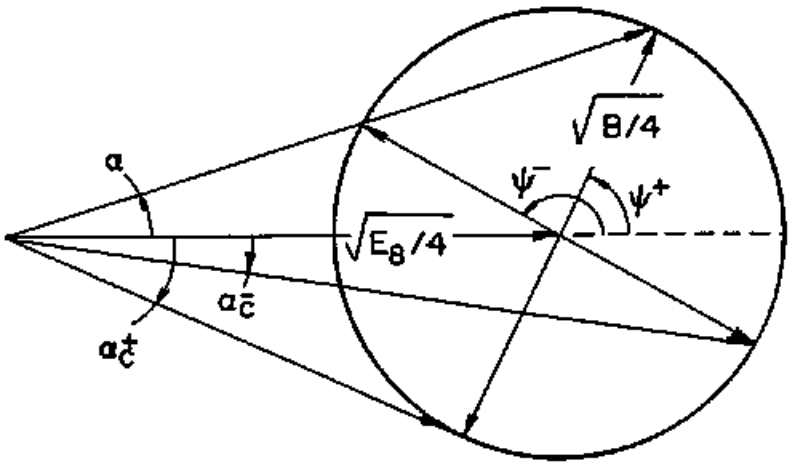
α
$\sqrt{E_B/4}$
$\sqrt{B/4}$
ψ^-
ψ^+
α_c^-
α_c^+

(a)

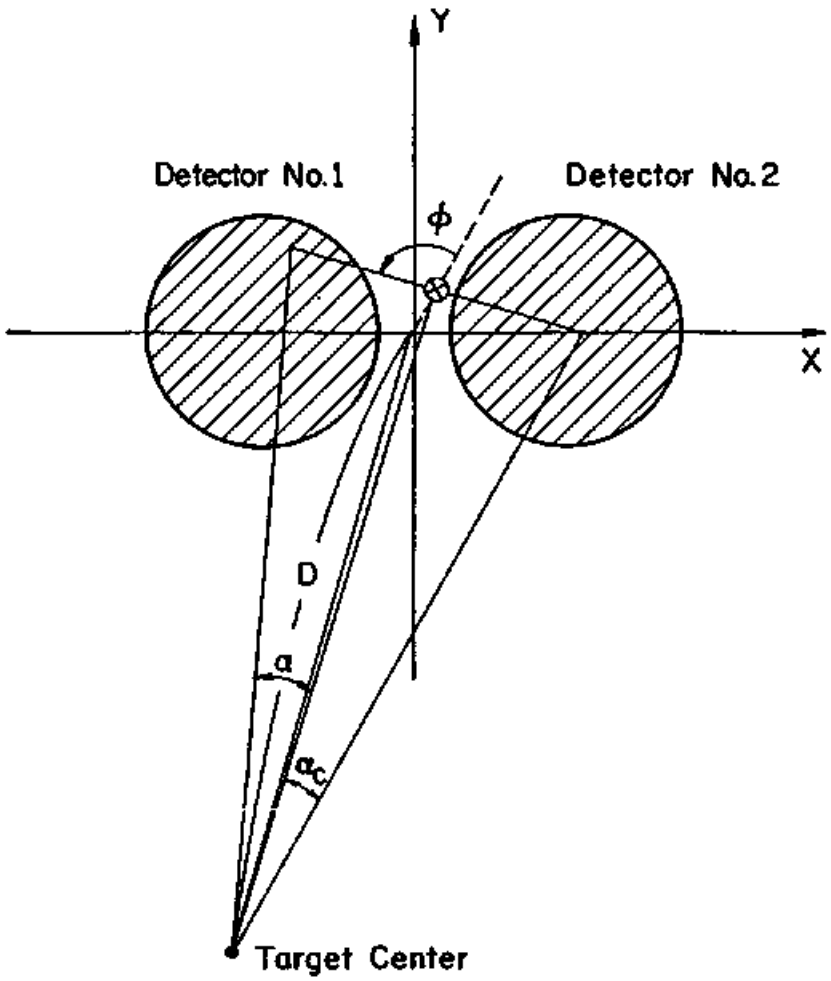
Y
Detector No.1
Detector No.2
ϕ
X
D
α
α_c
Target Center

(b)

detection of alpha particles per unit solid angle at an angle α is proportional to a sum of solid angle transformation factors

$$\left|(\sin\psi^{+}d\psi^{+})/(\sin\alpha d\alpha)\right| \tag{B5}$$

and

$$\left|(\sin\psi^{-}d\psi^{-})/(\sin\alpha d\alpha)\right|. \tag{B6}$$

If we define a detection probability $P^{\pm}(\alpha)$ by

$$P^{\pm}(\alpha)= \left|(\sin\psi^{\pm}d\psi^{\pm})/(\sin\alpha d\alpha)\right|/4\pi$$

$$=\{\pm 2(E8/B)^{1/2}\cos\alpha+(1+E8\cos 2\alpha/B)(1-E8\sin^{2}\alpha/B)^{-1/2}\}/4\pi, \tag{B7}$$

the total probability that one of the decayed alpha particles goes into the solid angle $d\Omega_{\alpha}$ at an angle α can be described as $2[P^{+}(\alpha)+P^{-}(\alpha)]d\Omega_{\alpha}$. The factor of 2 comes from the fact that either of the two alpha particle may be detected. To get an effective solid angle Ω, we have to integrate this value over all ^{8}Be directions $d\omega$ and over the surfaces of detectors. Therefore,

$$\Omega=\Omega_{+}+\Omega_{-}, \tag{B8}$$

where

$$\Omega_{\pm}=\int d\omega\ \sin\alpha d\alpha d\phi\ P^{\pm}(\alpha)S^{\pm}(\alpha,\phi;\omega). \tag{B9}$$

The function $S^{\pm}(\alpha,\phi;\omega)$ is defined by

$S^{\pm}(\alpha,\phi,\omega)=1$ if the companion alpha is

detected in the other detecter

$=0$ otherwise, (B10)

and the azimuthal angle ϕ is indicated in Fig. B-1(b). It should be noted that S^{+} and S^{-} are not always same, because at a fixed angle α, the angles $\alpha_c\pm$ of the companion are not equal to each other.

We will apply this analysis to two equal area circular detectors illustrated in Fig. B-1(b). Considering the symmetry, only integration over the first quadrant is needed with respect to ω, and then the result is multiplied by a factor of four. In addition, one has to consider only half range of the angle ϕ and then multiply the result by a factor of two. If we define the distance D from the target center to the center of two detectors,

$$d\omega=dXdY/\{D^2[1+(X^2+Y^2)/D^2]^{3/2}\}. \quad (B11)$$

Therefore, eqs. (B8), (B9) and (B11) give

$$\Omega=8/D^2\int_0^{X_{max}}dX\int_0^{Y_{max}}dY\left(1+\frac{Y^2+X^2}{D^2}\right)^{-2/3}[F^{+}(\omega)+F^{-}(\omega)], \quad (B12)$$

where the upper limits of integrations correspond to the maximum directions of strolling ^{8}Be which can result in coincident events. Here

$$F^{\pm}(\omega)=\int_{-\pi/2}^{\pi/2}\int_0^{\alpha_{max}}P^{\pm}(\alpha)S^{\pm}(\alpha,\phi;\omega)\sin\alpha d\alpha d\phi. \quad (B13)$$

Normally the functions S^+ and S^- are unity over a certan range in α. If we define those ranges $[\alpha_1^+, \alpha_2^+]$ and $[\alpha_1^-, \alpha_2^-]$ for S^+ and S^-, respectively, we can rewrite eq. (B13) as follows:

$$F^{\pm}(\omega) = 1/4\pi \int_{-\pi/2}^{\pi/2} d\phi \{\pm(E8/B)^{1/2} \sin^2\alpha - \cos\alpha(1-E8\sin^2\alpha/B)^{1/2}\]_{\alpha_1^{\pm}}^{\alpha_2^{\pm}}. \qquad (B14)$$

It should be noted that the limits $\alpha_1^{\pm}$ and $\alpha_2^{\pm}$ are functions of both ϕ and ω. The searching for $\alpha_1^{\pm}$ and $\alpha_2^{\pm}$ values and the integrations in eq. (B12) and (B14) were performed on a VAX-11/780 computer.

C. Calculation of Sequential Decay Process

1) Kinematics of the Sequential Decay Process

In this appendix we summarize the kinematics of the sequential decay process. In following equations the subscripts p and t refer to the projectile and target particles and the subscripts 1, 2 and 3 refer to the final state three particles. The ejectile before decaying into the particles 1 and 2 is represented by the subscript e. As usual, the symbols m, E and v denote the mass, energy and velocity respectively. If we determine Q-values of the first and second step reaction processes Q_f and Q_s, the scattered angle of the ejectile (θ_e, ϕ_e) and the detection angle of the partile 1, θ_1, we can calculate the enegy E_1. The energy E_e is easily obtained by using usual two-body kinematics as follows:

$$E_e = \frac{m_p m_e E_p}{(m_e+m_3)^2}\{2\cos^2\theta_e + \frac{m_3(m_e+m_3)}{m_p m_e}(\frac{Q_f}{E_p} - \frac{m_p}{m_3} + 1)$$
$$\pm 2\cos\theta_e[\cos^2\theta_e + \frac{m_3(m_e+m_3)}{m_p m_e}(\frac{Q_f}{E_p} - \frac{m_p}{m_3} + 1)]^{1/2}\}$$
$$= m_e v_e^2/2 \qquad (C1)$$

Considering the sum of the velocity vectors, we can get following equations.

$$E_1 = m_1 v_1^2/2 \qquad (C2)$$

$$v_1 = v_e\cos\theta_{1e} \pm \{v_e^2\cos^2\theta_{1e} - v_e^2 + 2Q_s/(m_1 + m_1^2/m_2)\}^{1/2} \qquad (C3)$$

$$\cos\theta_{1e} = \cos\theta_1\cos\theta_e - \sin\theta_{1e}\sin\theta_e\cos\phi_e. \qquad (C4)$$

2) Magnitudes of the Structures

To calculate the magnitudes of the structures induced in the inclusive α-spectrum due to the sequential ejectile decay processes, in principle, entire angular correlations (even out of plane correlations) of α-^{12}C and α-^{16}O would be required. At the present time, however, there are not enough informations of these angular correlations. So, we have attempted to interpolate and extrapolate a few available coincidence data taken by RCNP group [25] and to estimate the magnitudes assuming isotropic decays of ejectiles $^{16}O^*$ and $^{20}Ne^*$. The procedures of the calculation are as follows.

i) To make tables of the triple differential cross sections

$$\frac{d^3\sigma}{dE_{\alpha\text{-}^{12}C}\, d\Omega_{\alpha\text{-}^{12}C}\, d\Omega_{\alpha^{12}C\text{-}^{12}C}}$$

and

$$\frac{d^3\sigma}{dE_{\alpha\text{-}^{16}O}\, d\Omega_{\alpha\text{-}^{16}O}\, d\Omega_{\alpha^{16}O\text{-}^{8}Be}}$$

as a function of a relative energy between α and ^{12}C or α and ^{16}O, and a direction of their center-of-mass motion using RCNP group's coincidence data. (Assuming isotropic decays of ejectiles $^{16}O^*$ and $^{20}Ne^*$. these values are independent on decay directions.)

ii) To define the α-detection angle and α energy in the laboratory system.

iii) To calculate an observable energy of coincident ^{12}C and ^{16}O at a certain heavy-ion detection angle using the three-body kinematics.

iv) To get the relative energies between α and ^{12}C, and α and ^{16}O, and directions of their center-of-mass motions.

v) To consult the table of the cross sections at the calculated relative energies and the directions. (A quadratic inerpolation or extrapolation are made if necessarily.)

vi) To convert the tabulated cross sections to those in the laboratory system by using eq. (A18).

vii) To integrate obtained laboratory cross sections over whole available directions of ^{12}C or ^{16}O (including out of the reaction plane).

viii) To change the α energy and repeat same procedures after iii).

N.B. To introduce unisotropic decays, only procedures i) and v) should be modified.

To increase a speed of calculation, we introduce the Gaussiann quadrature in procedure vii).